ORNL/TM-2011/449

An Innovative Technique for Evaluating the Integrity and Durability of Wind Turbine Blade Composites - Project Final Report

October 2011

Prepared by

Jy-An John Wang[1], Fei Ren[1], Ting Tan[1], John Mandell[2], Pancasatya Agastra[2]

[1]Materials Science and Technology Division
Oak Ridge National Laboratory

[2]Montana State University

ORNL/TM-2011/449

Materials and Technology Division
Oak Ridge National Laboratory

An Innovative Technique for Evaluating the Integrity and Durability of Wind Turbine Blade Composites

FY2011 Project Report

Jy-An John Wang[1], Fei Ren[1], Ting Tan[1], John Mandell[2], Pancasatya Agastra[2]

[1]Materials Science and Technology Division
Oak Ridge National Laboratory

[2]Montana State University

Date Published: October 2011

Prepared by
OAK RIDGE NATIONAL LABORATORY
Oak Ridge, Tennessee 37831
Managed by
UT-BATTELLE, LLC

For the
U.S. DEPARTMENT OF ENERGY
under contract DE-AC05-00OR22725

ACKNOWLEDGEMENTS

This research was sponsored by the Wind Energy Program of Department of Energy and was carried out at Oak Ridge National Laboratory under contract DE-AC05-00OR22725 with UT-Battelle, LLC. The authors are grateful to Mr. Stanton Hadley, Dr. Brennan Smith, and Mr. Tom King Jr., for supporting this project.

The authors would like to thank Mr. Williams Bertelsen at Gougeon Brothers, Inc. and Mr. Carl LaFrance at Molded Fiber Glass Companies for providing epoxy materials.

Table of Contents

LIST OF FIGURES

LIST OF TABLES

EXECUTIVE SUMMARY

To build increasingly larger, lightweight, and robust wind turbine blades for improved power output and cost efficiency, durability of the blade, largely resulting from its structural composites selection and aerodynamic shape design, is of paramount concern. The safe/reliable operation of structural components depends critically on the selection of materials that are resistant to damage and failure in the expected service environment. An effective surveillance program is also necessary to monitor the degradation of the materials in the course of service. Composite materials having high specific strength/stiffness are desirable for the construction of wind turbines. However, most high-strength materials tend to exhibit low fracture toughness. That is why the fracture toughness of the composite materials under consideration for the manufacture of the next generation of wind turbines deserves special attention.

In order to achieve the above we have proposed to develop an innovative technology, based on spiral notch torsion test (SNTT) methodology, to effectively investigate the material performance of turbine blade composites. SNTT approach was successfully demonstrated and extended to both epoxy and glass fiber composite materials for wind turbine blades during the performance period. In addition to typical Mode I failure mechanism, the mixed-mode failure mechanism induced by the wind turbine service environments and/or the material mismatch of the composite materials was also effectively investigated using SNTT approach. The SNTT results indicate that the proposed protocol not only provides significant advance in understanding the composite failure mechanism, but also can be readily utilized to assist the development of new turbine blade composites.

In FY10, an extensive study was performed to characterize the fracture behavior of epoxy materials. This effort included equipment setup and calibration, sample design and fabrication, sample fatigue pre-crack and final fracture testing, and fractographic examination using advanced microscopic techniques. The detailed description of the progress and results from testing epoxy samples is included in the attached FY10 annual report (Appendix A). For all epoxy samples tested in this study, linear elastic behavior was observed, which is consistent with the brittle feature of these materials. Mode I samples fractured along a spiral plane that had a 45^{o} pitch angle with respect to the sample axis. For some mixed-mode samples the final failure mode appeared to be also along the 45° pitch angle, indicating that Mode I fracture still dominated in these mixed-mode samples. Under fatigue loading conditions, Mode I samples formed a uniform fatigue zone, which then grew into a uniform band of mirror along 45° spiral plane. In contrast, a semi-elliptical fatigue zone was discovered on some mixed-mode samples failed at 45° pitch angle. A transition region was also found between the fatigue zone and the mirror during fatigue crack growth in the mixed mode, indicating the crack growth mode changed from mixed-mode to Mode I.

Finite element method (FEM) was used to estimate energy release rates and fracture toughness of the epoxy SNTT samples. Numerical FEM models were successfully established to capture the stress concentrations around the non-coplanar three-dimensional spiral crack front. FEM results showed that the energy release rates varied with different types of epoxy samples, including the geometry variation related to initial notch sharpness and final crack length. The energy release rates of some mixed-mode failure were higher than those of Mode I failure. The energy release rates of samples with fatigue precrack were lower than those without pre-fatigue crack due to the sharper crack front. In the meantime, samples failed during the fatigue progress possessed much lower energy release rates due to the significantly higher loading rates, about two orders of magnitude higher than that in a typical quasi-static SNTT test.

Shallow notch depth, where the majority of epoxy SNTT samples had initial notch depth to sample diameter ratio around 0.1, and insufficient precision control on the notch root sharpness, could result in less constraint boundary conditions in the vicinity of the crack front. This may result in a relative higher energy release rate and fracture toughness compared to that of SNTT sample with sharper notch root and higher a/D ratio. As regarding the mixed-mode study, the above mentioned constraint issues can also affect the mixed-mode failure investigation, such as fracture contour aligns with mixed-mode contour or climbs back to 45° principal stress plane. Therefore, more investigation on epoxy fracture behaviors will be performed in the future on refined SNTT samples with sharper crack fronts and relatively deeper crack penetration length to reaching higher a/D ratios. By doing so we can further increase the SNTT sample geometry constraint to increase the accuracy of obtaining intrinsic fracture toughness of these materials.

The successful experience of applying SNTT approach to epoxy materials was then extended to polymeric composite materials in FY11. A significant amount of effort of this initiative was focused on the design and fabrication of composite samples suitable for SNTT testing. Various designs and trials were carried out in a joint collaboration between Oak Ridge National Laboratory and Montana State University. The progress on composite sample fabrication is detailed in the attached FY11 Q1 report (Appendix B). One of the successful approaches to manufacture composite samples utilized the vacuum assisted infusion. Bulk polymeric composite plates were manufactured and SNTT samples were subsequently machined from these plates. Three different sample configurations were designed such that the angle between the sample axis and the fiber orientations were 90^o, 0^o, and 45^o for A -type, B-type, and C-type samples, respectively.

During SNTT testing, A-type and C-type samples exhibited similar behavior. The cracks tended to initiated from a single location along the notch root and then extended to the entire notch length. The fracture plane propagated through the samples and separated the SNTT samples into halves. However, the fracture surfaces of A-type appeared to be flat; while a spiral plane was observed on the fracture surfaces of C-type samples. Both A and C-types samples appeared to

fail at the glass fiber/epoxy matrix interface, which is a typical delamination failure mode. In contrast, B-type samples were not completely separated but held together by the glass fibers upon final failure. A very complex crack pattern on the cross section of B-type samples was observed with three crack systems: 1) cracks along the fabric interfaces; 2) cracks between the fiber strands; and 3) a circular crack approximately corresponded to the projection of the spiral notch on the cross-section plane.

Three finite element models were developed for the composite SNTT samples along different fiber orientations. The composite materials were assumed to be orthotropic in the developed models. Meshing was successfully established to capture the stress concentrations along the three-dimensional spiral crack front for these composite samples. Asymmetric von Mises stress contours were obtained based on the orthotropic assumption. The SNTT composite results indicated that the fiber orientations and the associated embedded fiber lengths have significant impact to the fracture resistance of the composite samples. It was shown that the energy release rates of B-type composite samples were the highest and those of A-type samples were the lowest. The energy release rates of composite samples did not appeared to be sensitive to loading rates included in this study. In addition it was found that the energy release rate of the composite samples was lower than that of the epoxy matrix.

In this study, the interfacial region appears to be the weakest link in the wind turbine blade composites. In order to pave a solid path for future investigation on the interfacial failure mechanisms of the composite materials, extensive effort was also carried out to develop composite SNTT samples for interfacial bonding investigation. A series of sample designs and fabrication trials resulted in two types of infusion samples, e.g. epoxy samples with grooves embedded by glass fibers, and composite samples with grooves embedded by epoxy resin. These samples demonstrated the viability to create artificial interfaces between resins and reinforcement fibers using the infusion technique. Combining advanced monitoring methods (e.g. acoustic emission) and finite element analysis, the fracture events at the interfaces could be accurately monitored and modeled. These results will provide necessary information to detailed understanding of interfacial fracture phenomena. In addition, these successful experiences can be further extended to investigating the integrity of the adhesive bonding, which is heavily used in industrial manufacturing of large wind turbines.

Other areas of interests to investigate in the future include testing of samples obtained from industrial wind turbines, testing under cyclic loadings, and testing under simulated offshore conditions. Furthermore, our industrial partner, Molded Fiber Glasses Companies agreed to provide composite materials from their existing decommissioned wind turbine blades in the near future. Such aged wind turbine blade composite materials are extremely useful in benchmarking current available aging models or developing new prediction models for estimating the effective lifetime of wind turbine blade composites during service. These proposed future works will

significantly improve our understanding of the fracture behavior of wind composite materials and provide precious data and guidelines for the development of the wind energy industry.

1. Introduction and background

An increasing trend in blade size has been seen in design and fabrication of wind turbine blades, which is mainly due to the need of increasing the wind energy capture capability [Hayman 2008]. Meanwhile, improvement of performance heavily depends upon enhancing the reliability of turbines and components. This will require more thorough knowledge of material properties. In particular, the basic understanding of damage and failure mechanisms, the effects and interpretation of stochastic loadings, multiple stress states, *etc.* shall be obtained [Kensche 2006].

The safe/reliable operation of structural components depends critically on the selection of materials that are resistant to damage and failure in the expected service environment. An effective surveillance program is also necessary to monitor the degradation of the materials in the course of service. Composite materials having high specific strength/stiffness are desirable for the construction of wind turbines. However, most high-strength materials tend to exhibit low fracture toughness. That is why the fracture toughness of the composite materials under consideration for the manufacture of the next generation of wind turbines deserves special attention. We propose to develop new methods based on the spiral notch torsion test (SNTT), an ORNL patented, R&D 100 Award winning technology, to meet this need.

1.1 Mixed-mode loading of composite materials for wind turbine blades

Wind turbine blades are subjected to complex, multiaxial stress states during operation. Typical composite materials used for the manufacture of wind turbine blades consist of fiber (glass and/or carbon fibers)-reinforced polymeric (especially thermosetting polymers) materials [Brondsted 2005]. To ensure the reliability and safety of wind power systems it is necessary to identify the mechanisms that might lead to failure in blade materials and to fully characterize the material behavior under extreme conditions.

Fracture is one of the most dramatic failure modes of any engineering structure. A material's intrinsic capacity to resist fracture is known as the fracture toughness. The fracture toughness of fiberglass mostly comes from the interfacial bonding between fiber and resin matrix. In addition, matrix cracking and fiber fracture also contribute to the fracture resistance of fiberglass. Thus, to obtain a complete knowledge of the fracture behavior of fiberglass, it is important to understand the detailed behavior of the matrix, the fiber, and their interfacial regions under different loading conditions.

There are three independent fracture modes, i.e. Mode I (opening mode), Mode II (in-plane shear), and Mode III (tearing or out-of-plane shear) [Sanford 2003]. Since wind turbine blades are subject to mixed mode loading in their service environments, it is highly desired to study the mixed-mode loading effect on the integrity and durability of the wind turbine blade composites.

Compared to the numerous studies on Mode I fracture, the understanding of mixed mode fracture behavior is relatively limited. Thus, development of simplified test methods to characterize the fracture behavior of composite materials under mixed loading modes is essential to enable the qualification and use of these materials for the next generation wind turbines.

1.2 Spiral notch torsion test (SNTT)

In this project, a novel testing method based on the spiral notch torsion test (SNTT) [Wang 2002a] has been developed to quantify the fracture behavior of epoxy resins and polymeric composite materials under combined Mode I and Mode III loading.

The original SNTT test method uses a round-rod specimen having a V-grooved spiral line at a 45° pitch (Figure 1), subjected to pure torsion. In the absence of the V-groove, the stress state of a generic element in a round bar under pure torsion can be depicted as tension (normal to the 45° pitch) and compression (tangential to 45° pitch) of equal magnitude.

When a notch is introduced (Figure 1), a tri-axial tensile stress field will evolve in the neighborhood of the notch root area. This observation has been experimentally and analytically validated [Wang 2000, 2002b]. When the grooved specimen is sectioned into segments perpendicular to the groove line, each of the segments can be viewed as a compact tension (CT) specimen with a notch. Since all the imaginary CT specimens are bonded side-by-side seamlessly, the compatibility condition is automatically satisfied, and remains in place before and after application of torsion loading.

Therefore, when a V-grooved spiral line with a 45° pitch is machined on the surface of the specimen, the grooved line effectively becomes a Mode I crack mouth opening. When the pitch angle is different than 45°, mode III component is introduced at the notch root, which enables the investigation of fracture behavior under I/III mixed mode loading.

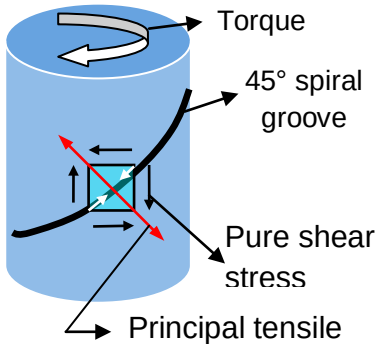

Figure 1. SNTT configuration.

Due to the 3-D non-coplanar crack front of the SNTT configuration and the lack of closed form solutions, K_{IC} of the SNTT method was evaluated using 3-D finite element analysis and derived from minimum strain energy density criterion [Sih 1974] or J-Integral based on the domain integral method [Wang 2000, 2002b].

2. Scope of current research

The objective of this research project is to develop a testing methodology based on spiral notch torsion test (SNTT) method to evaluate the effect of mixed-mode loading on the static and dynamic fracture behavior of composite materials used for wind turbine blades. The project is divided into the following stages:

1) SNTT testing and fracture toughness evaluation for epoxy resin materials
2) SNTT testing and fracture toughness evaluation for composite materials;

In the first stage, SNTT samples were designed and fabricated from epoxy resin – a common matrix material used in wind turbine blade composites. Spiral notches were machined on the epoxy samples with different notch depth and pitch angle. Using the SNTT technique, the fracture behavior of these epoxy samples was investigated for both notched sample and notched sample with fatigue pre-crack conditions. Fractographical examination was performed to study the fracture mechanisms; while finite element analysis was used to estimate the fracture toughness. The accomplishment in the first stage demonstrated the applicability of the SNTT technique to polymeric materials and provided understanding of the fracture behavior of these materials under different loading conditions.

Due to complexity of composite materials, a significant effort was dedicated to SNTT sample design and fabrication in the second stage of this project. Direct machining method for fabricating SNTT composite samples was selected from several different designs. SNTT experiments were performed on composite samples with various fiber orientations. The effect of loading rate on the fracture behavior of these samples was also investigated. Using microscopy and finite element analysis, the fracture surface and the fracture toughness of these composite samples were studied, respectively.

Pilot experiment of groove-infusion was conducted on both epoxy and composite samples. These samples would be suitable for future studies of the interfacial fracture between composites and epoxies as well as composites and bonding adhesives.

3. Testing and analysis of epoxy materials

Epoxies are good candidates used as matrix materials to fabricate polymeric composites in wind turbine blades. Its brittleness nature can lead to matrix cracking, a major failure modes in polymeric composites. Thus the fracture behavior of epoxy materials deserves special attention. A large amount of work was performed on fracture study of epoxies in FY10. The detailed information on equipment setup and calibration, sample design and fabrication, SNTT testing,

and post mortem fractographic examination is included in the attached FY10 annual report (Appendix A); while the highlights from FY10 are described in the following two sections (Sections 3.1 and 3.2).

3.1 Materials and samples

Three epoxy materials were used in this project: 1) Pro-Set® 117LV resin/229 hardener (Gougeon Brothers (GB), Inc. Bay City, MI); 2) Pro-Set® 117LV resin/XH10B hardener (Gougeon Brothers, Inc. Bay City, MI); and 3) Hexion® Epikote™ MGS® RIM135 resin/RIMH1366 curing agent, provided by Molded Fiber Glass Companies (MFG), Ashtabula, OH. The nominal composition of the resins and hardeners provided by the vendors are list in Table 1 and the processing conditions of the epoxies are given in Table 2.

Table 1. Chemical composition of the resins and hardeners used in the study.

Epoxy component	**Ingredient**	**concentration**
Pro-Set® 117LV infusion resin	Bisphenol-A type epoxy resin	
	Bisphenol-F type epoxy resin	
	Neopentyl glycol diglycidyl ether	< 25%
PRO-SET® 229 Hardener	Polyoxypropylenediamine	25-50%
	Reaction products of isophoronediamine with phenol/formaldehyde	< 25%
	Isophoronediamine	< 25%
	Triethylenetetramine (TETA)	<12%
	Hydroxybenzene	<7%
XXH10B Hardener	Polyoxypropylenediamine	25-50%
	Reaction products of isophoronediamine with phenol/formaldehyde	<25%
	Isophoronediamine	< 25%
	Triethylenetetramine (TETA)	<10%
	Hydroxybenzene	<7%
EPIKOTE™ Resin MGS RIMR 135	4,4'-Isopropylidenediphenol-Epichlorohydrin Copolymer	70-100%
	1,6-Hexanediol Diglycidyl Ether	10-30%
EPIKURE™ Curing Agent MGS RIMH 1366	Alkyletheramine	25-50%
	Isophoronediamine	20-25%
	Aminoethylpiperazine	<20%

Table 2. Processing conditions of the received epoxy materials.

Epoxy	117LV/229	117LV/XH10B	RIM135/RIMH1366
Resin to hardener ratio	100:31	100:33.9	100:30
Curing conditions	Overnight at room temperature followed by 8 hrs at 60°C		Cured through the exotherm, and post-cured for 6.5 hours at 70°C.

SNTT samples were machined according to the geometry shown in Figure 2a. The samples were 1" (25.4 mm) in diameter with a gauge length of 4" (101.6 mm). A V-shaped spiral groove was machined on the sample surface with a pitch angle θ. As mentioned in Section 1.2, when $\theta = 45^{o}$, the notch root is subject to an effective Mode I loading; and when $\theta < 45^{o}$, the notch root is then subject to a mixed loading of Mode I and Mode III. Examples of machined epoxy samples are shown in Figure 2b and Figure 2c.

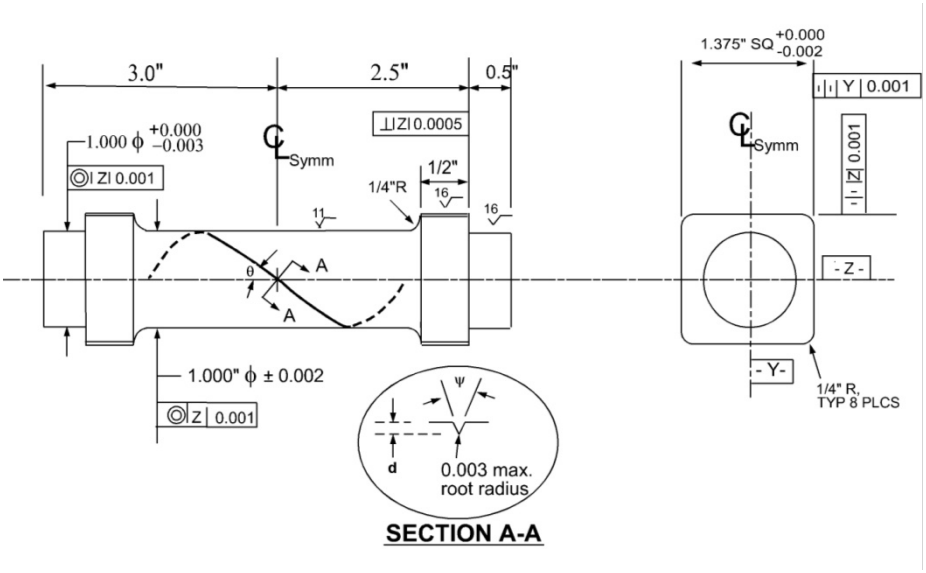

(a)

(b)

(c)

Figure 2. (a) The geometry of the epoxy SNTT samples, and pictures showing machined samples made from epoxy materials provided by (b) Gougeon Brothers, Inc. and (c) Molded Fiber Glass Companies.

3.2 SNTT experiments

In this project, a servo-hydraulic axial/torsional testing machine (Model 809, MTS Systems Corp. Eden Prairie, MN, USA) was used to perform SNTT testing. Notched samples with fatigue precrack or as received machined notch condition were used in the fracture tests.

For fracture testing, a fixed loading rate of 40 lbf-in/sec (4.52 N-m/sec) was used for all sample. For cyclic fatigue loading, the maximum torque, the minimum torque, the cycling frequency, and the cycle numbers varied. The fracture surfaces were examined by optical microscopy (SZH10, Olympus, Japan), scanning electron microscopy (S3400, Hitachi, Japan), and white light interferometer (Wyko NT9100, Veeco Instruments, USA).A detailed description of the tests performed on epoxy samples is given elsewhere [Wang 2010]. The following section will briefly review some highlights in the results.

All epoxy samples exhibited linear elastic behavior during SNTT fracture tests, which is expected for brittle materials such as epoxies. Some examples of loading curves are shown in Figure 3.

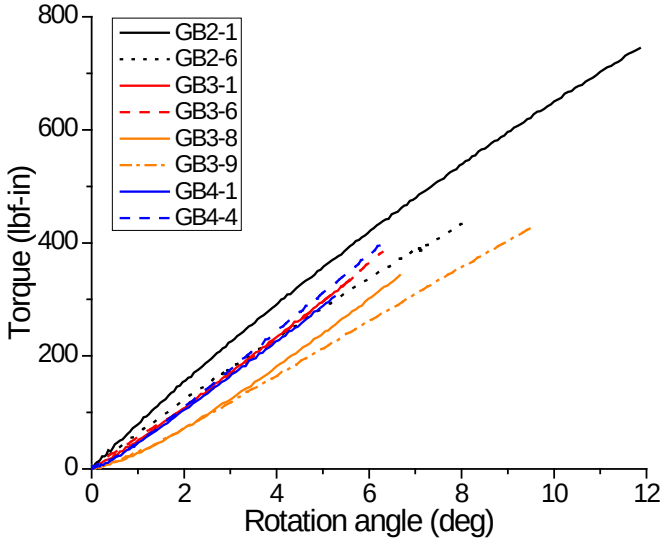

Figure 3. Example loading curves during final fracture tests performed on epoxy samples in this study. “GB” in the sample ID refers to samples provided by Gougeon Brothers.

3.2.1 Mode I fracture

For Mode I samples (pitch angle = 45^{o}) fractured without fatigue, primary cracks initiated from the notch root and propagated along the spiral plane toward/perpendicular to the center axis of the cylinder sample. For example, the fracture surface of sample GB3-1 is shown in Figure 4. The notch depth to sample diameter ratio (a/D) is 0.13.

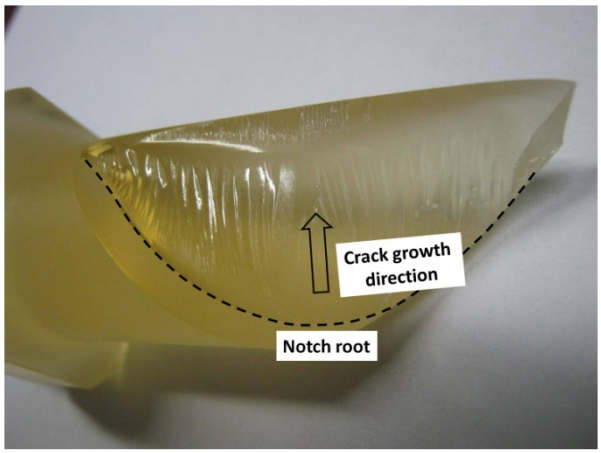

Figure 4. Fracture surface of sample GB3-1, a Mode I sample fractured without fatigue.

Two distinct regions were observed on the fracture surface: 1) a semi-elliptical “mirror” region and 2) a rough “hackle” region Figure 5. The mirror region was featureless under the optical microscope, while the hackle region consisted of river lines and ridges (Figure 5a), which were due to surface coarsening as the result of the speed of the crack propagation increased [Owen 1975]. A higher magnification image (Figure 5b) indicated the fracture origin was likely a surface flaw near the notch root. Some “zipper cracks” emanated from the fracture origin, which was likely related to machining induced flaws [ASTM C1322]. The apparent Mode I fracture toughness of sample GB3-1 is 1.5 $MPa\sqrt{m}$ with failure plane at 45 degree pitch angle.

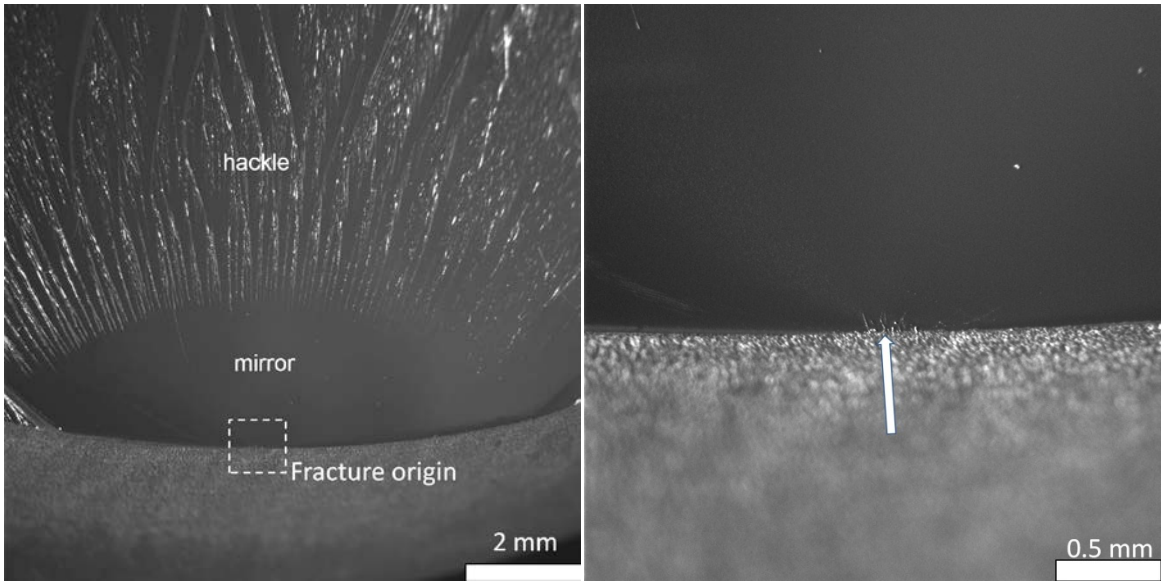

(a) (b)

Figure 5. Optical microscope images of sample GB3-1 showing (a) the mirror and the hackle, and (b) a possible fracture origin.

The fracture surface of Mode I samples subject to fatigue exhibited different features. Sample GB3-3 was fatigued between 15 lbf-in (2.26 N-m) and 150 lbf-in (22.6 N-m) for a total number of 3000 cycles and then fractured under monotonic loading of 40 lbf-in/sec (4.52 N-m/sec) loading rate. The apparent Mode I fracture toughness of sample GB3-3, with a/D=0.15, is 1.2 $MPa\sqrt{m}$ with failure plane at 45 degree pitch angle.

The primary fracture plane of sample GB3-3 was along the 45^o spiral plane. In contrast to Mode I samples fractured without fatigue, where the mirror region was semi-elliptical (Figure 5a), the mirror region on the fracture surface of GB3-3 appeared as a uniform band parallel to the notch root (Figure 6a). This observation demonstrated the geometrical constraint effect of SNTT configuration such that the crack was propagated perpendicularly toward the central axis of the SNTT sample and along the 45^o spiral crack front [Wang 2000], in contrast to the conventional fracture testing methods where crack may deviate from the designated propagation path and crack front may appear to be zig-zag or thumbnail shape.

Under higher magnification, a second uniform band, ~ 0.55 mm wide (Figure 6b), was observed between the notch root and the mirror region, which occurred due to crack growth during fatigue cycling. The fatigue region and the mirror region were separated by a boundary also parallel to the notch root, which was the arrest line of the crack front when fatigue cycling was stopped (Figure 6b).

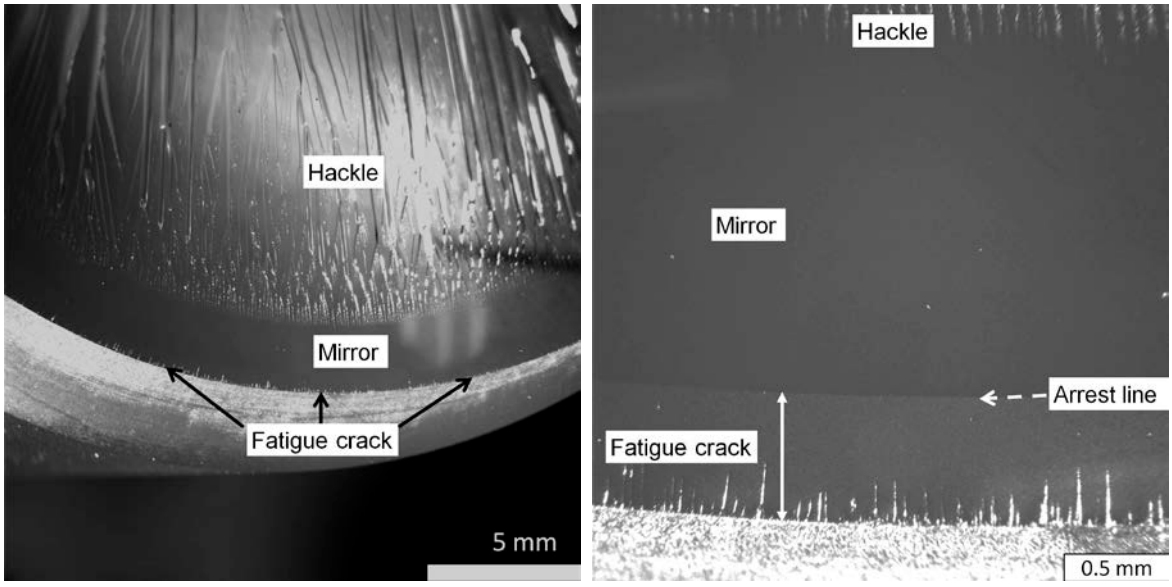

(a) (b)

Figure 6. Optical microscope images of the fracture surface of sample GB3-3, a Mode I sample fractured after fatigue.

In the fatigue region, a number of parallel fine markings were observed. These fine markings extended from the notch root and distributed uniformly, which eventually disappeared (Figure 6b). These fine makings seemed similar to the zipper cracks shown in Figure 5b except that they were parallel to each other and perpendicular to the notch root (Figure 6b). It was likely that during the fatigue cycling crack firstly initiated at a weakest location and then “unzipped” along the length of the notch root before further propagating into the bulk material. The fine markings gradually disappeared, which suggests that the local stress state at the crack front changed to pure Mode I during crack propagation under the SNTT configuration.

Figure 7 shows the topographical feature of the fatigue and mirror zones, where the fine markings and the crack arrest lines can be clearly identified. The arrest line also marked the onset of the crack initiation of the final fracture; and it was clear that the failure mode of the tested sample is Mode I fracture. The fracture surface remained mirror smooth while the hackle region appeared as a result of increasing crack propagation speed.

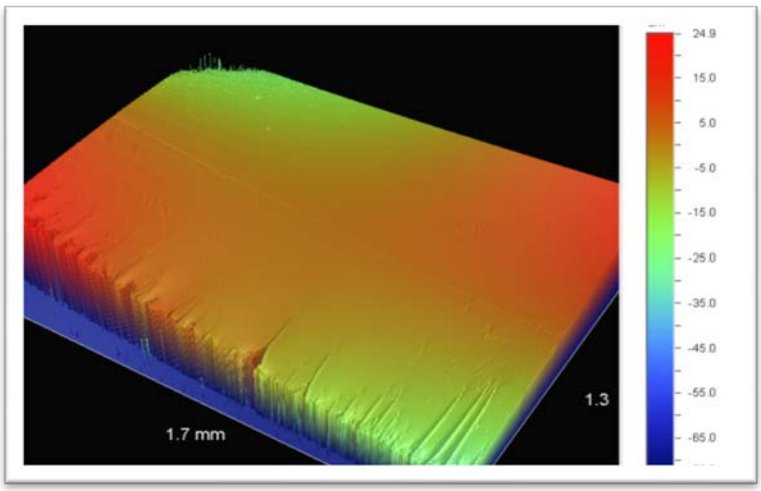

Figure 7. A white-light interferometry image showing the three-dimensional topography of sample GB3-3 near the notch root.

Different mirror shapes were observed on Mode I samples between samples with fatigue pre-crack and without fatigue pre-crack. For notched sample without fatigue pre-crack, crack initiated from the fracture origin (the weakest link along the notch root) and propagated in an unstable manner, resulting in a semi-elliptical mirror region emanating from the fracture origin. For fatigue pre-crack samples, when the stress level at the crack front reaching the fatigue

threshold, the crack initiated and grew inwards toward the center axis of SNTT sample along the spiral notch front. Eventually, the crack growth during fatigue cycles led to a uniform crack front along the 45° spiral plane, this results in a uniform band of mirror upon the subsequent fracture testing.

3.2.2 Mixed mode (Mode I Plus Mode III) fracture

The mixed-mode loading of Mode I+ Mode III can be readily seen in wind turbine blade in action, where Mode I in-plane tensile loading is from the flexural deformation/vibration of blade and Mode III out of plane shear stress loading is from torsion shear and tangential shear related to blade rotational deformation/acceleration. This type of failure is difficult to simulate from the conventional approaches or testing methods; but in term of SNTT approach it can be easily simulated by varying the pitch angles of spiral notch.

During SNTT fracture testing, some mixed mode samples fractured initiated at the weakest location along the notch root and the final fracture propagated along the 45^o spiral plane contour. Figure 8a shows the fractured surface of sample GB1-6 with a pitch angle of 36^o, which was fractured without fatigue. A semi-elliptical mirror region and a hackle region were observed on the fracture surface (Figure 8b). The apparent mixed-mode fracture toughness, K_{MC}, of sample GB 1-6, with a/D=0.1 and no observed fatigue crack growth, is 2.23 $MPa\sqrt{m}$. This sample is from the 1^{st} batch with failure plane at 45 degree pitch angle.

While other mixed-mode samples, multiple fractures initiation sites were observed from the spiral notch-root contour (Figure 9a). Multiple mirror regions next to the notch root were separated by large furrows and ridges (Figure 9b). However, the mechanism led to this multiple-mirror fracture is not clear and will be investigated in future studies. The apparent mixed-mode fracture toughness, K_{MC}, of sample GB 4-7, with a/D=0.1 and no fatigue –pre-crack, is 1.00 $MPa\sqrt{m}$. This sample is from the 2^{nd} batch with failure plane at 36 degree pitch angle.

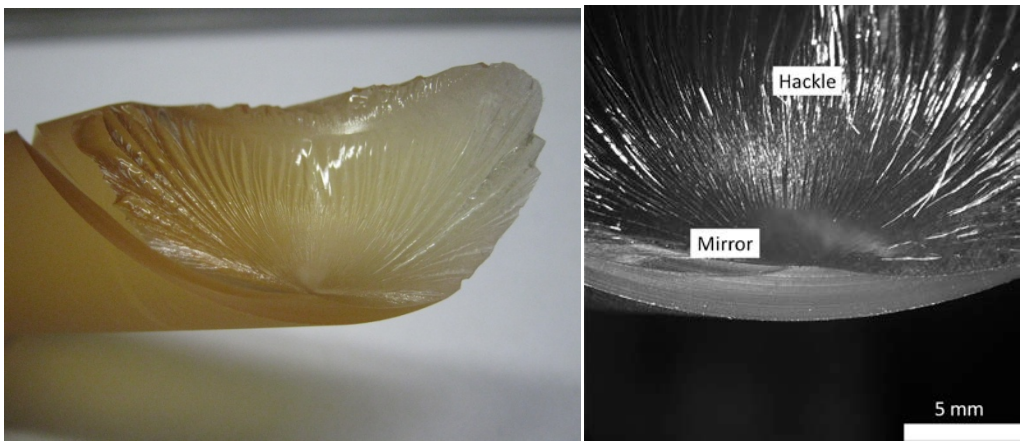

(a) (b)

Figure 8. Optical microscope images of the fracture surface of sample GB1-6, a mixed mode sample (pitch angle = 36^o) fractured without fatigue.

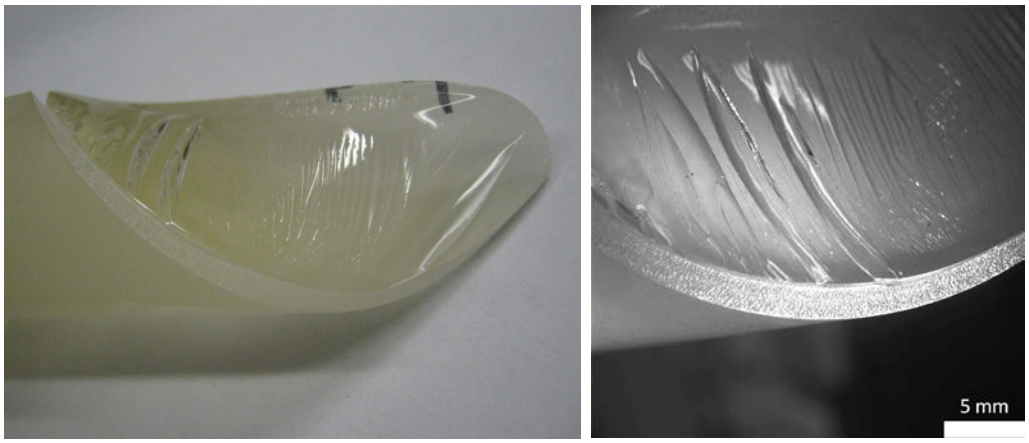

(a) (b)

Figure 9. Optical microscope images of the fracture surface of sample GB4-7, a mixed mode sample (pitch angle = 36^o) fractured without fatigue.

Preliminary tests indicated that no significant precracks could be observed on mixed-mode samples fatigued for less than 100,000 cycles, thus sample GB1-7 (pitch angle = 36^o) was cycled between 15 lbf-in (2.26 N-m) and 150 lbf-in (22.6 N-m) for a total number of 260,000 cycles before final fracture testing. The apparent mixed-mode fracture toughness, K_{MC} , of sample GB 1-7, with a/D=0.16, is 1.81 $MPa\sqrt{m}$. This sample is from the 1st batch with failure plane at 45 degree pitch angle.

For sample GB1-7 (and others subjected to mixed-mode fatigued loading), fracture initiated from a single location along the notch root (Figure 10a). The primary fracture appeared to close to a 45^o spiral plane with respect to the sample axis. Four regions can be identified on the fracture surface: 1) the fatigue zone, 2) the transition zone, 3) the mirror, and 4) the hackle (Figure 10b).

The fatigue zone appeared semi-elliptical, containing river lines irradiated from the fracture origin (Figure 10b). The existence of river lines indicated that the stress state had a mode III component when the precrack formed [Hull 1999], which implied contribution mode III loading to the crack initiation when subject to mixed mode cycling.

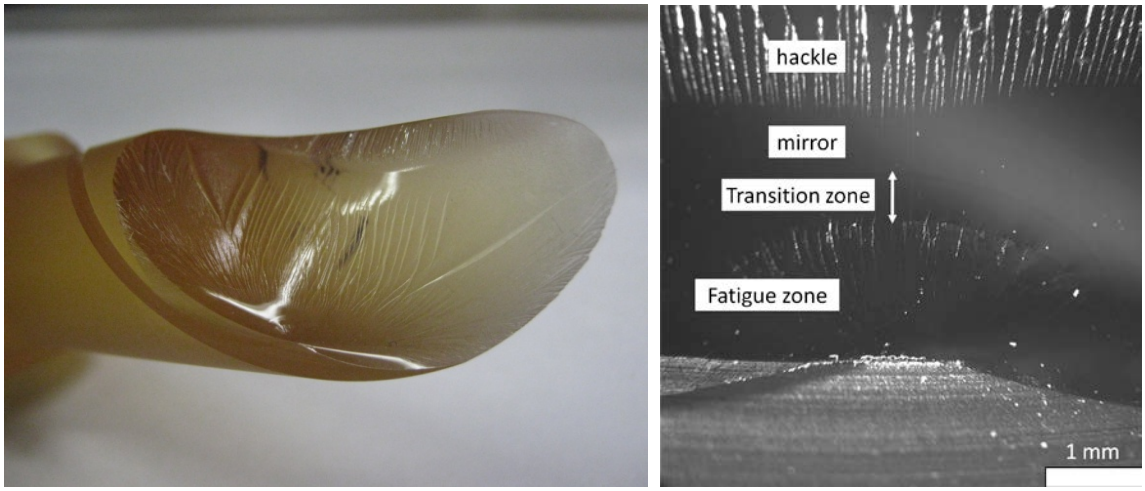

(a) (b)

Figure 10. Optical microscope images of the fracture surface of sample GB1-7, a mixed mode sample (pitch angle = 36^{o}) fractured after fatigue.

Striation lines were observed in the fatigue zone of some fatigued mixed-mode samples. Figure 11a. shows an SEM image of the fatigue zone of sample GB1-4, fractured during cyclic fatigue. These striations, approximately perpendicular to the river lines, were traces of crack front growth. Since wind turbine blades are constantly loaded under multiaxial forces, mixed mode effect on the fatigue behavior must be considered when designing components utilizing epoxy materials.

The transition zone appeared to be a uniform band with a “rainbow” shape, which was observed between the fatigue zone and the mirror region (Figure 10b). Figure 11b is a three-dimensional reconstruction of the fracture surface. The fatigue zone, on the left, had a relative rough surface compared to the transition zone on the right (Figure 11b). It can be seen that not only the direction of crack propagation was altered, the propagation mode also changed from mixed mode I/III to Mode I, as evidenced by the disappearing river lines into the transition zone. This unique transition zone indicated that for this epoxy material the primary crack can propagate aligned to the maximum tensile direction, if condition allows, such as less localized constraint or low a/D ratio. This phenomenon is also material dependent and sensitive to notch root sharpness as demonstrated in the previous sections.

It is speculated that shallow notch depth, where the majority of epoxy SNTT samples had initial notch depth to sample diameter ratio around 0.1, and insufficient precision control on the notch root sharpness, result in less constraint boundary condition in the vicinity of the crack front. This may result in a relative higher energy release rate and fracture toughness evaluation compared to that of SNTT sample with sharper and deeper a/D ratio. As regarding the mixed-mode study, the above mentioned constraint issues can also affect the mixed-mode failure investigation, such as fracture contour aligns with mixed-mode contour or climbs back to 45° principal stress plane. Therefore, more investigation on epoxy fracture behaviors is recommended with a refined SNTT samples preparation protocol that can generate a sharp crack front with relatively deeper crack penetration length to reaching higher a/D ratios. By doing so we can further increase the SNTT sample geometry constraint to increase the accuracy of obtaining intrinsic fracture toughness of polymer materials.

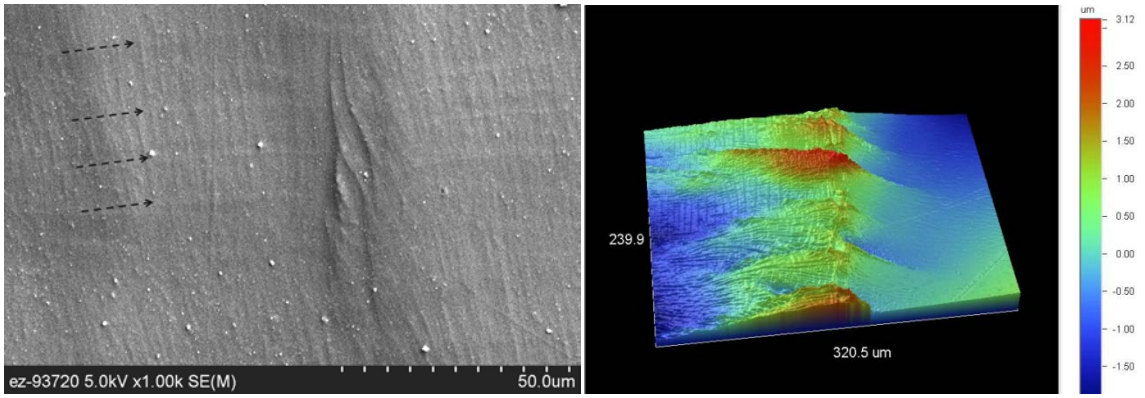

(a) (b)

Figure 11. For sample GB1-4, (a) a SEM image showing the striation lines, and (b) a white-light interferometry image showing the 3-D topography of the transition zone.

3.3 Finite element analysis

Finite element analysis (FEA) was used to analyze the Spiral Notch Torsion Test (SNTT) results of epoxy samples used for manufacturing wind turbine blade composite. The objective of this study was to estimate the energy release rates and apparent fracture toughness of the epoxy SNTT samples, to provide quantitatively estimate on the epoxy material performance. The SNTT tests were conducted with samples of various notches depths with or without fatigue pre-crack conditions. The effect of a/D ratio to epoxy fracture behavior was also investigated.

3.3.1 Geometries

In the SNTT test, a spiral notch was fabricated along the surface of the cylindrical bar. A schematic diagram of the spiral contour was shown in Figure 12, and the mathematical expression of the spiral curve was also presented in the following paragraphs.

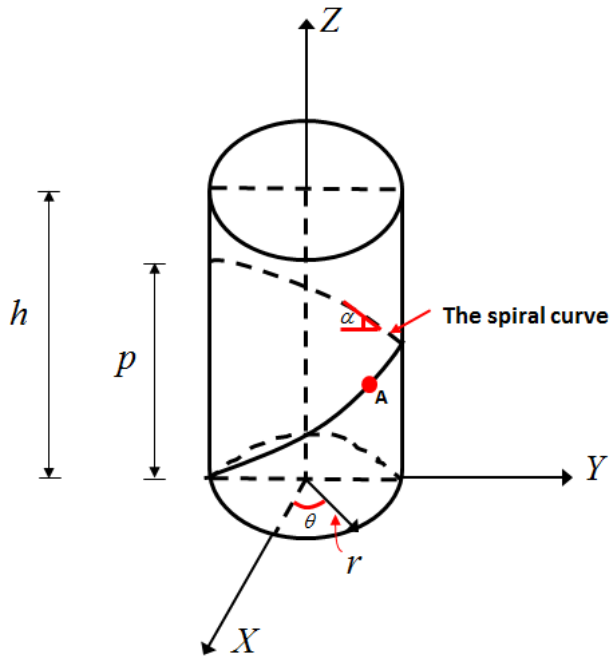

Figure 12. The coordinate system for the spiral notch in SNTT sample

where α is the pitch angle; r is the circle radius of the cylindrical cross section; θ is the rotation angle; p is the pitch length; h is the height of cylinder. X and Y are the axes of the coordinate system in the cross-section plane. Z is the axis of the cylindrical length. For any point $A(x, y, z)$ on the spiral curve, we have

$$x = r\sin\theta \tag{1}$$

$$y = r\cos\theta \tag{2}$$

$$z = p\frac{\theta}{2\pi} \tag{3}$$

In this finite element model, the height of the cylinder, h, was selected to be a quarter of the pitch length, i.e., $0.25p$. Therefore, the spiral rotational angle between the top and bottom of the cylinder, θ_h, was given by:

$$\theta_h = 2\pi\frac{h}{p} = (2\pi)\frac{1}{4} = \frac{\pi}{2} \tag{4}$$

A three dimensional finite element model was established in commercial software Abaqus™ 10.0 (Dassault Systèmes, Providence, RI) [Abaqus 2010]. The model geometry was shown in Figure 13.

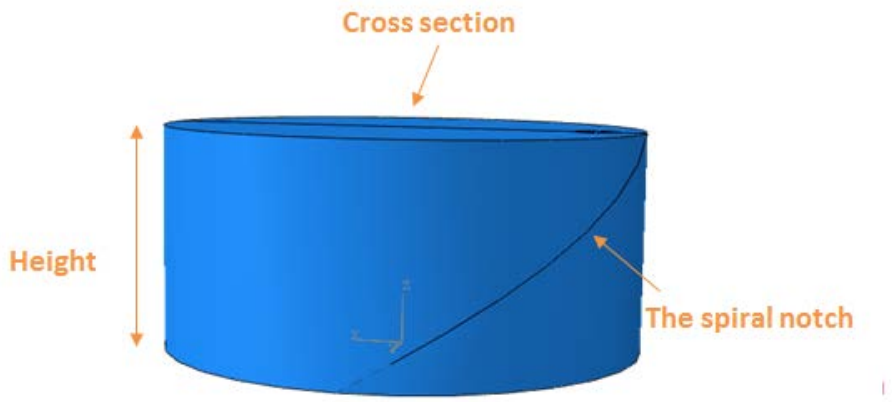

Figure 13. The geometry of the epoxy SNTT model

3.3.2 Meshing

In the finite element model of the epoxy SNTT sample, the spiral notch served as the initiation or starter of a three dimensional (3-D) non co-planar crack front. The associated meshing strategy need to capture the stress concentrations along this spiral crack front, and the energy release rates would be extracted from these stress contours. The model mesh was shown in Figure 14.

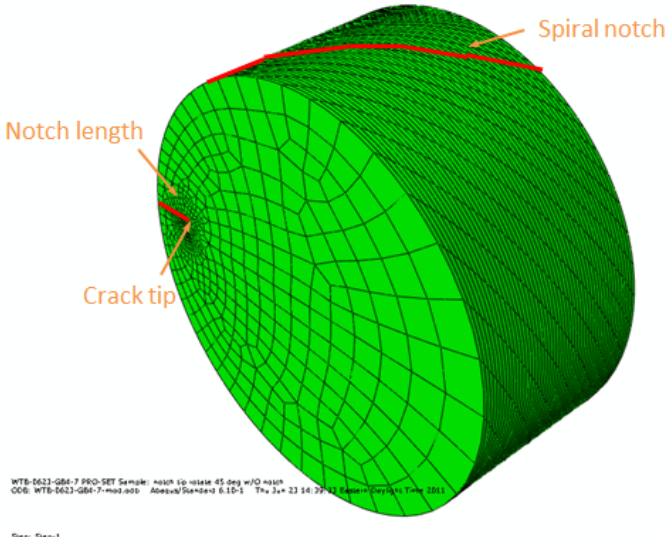

Figure 14. The finite element mesh of the epoxy SNTT sample

Different element types the associated regions were assigned to area A1, A2 and A3 (Figure 15 and Figure 16). In Figure 15, the element C3D20R in Abaqus was assigned to area A1, which was the area outside the red circle. In Figure 16, the crack tip area, i.e., the area inside the red

circle, was shown with higher resolution. The element C3D20R was also assigned to area A2; while the element C3D15 of singular element was assigned to area A3. In areas A2 and A3, the web mesh would be able to capture the stress concentrations along the spiral notch crack front.

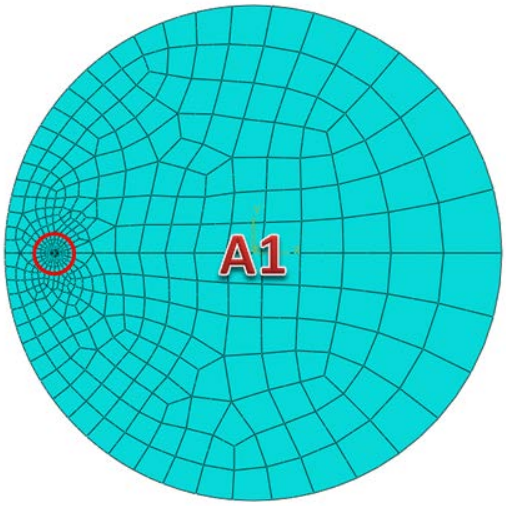

Figure 15. The finite element model mesh in area A1

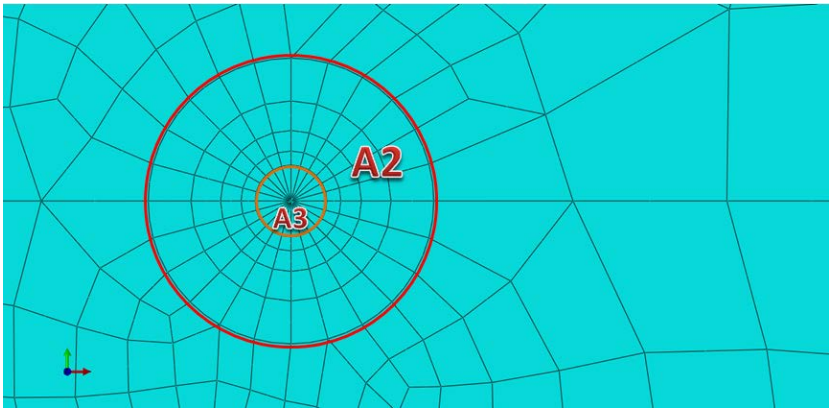

Figure 16. The finite element model mesh in areas A2 and A3

3.3.3 Materials

The epoxy materials used for SNTT samples are made from both Gougeon Brothers (GB) Company and the Molded Fiber Glass (MFG) Company. The epoxy samples of Gougeon Brothers Company included epoxy Pro-Set® 117LV/229 (GB117LV/229) and epoxy Pro-Set® 117LV/XH10B (GB117LV/XH10B). The epoxy samples of Molded Fiber Glass (MFG) Company included Hexion® MGS® RIM135/RIMH1366 (Hexion 135/1366).

All the epoxy materials used in this study were assumed as linear elastic materials. The primary mechanical properties used in the finite element models were summarized in Table 3.

Table 3. Mechanical properties of epoxies used in the FEM study

Material	GB117LV/229	GB117LV/XH10B	Hexion 135/1366
Young's moduli, E (GPa)	3.4 [a]	3.1[a]	3.0 [b]
Poisson's ratio, ν	0.35 [a]	0.35 [a]	0.35 [b]
Density (Kg/m^3)	1150 [a]	1150 [a]	1150 [b]
Tensile strength (MPa)	70	66	60-75
Tensile elongation (%)	3.2	4.3	8-16
Compressive strength (MPa)	102	104	80-90
Impact strength	28.3 J/m	57.6 J/m	70-80 KJ/m^2

[a] Data sheet of epoxy Pro-Set® 117LV/229
[b] Data sheet of epoxy Pro-Set® 117LV/XH10B
[c] Data sheet of epoxy Hexion® MGS® RIM135/RIMH1366

3.3.4 Loading and boundary conditions

The loading and boundary conditions were shown in Figure 17. A concentrated torque was applied at the center of the cross section on one end of the cylinder model. On the other end, the in-plane translations were fixed.

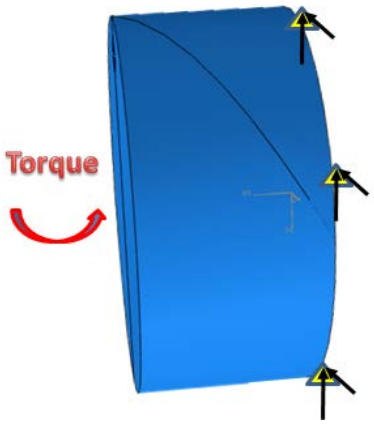

Figure 17. Loading and boundary conditions of the SNTT model

3.3.5 Results and discussions

3.3.5.1 Displacement distributions of the epoxy SNTT sample

In order to illustrate the displacement contour of the epoxy SNTT samples, a cylindrical coordinate system was defined in Figure 18. The tangential and the radial orientations were along with the cross-section circle; while the axial orientation was aligned with the cylindrical axis of the SNTT samples.

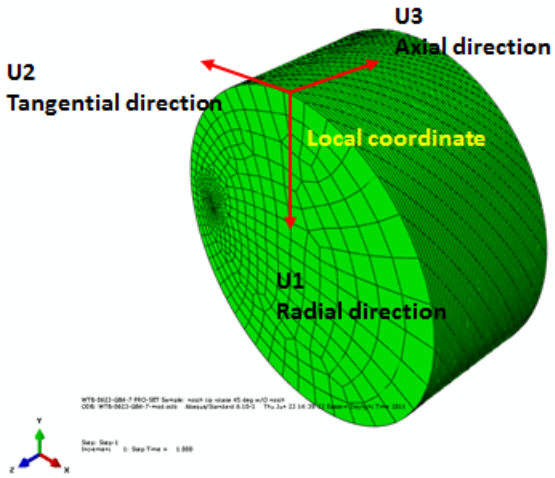

Figure 18. A cylindrical coordinate systme of the SNTT sample

The displacement contour of the deformed epoxy SNTT sample was shown in Figure 19 to Figure 21. The epoxy used in this model was GB 117LV/229. Similar contours were observed for the other two epoxies, i.e., GB117LV/XH10B and Hexion 135/1366.

The numerical results of sample GB3-1 were selected as a representative example for the epoxy SNTT samples in Figures 19 to 21. Figure 19 shows that the maximum radial displacements (red areas) appeared to be on the middle section away from the ends of the spiral notch; which was consistent with displacement of a rotating cylinder. Furthermore, due to pure shear stress loading, the maximum stress contour is located on perimeter or the outer surface of the SNTT samples.

The tangential displacement of the deformed sample GB3-1 was shown in Figure 20. The red contours were areas with zero tangential displacements, corresponding to the fixed surface. The blue contours were the maximum tangential displacement areas, corresponding to the torque applied surface. The gradient located between the red and the blue contours reflected the tangential displacement variation along the spiral notch. And the tangential displacements were around zero in the center area of the torque applied surface; while the tangential displacements are the maximum on the perimeter of the cross-section due to torsion loading.

The axial displacement distributions of the deformed sample GB3-1 were shown in Figure 21. It was shown that the contours of the split halves are symmetrically distributed around the spiral notch crack front. This is due to symmetrical reaction forces of the torsional loading applied to the two halves.

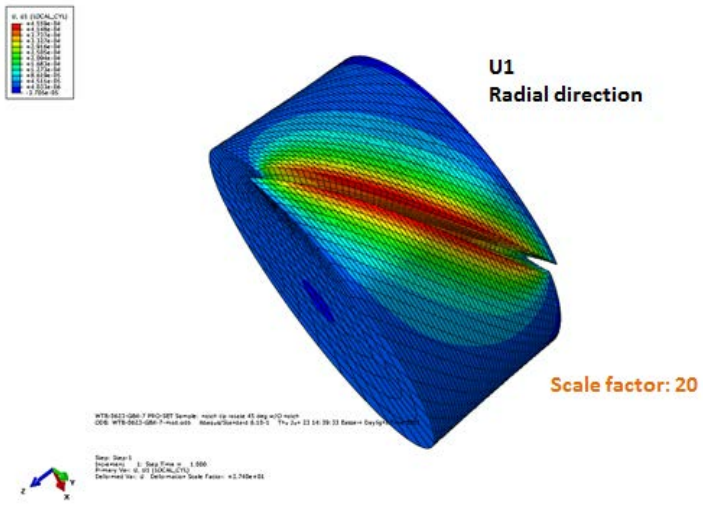

Figure 19. Radial displacement contours of the deformed epoxy SNTT sample

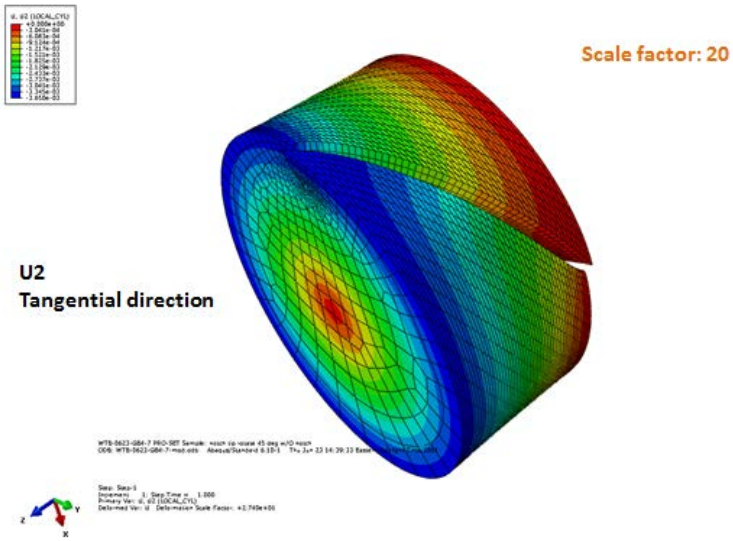

Figure 20. Tangential displacement contours of the deformed epoxy SNTT sample

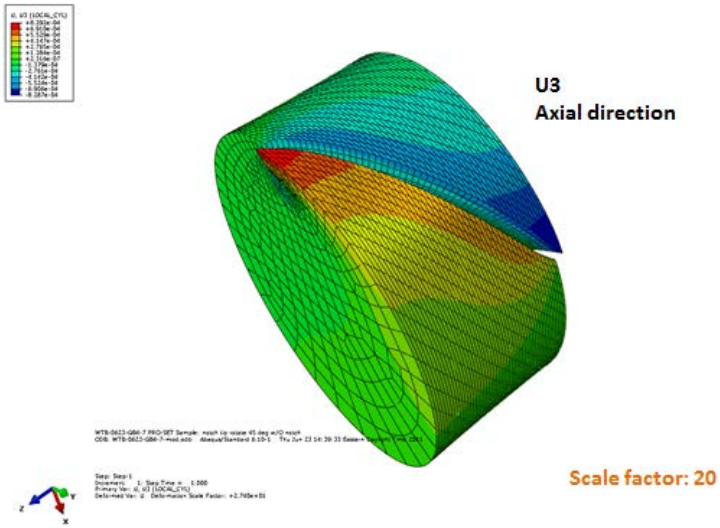

Figure 21. Axial displacement contours of the deformed epoxy SNTT sample

3.3.5.2 Von Mises Stress distributions of the epoxy SNTT sample

The von Mises stress distributions of the deformed sample GB3-1was shown in Figure 22. Similar contours were also observed for the other two epoxy samples.

The stress concentrations phenomenon was observed near the vicinity of the spiral notch. In Figure 23, the von Mises stress distributions around the crack tip were illustrated with a cross-section view. The deformed notch root blunting was clearly presented; while the butterfly plastic process zone was also captured by the wedge element mesh.

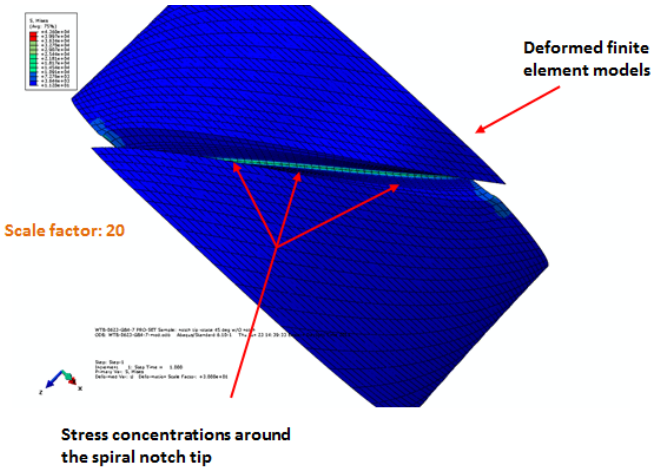

Figure 22. Von Mises stress contours of the deformed epoxy SNTT sample

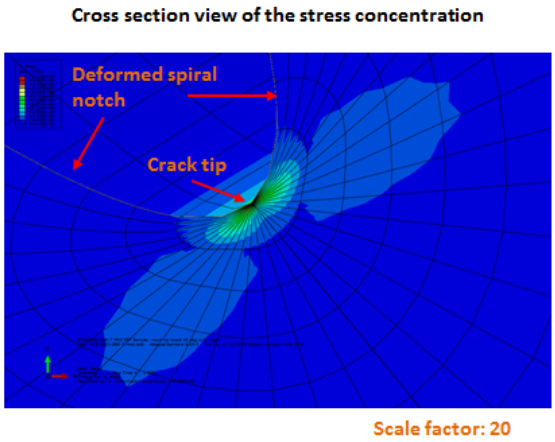

Figure 23. Von Mises stress contours near the crack tip of the epoxy SNTT sample

3.3.5.3 Statistics analysis of epoxy SNTT samples

Epoxy GB117LV/229

The energy release rates of epoxy GB117LV/229 obtained at different scenarios are shown in Figure 24 and Figure 25. The energy release rates obtained under mode I failure are shown in Figure 24; while the results obtained under mixed mode lading are shown in Figure 25. For these three-dimensional figures, one axis is for sample identification with the pitch angle in the brackets, and the other axis is the notch depth to sample diameter (a/D) ratio of the epoxy SNTT samples. The vertical axis is the energy release rates obtained from FEA.

For samples of Mode I scenario, Figure 24 shows that the energy release rates are comparable among the samples, i.e., GB3-1, GB3-6, GB4-1, GB4-4. The a/D ratios were around 0.1, and the energy release rates were around 0.5 kN/m. For fatigue samples with detectable fatigue pre-crack length, i.e., GB 3-3, GB4-3 and GB 4-6, the ranges of a/D ratios were between 0.12 and 0.15, and the energy release rates were around 0.35 kN/m. Thus, lower toughness was observed for samples with fatigue pre-crack growth compared to that of the samples without fatigue crack growth.

Sample GB 4-9 failed during the sample fatigue pre-crack process. Its energy release rate was much lower than the other samples. During the dynamic fatigue pre-process, the loading rate was about two orders of magnitudes higher than that of SNTT fracture testing. The consequence of increased loading rate will result in the increase of epoxy yield stress; and this will result in the decrease of the fracture toughness.

The energy release rates estimated from available mixed-mode samples appeared to have wide spectrum (Figure 25). The energy release rates of mixed mode samples seemed to be higher than that of the Mode I samples. For the mixed-mode samples, those failed along the 45° principle stress plane had much higher fracture toughness than the samples failed along the initial mixed-mode spiral crack front.

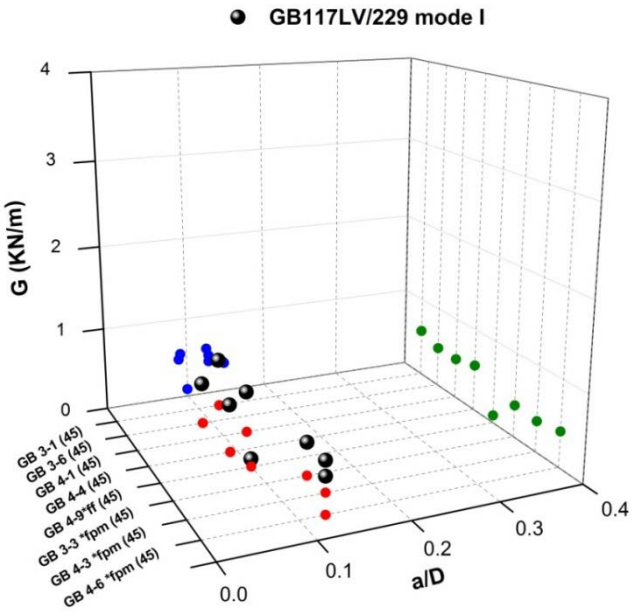

***fpm**: Samples are failed by monotonic loading with detected pre- fatigue crack length

***fm**: Samples are failed during the monotonic loading process without detected pre-fatigue crack length

***ff**: Samples are failed during the fatigue process without detected pre-fatigue crack length

Figure 24. Energy release rates of epoxy GB117LV/229 at mode I failure

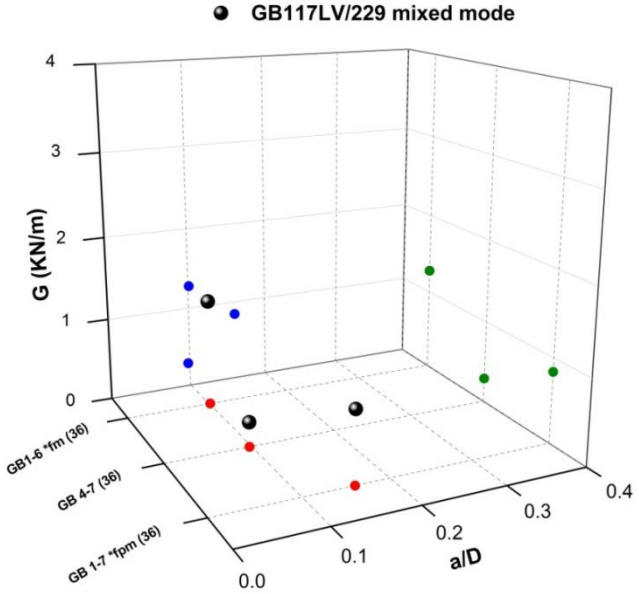

***fpm**: Samples failed by monotonic loading with detected pre- fatigue crack length

***fm**: Samples failed during the monotonic loading process without detected pre-fatigue crack length

***ff**: Samples failed during the fatigue process without detected pre-fatigue crack length

***pitch angle:** degrees in the

Figure 25. Energy release rates of epoxy GB117LV/229 at mixed mode failure

Epoxy GB117LV/ XH10B

The energy release rates of epoxy GB117LV/ XH10B obtained at different scenarios were shown in Figure 26 and Figure 27. The energy release rates obtained under mode I failure were shown in Figure 26; while the results obtained under mixed mode failure were shown in Figure 27. The axes were the same definitions as those used in previous figures.

For samples failed at mode I scenario (Figure 26), it was shown that the energy release rates were comparable among samples failed under typical loading rate, i.e., GB5-1, GB5-3 and GB5-4. For these samples, the a/D ratios varied between 0.1 and 0.3. The estimated energy release rates were around 0.6 kN/m.

Sample GB 5-5 failed during the fatigue pre-crack process without detectable fatigue pre-crack; while sample GB5-6 failed during the fatigue pre-crack process with detectable fatigue pre-crack. The estimated energy release rates for them were around 0.15 kN/m, which was significantly lower than that of lower strain-rate testing data. This loading rate dependent toughness behavior was also observed from epoxy samples made of GB117LV/229 material.

For samples failed at mixed mode scenarios (Figure 27), the energy release rates of samples failed at mixed mode appear to be higher than that of mode I samples. The energy release rates have wide spectrum from samples, i.e., GB 2-1, GB 2-6, GB5-9, and GB2-2. Sample GB2-2 had undergone fatigue pre-crack process without detachable fatigue crack. The sample GB5-9 haD lowest energy release rate, partially due to a high a/D ratio of 0.3. This sample fractured along the initial mixed-mode spiral crack front.

For sample GB2-7, the associated energy release rate appeared to be significantly lower than that of the other mixed-mode samples. This sample failed during SNTT testing but with notable axial loading increased to 332 lb upon fracture. The cause might be that highly localized constraint enforced by the axial loading at the crack front decreased the apparent fracture toughness.

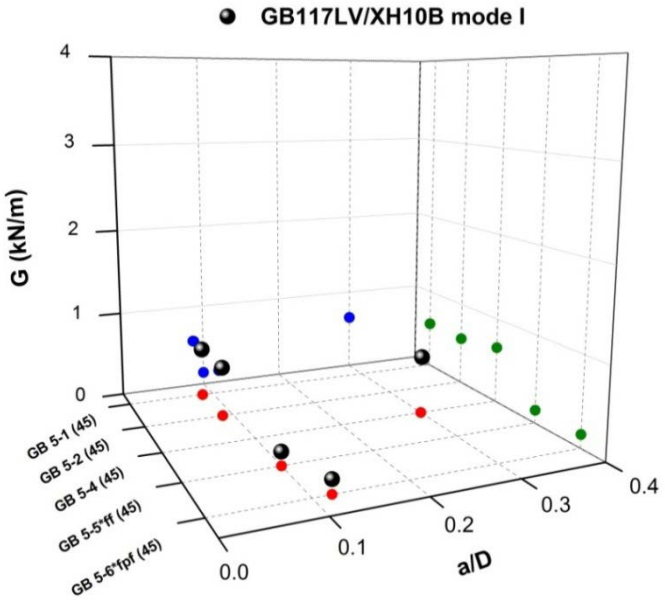

***ff**: Samples failed during the fatigue process without detected fatigue precrack length

***fm**: Samples failed during fracture testing without detected fatigue precrack length

***fpf**: Samples failed during the fatigue process with detected fatigue precrack length

***faf:** Samples failed during the fatigue process without detected fatigue precrack length under axial forces

***pitch angle:** degrees in the brackets

Figure 26. Energy release rates of epoxy GB117LV/XH10B at mode I failure

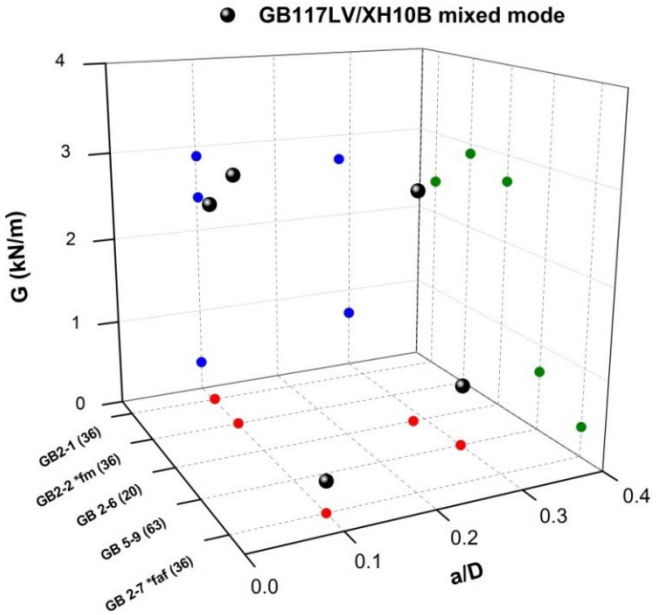

***ff**: Samples failed during the fatigue process without detected fatigue precrack length

***fm**: Samples failed during fracture testing without detected fatigue precrack length

***fpf**: Samples failed during the fatigue process with detected fatigue precrack length

***faf:** Samples failed during the fatigue process without detected fatigue precrack length under axial forces

Figure 27. Energy release rates of epoxy GB117LV/XH10B at mixed mode failure

Epoxy Hexion 135/1366

The energy release rates of epoxy Hexion 135/1366 at mode I failure were shown in Figure 28. Large variation of the energy release rates from SNTT tested samples, i.e., MFG-1 and ORNL-1, could be observed. The energy release rates of samples failed during the fatigue pre-crack process, i.e., MFG-2 and MFG-3, showed much less toughness that those of regular SNTT tested samples of similar a/D ratios. The energy release rates of samples failed under fracture loading with detachable fatigue pre-crack, i.e., MFG-5 and MFG-6, also had lower toughness, i.e., 0.84 kN/m, compared to that of samples without fatigue pre-crack.

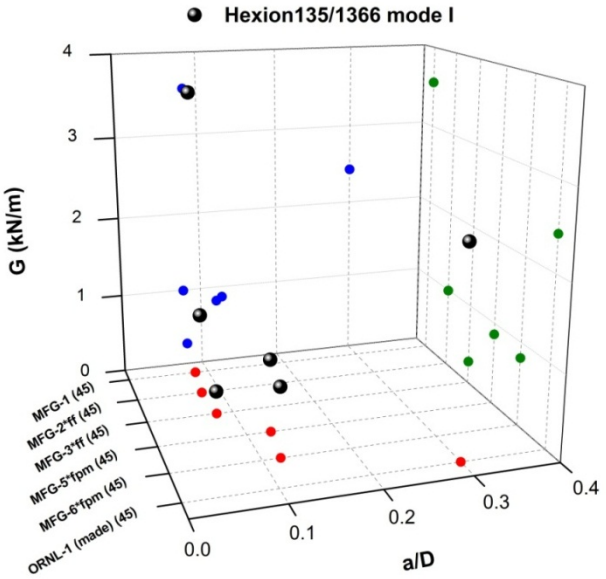

***fpm**: Samples failed during fracture testing with detected fatigue precrack length

***ff**: Samples failed during the fatigue process without detected fatigue precrack length

***pitch angle:** degrees in the brackets

Figure 28. Energy release rates of epoxy Hexion135/1366 at mode I failure

The evaluated fracture toughness data for epoxy SNTT tests were summarized in table 4. It was shown that the sample with noticeable fatigue pre-crack growth had lower toughness than that of sample without fatigue pre-crack in mode I fracture, due to higher constraint of a tested sample with sharp crack front.

The overall fracture toughness obtained from some mixed mode (Mode I + Mode III) samples, with fracture surface of 45° spiral crack front contour, had higher toughness than that of Mode I toughness. However, for second batch epoxy SNTT samples, the apparent mixed-mode fracture toughness with fracture surface along 36° spiral crack front contour showed much lower fracture toughness than that of Mode I samples.

The epoxy 117LV/XH10B was higher in apparent fracture toughness than that of epoxy 117LV/229 for both mode I and mixed mode failures. The epoxy Hexion 135/1366 is higher in fracture toughness than that of epoxy 117LV/XH10B and 117LV/229 for mode I failure.

The fracture toughness of samples failed during the fatigue pre-crack process appeared to be significantly lower in than of samples failed undergoing typical SNTT fracture test, due to higher loading rate.

Table 4. Summary of apparent fracture toughness for epoxy SNTT samples.

	Apparent Fracture Toughness, K_{eff} ($MPa\sqrt{m}$)			
	Mode I, K_Q		Mixed Mode (Mode I + Mode III), K_{MC}	
Materials	Without fatigue	With fatigue	Without fatigue	With fatigue
117LV/229	1.50 (GB3-1) 1.38 (GB3-6) 1.38 (GB4-1) 1.47 (GB4-4)	1.22 (GB3-3*fpm) 1.18 (GB4-3*fpm) 1.27 (GB4-6*fpm) 0.60 (GB4-9*ff)	1.00 (GB4-7, 36^o)	2.23 (GB1-6*fm, 36^o) 1.81 (GB1-7*fpm, 36^o)
117LV/XH 10B	1.42 (GB5-1) 1.41 (GB5-2) 1.47 (GB5-4)	0.73 (GB5-5*ff) 0.74 (GB5-6*fpf)	2.92 (GB2-1, 36^o) 3.10 (GB2-6, 20^o) 1.57 (GB5-9, 63^o) 1.11 (GB2-7*faf, 36^o)	3.24 (GB2-2 *fm, 36^o)
Hexion 135/1366	3.49 (MFG-1) 2.98 (ORNL-1)	1.72*fpm (MFG-5) 1.67*fpm (MFG-6) 1.82*ff (MFG-2) 0.97*ff (MFG-3)		

Notice :
***fpm:** Samples failed in fracture testing with detected pre-fatigue crack length;
***ff:** Samples failed during the fatigue process without detected pre-fatigue crack length;
***fm:** Samples failed in fracture testing without detected pre-fatigue crack length;
***fpf:** Samples failed during the fatigue process with detected pre-fatigue crack length;
***faf:** Samples failed during the fatigue process without detected pre-fatigue crack length under axial forces;
***pitch angle:** degrees in the brackets.

Table 5 Summary of energy release rate and stress intensity factors for epoxy SNTT samples.

Epoxy								
	a/D	theta	G	K_{eff}	K_I	K_{II}	K_{III}	Notice
Units		degree	kN/m	MPa$\sqrt{m}$	MPa$\sqrt{m}$	MPa$\sqrt{m}$	MPa$\sqrt{m}$	
GB1-6*fm	0.10	36	1.28	2.23	2.14	0.00	0.52	1st batch, failed at 45° plane
GB1-7*fpm	0.16	36	0.84	1.81	1.74	0.00	0.42	1st batch, failed at 45° plane
GB3-1	0.13	45	0.58	1.50	1.51	0.00	0.03	
GB3-3*fpm	0.15	45	0.38	1.22	1.22	0.00	0.01	
GB3-6	0.09	45	0.49	1.38	1.38	0.00	0.00	
GB4-1	0.13	45	0.49	1.38	1.38	0.00	0.03	
GB4-3*fpm	0.15	45	0.36	1.18	1.18	0.00	0.01	
GB4-4	0.09	45	0.55	1.47	1.47	0.00	0.00	
GB4-6*fpm	0.13	45	0.41	1.27	1.27	0.00	0.01	
GB4-7	0.10	36	0.26	1.00	0.96	0.00	0.23	2nd batch, failed at 36° plane
GB4-9*ff	0.10	45	0.09	0.60	0.60	0.00	0.00	
GB2-1	0.10	36	2.39	2.92	2.80	0.00	0.67	Failed at 45 plane
GB2-2*fm	0.10	36	2.95	3.24	3.11	0.00	0.75	Failed at 45 plane
GB2-6	0.29	20	2.70	3.10	2.23	0.00	1.74	
GB2-7*faf	0.10	36	0.34	1.11	1.10	0.01	0.11	Axial: 332 lbs
GB5-1	0.09	45	0.56	1.42	1.42	0.00	0.00	
GB5-2	0.09	45	0.56	1.41	1.41	0.00	0.00	
GB5-4	0.30	45	0.65	1.53	1.47	0.00	0.35	
GB5-5*ff	0.10	45	0.15	0.73	0.73	0.00	0.00	
GB5-6*fpf	0.12	45	0.15	0.74	0.74	0.00	0.01	
GB5-9	0.30	63	0.69	1.57	1.55	0.00	-0.19	
MFG-1	0.08	45	3.56	3.49	3.49	0.00	0.00	
MFG-2*ff	0.08	45	0.99	1.84	1.84	0.00	0.00	
MFG-3*ff	0.08	45	0.28	0.97	0.97	0.00	0.00	
MFG-5*fpm	0.13	45	0.86	1.72	1.72	0.00	0.02	
MFG-6*fpm	0.12	45	0.82	1.67	1.67	0.00	0.00	
ORNL-1	0.30	45	2.43	2.98	2.86	0.00	0.69	

4. Testing and analysis of composite materials

4.1 Sample design and fabrication

Although SNTT has been successfully applied to various types of materials, it is the first time to utilize SNTT to study polymer/fiber composite materials. Although SNTT has been successfully applied to various types of materials, it is the first time to utilize SNTT to study polymer/fiber composite materials. During the first quarter of FY11, an extensive study was performed to test the viability of various approaches to fabricate composite samples suitable for SNTT testing. This study was carried out through collaboration between Oak Ridge National Laboratory and Montana State University. The details of sample design and results from fabrication trials are included in the attached FY11 Q1 report (Appendix B). This section will highlight some important findings from this joint effort.

4.1.1 Co-cured sandwich laminate

In this approach, a resin/composite/resin sandwich structure (Figure 29a) would be fabricated from a co-curing process and SNTT samples could be machined from the co-cured structure (Figure 29b).

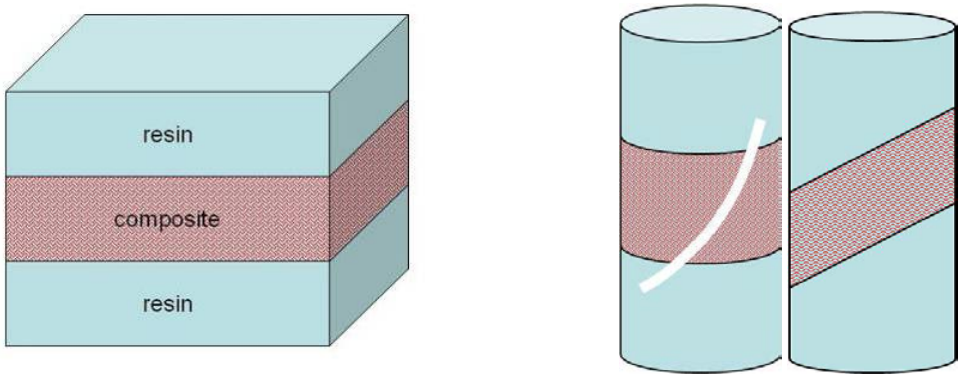

(a) (b)

Figure 29. Schematic diagrams showing (a) a co-cured sandwich laminate, and (b) SNTT samples machined from the sandwich structure.

Three stacks of E-LT5500 fabric were cut into 6”×1.5” pieces placed equidistance apart under a 0.5” glass plate. The fabric and glass plate were vacuum-bagged with extra tortuous path entering the vent port. Two pilot experiments were carried out: 1) 30 layers of precut fabric, off-centered in the mold with bottom injection and vent; and 2) 15 layers of fabric precut, centered in the mold, bottom injection and top vent. Schematic of the setup and actual setup are illustrated in Figure 30 and Figure 31, respectively.

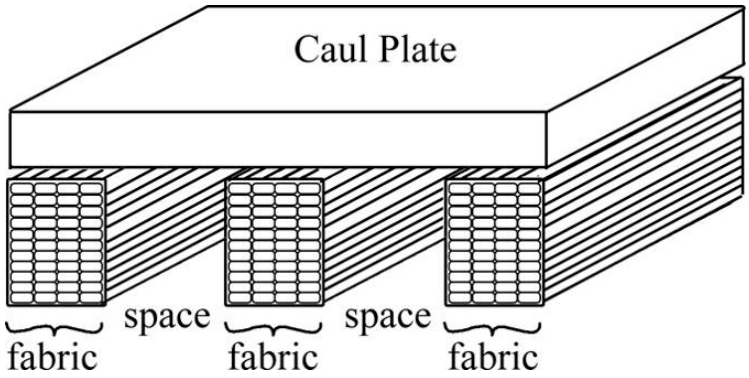

Figure 30. Schematic for sandwich test specimen between the vacuum bag material and the aluminum mold.

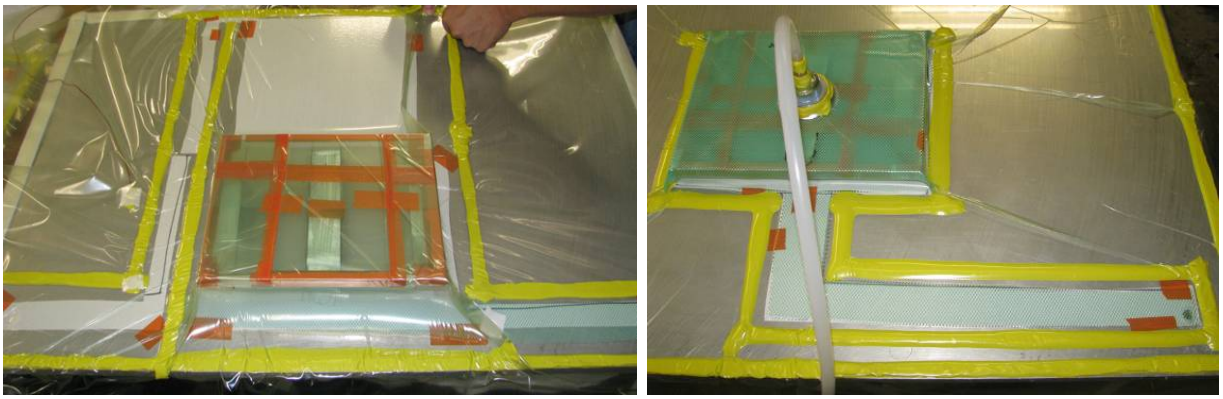

(a) (b)

Figure 31. Pictures showing (a) the vacuum-bagging step, and (b) the infusion process.

However, this approach was proved to be very difficult. During the infusion process, resin flow entered the exit port leaving a large volume of empty space between the fabric stacks (Figure 32). Lots of air bubbles remained in the infused fabrics. Thus, it was concluded that this approach was not appropriate using the current setup.

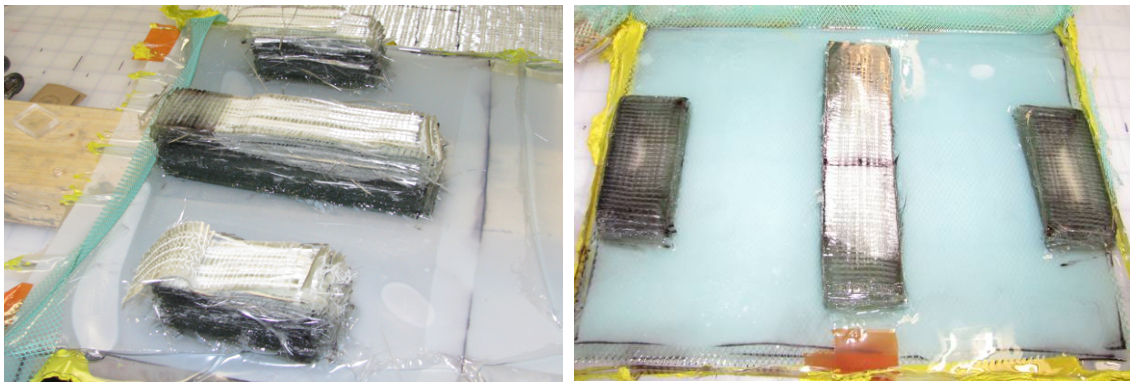

Figure 32. Pictures of failed samples from (a) the first and (b) the second attempts.

4.1.2 SNTT samples machined from bulk composite plates

The unsuccessful fabrication of sandwich laminates prompted the idea of machining SNTT test samples from a bulk piece of composite laminate. Using the vacuum assisted infusion technique (Figure 33a), composite plates were fabricated (Figure 33a). These plates consisted of 20 layers of unidirectional fabrics stitched to 90^{o} (E-LT 5500-10, Vectorply Corp. Phenix City, AL), were infused with Epikote® RIMR 135 resin/Epikure® RIMH1366 curing agent (Momentive, Columbus, OH). The resin to curing agent weight ratio was 100:30. The infused plates were cured at 70^{o}C for 8 hours.

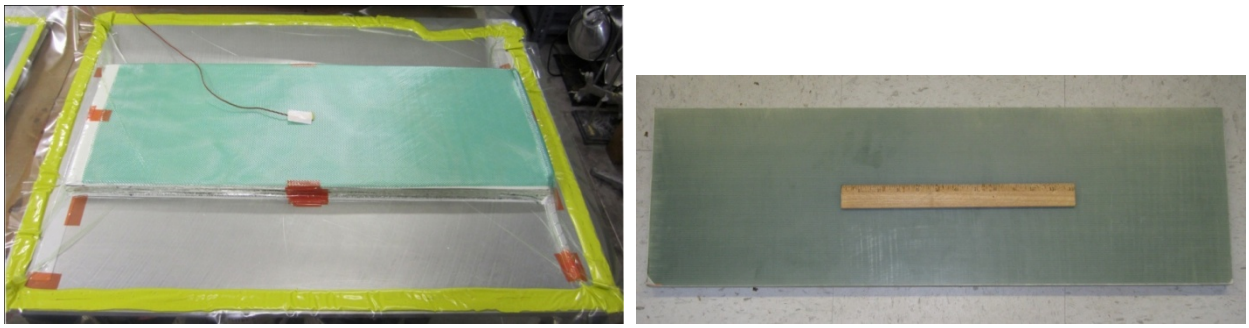

(a) (b)

Figure 33. (a) Vacuum assisted infusion process for composite fabrication, and (b) a finished composite plate.

The geometry of the composite SNTT samples is illustrated in Figure 34. Three types of SNTT samples (Figure 35a) were machined from composite plates: 1) type A – sample axis perpendicular to fibers (Figure 35b); 2) type B – sample axis parallel to fibers (Figure 35c); and 3) type C – sample axis was 45^{o} to fibers (Figure 35d).

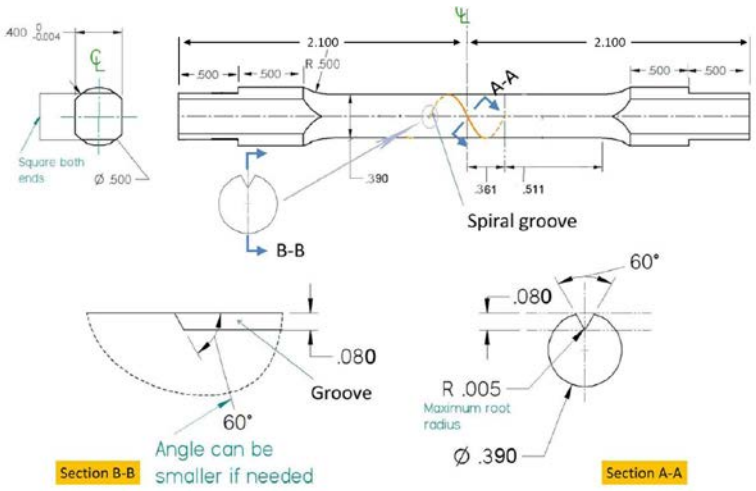

Figure 34. The geometry of the composite SNTT samples.

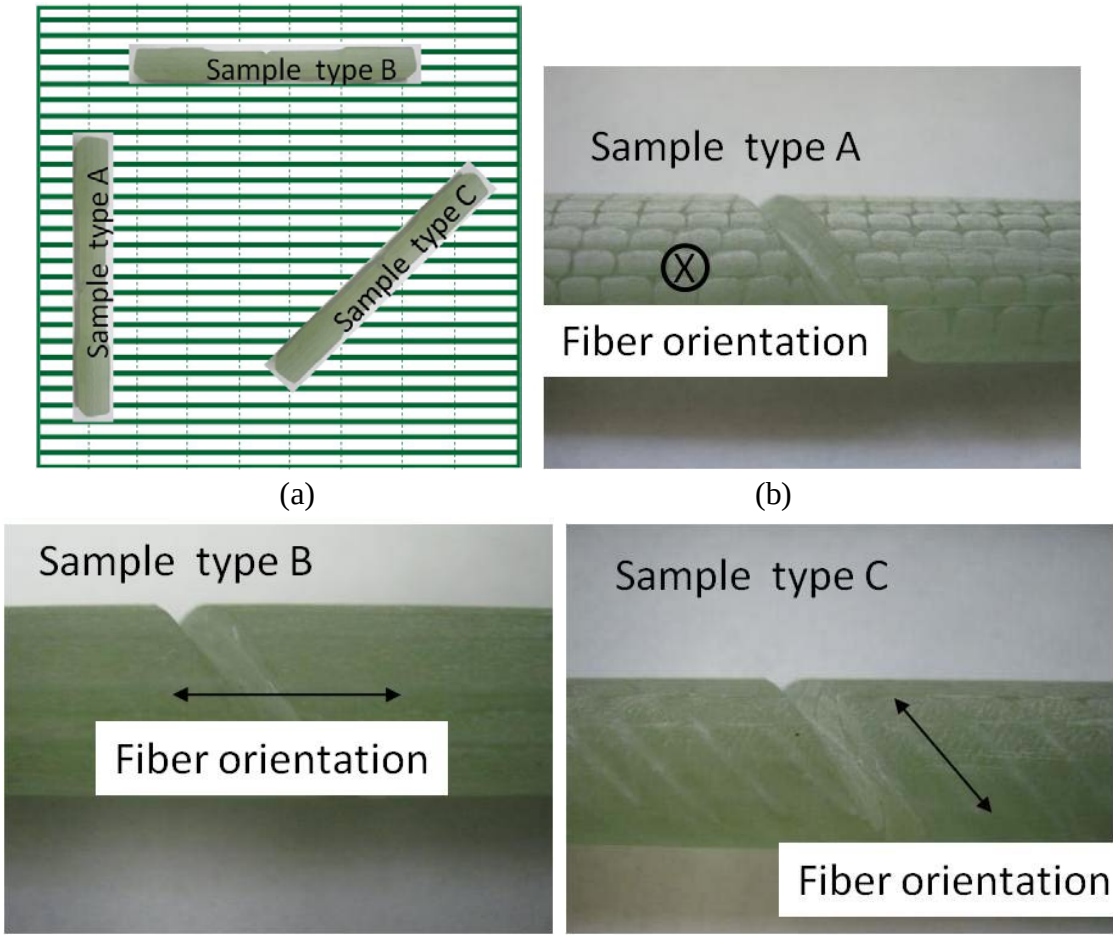

Figure 35. (a) The schematic showing the orientations of three types of SNTT samples; and pictures of (b) type A, (c) type B, (d) type C samples.

4.1.3 Strand embedment and infusion

In the third approach, an epoxy sample with a spiral notch would be first machined. A strand of glass fiber would be embedded in the notch and then infused using resin (Figure 36).

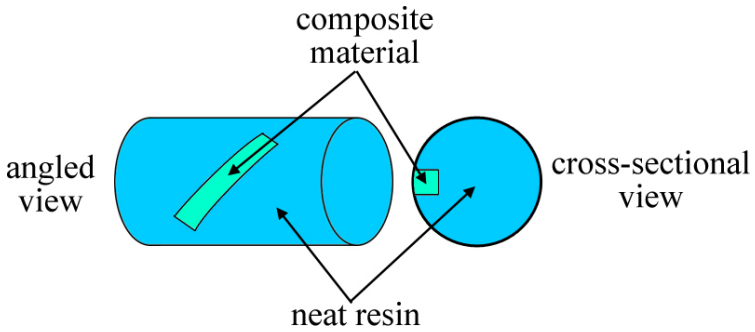

Figure 36. Schematic of an epoxy SNTT sample with glass fiber embedded in the groove.

Experimentally, glass fiber strands were placed inside the groove of an epoxy SNTT sample (Figure 37a) and then sealed with a Nylon sheet, tacky tape, and rubber bands (Figure 37b). Resin was then infused under vacuum and the sample was cured afterwards. The completed sample was shown in Figure 38. However, the fiber strands were only partially saturated with small air bubbles trapped in the groove (Figure 38b). The partial saturation could be reduced by slowing down the infusion speed in the future.

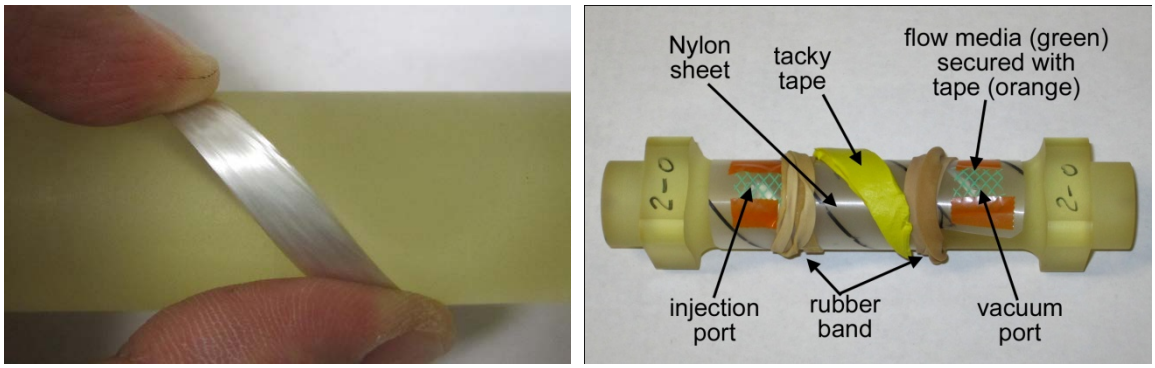

(a) (b)

Figure 37. Pictures showing (a) the glass fibers placed in the groove, and (b) the securely sealed sample.

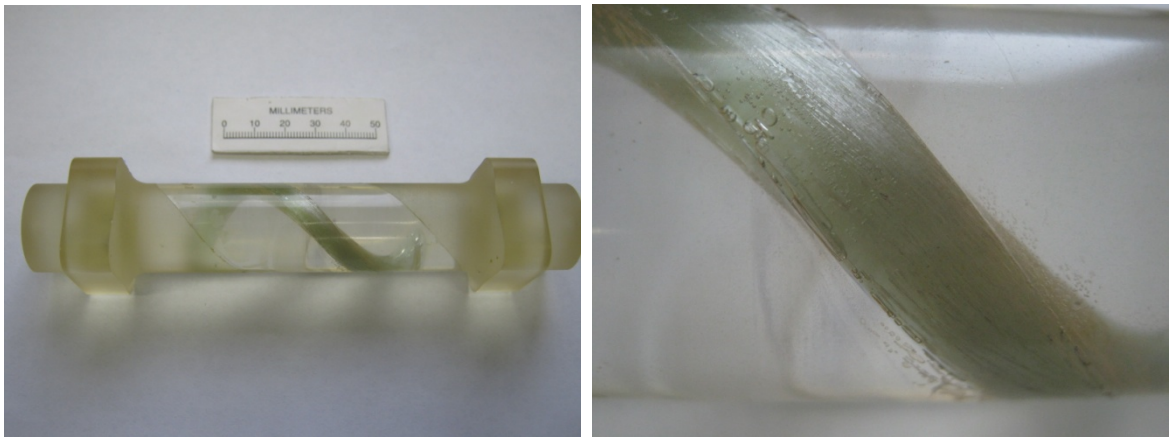

(a) (b)

Figure 38. Pictures showing the completed strand-embedded sample.

4.1.4 Epoxy infusion of composite bars

A similar approach was used to infuse the groove of composite SNTT samples. The machined composite bar was first sealed with a piece of Nylon sheet, tacky tape, and rubber bands (Figure 39a). Two holes were punched on the Nylon sheet near the end of the spiral notch. The resin/hardener mixture was then injected using a syringe. Curing was first performed at room temperature over night and then at 60^{o}C for 6 hours. A cured sample is shown in Figure 39b. The infused samples were free of air bubbles along most of the notch length (Figure 40a) except at the ends of the groove (Figure 40b).

(a) (b)

Figure 39. Pictures showing a composite SNTT sample (a) before and (b) after resin infusion.

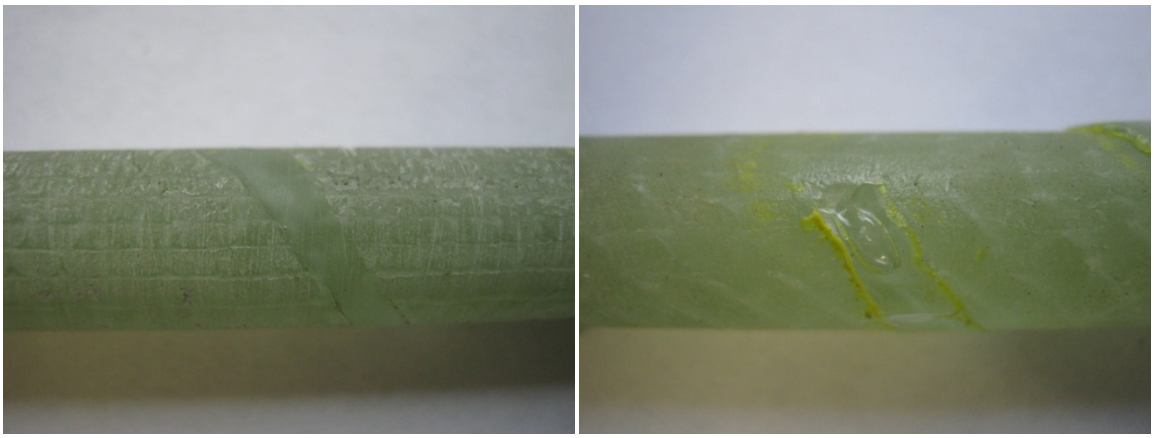

(a) (b)

Figure 40. Detailed view of an infused sample (a) in the middle section and (b) near the notch end.

The infusion processes described here and in Section 4.1.3 seemed promising methods for fabricating composite/resin SNTT samples, where interfacial regions are of special interest. However, the infusion quality needs to be improved in the future to minimize artificial defects such as air bubbles.

4.2 SNTT equipment setup

To date, the SNTT testing of composite materials has been focused on samples machined from the bulk composite plates (see Section 4.1.2). Preliminary testing indicated these samples would fail under an applied torque of approximately 60 lbf-in or less. The capacity of the load/torque cell equipped on the MTS 809 machine is 10000 lbf-in. In order to obtain a higher accuracy in measured torques, an auxiliary torque cell with a capacity of 200 lbf-in (Model 2102-200, Honeywell, Golden Valley, MN) was installed (Figure 41).

The output voltage from the 200 lbf-in torque was first conditioned using a balance unit (SB-10, Vishay, Shelton, CT) and a strain indicator (Model 3800, Vishay, Shelton, CT), and then collected by a computer. By comparing the voltage reading from the 200 lbf-in torque cell and

the torque value measured by the MTS load/torque cell, a linear relationship was established between the torque and the voltage for the 200 lbf-in torque cell (Figure 42).

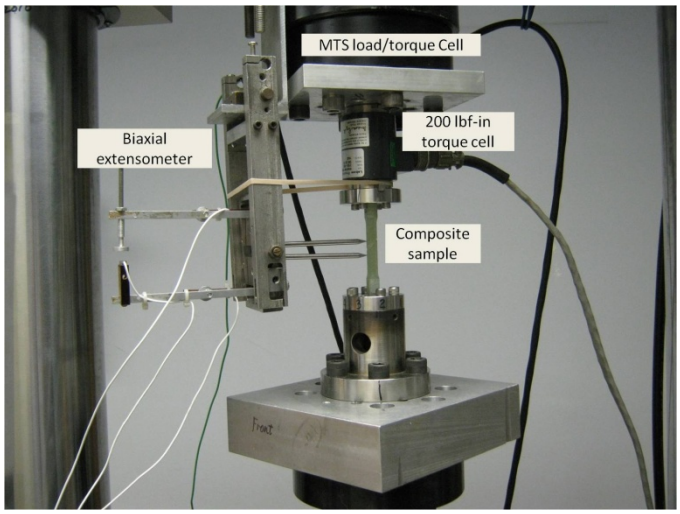

Figure 41. SNTT testing setup of composite bars using a 200 lbf-in torque cell.

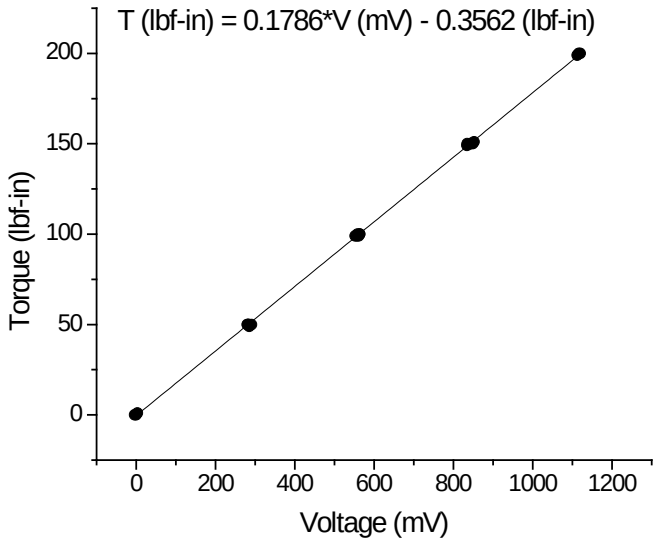

Figure 42. Torque-voltage calibration curve for the 200 lbf-in torque cell.

Figure 43 shows the comparison between the data measured by the MTS load/torque cell and the 200 lbf-in torque cell during the measurement of a composite bar sample. It is evident that the 200 lbf-in torque cell has a higher resolution and a lower noise level in the torque range relevant to this study.

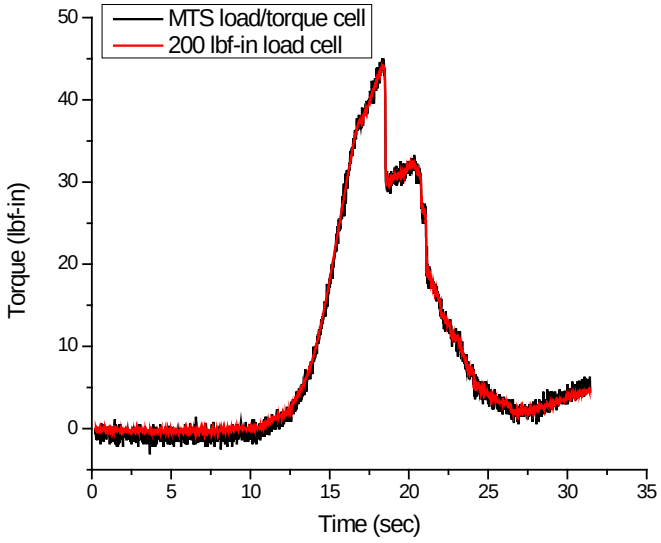

Figure 43. Comparison between the data obtained from the MTS load/torque cell and the 200 lbf-in torque cell.

4.3 SNTT testing of composite samples

4.3.1 A-type samples

Using an infrared (IR) camera (Model A325, FLIR Systems, Inc. Boston, MA), the complete loading process was recorded on an A-type sample (#A-13). In Figure 44, the grey level was related the apparent temperature with a brighter region corresponding to a higher temperature. Initially, a bright spot was observed along the spiral notch (Figure 44b), indicating this location had a higher temperature than the surrounding area. This temperature rise was likely due to the release of surface energy when a crack formed. Thus, this location was likely the fracture origin. With increasing torque, the bright region extended to the entire length of the spiral notch (Figure 44c), implying the crack propagated along the notch. The IR image at failure is shown in Figure 44d, where a large amount of released surface energy is indicated by the brightness on the fracture surfaces.

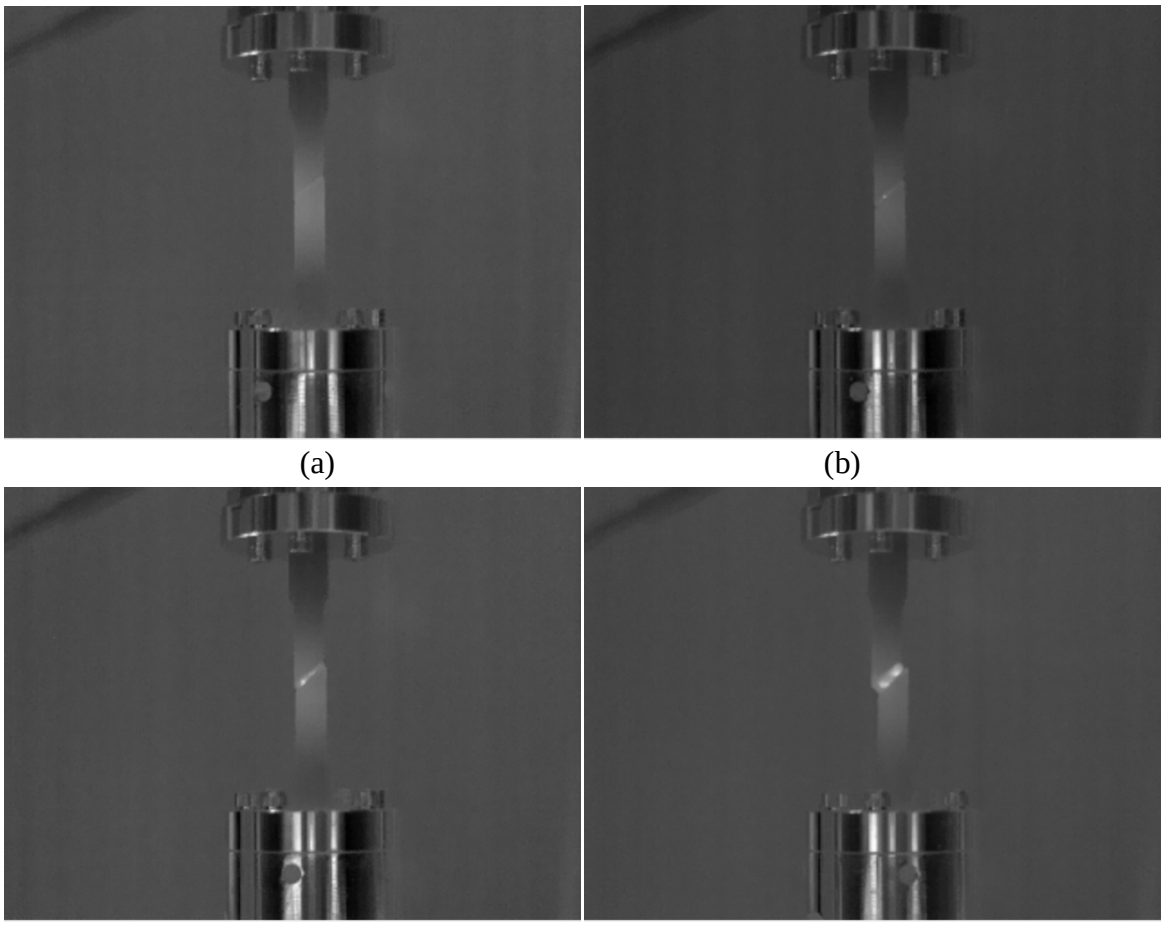

(a) (b)

(c) (d)

Figure 44. Infrared images obtained during the testing of an A-type sample (#A-13). The images were taken (a) at the start of the testing, (b) at a potential moment for crack initiation, (c) during the crack propagation, and (d) after the complete separation of the sample.

All A-type samples were completed separated into halves after SNTT testing (Figure 45a). Macroscopic failure modes included weft fiber failure, and strand delamination. On the fracture surface, it can be clearly seen that the fracture took place along the spiral notch and the crack propagation direction was parallel to the fiber orientation (Figure 45b, Figure 46a).

Figure 46b is a backscattered electron image, in which the dark regions were epoxy resin and the grey columns were glass fibers. The fiber surfaces were very smooth with litter residual resin, implying interfacial debonding took place. River lines were observed in the resin region, which were evidence of crack propagation through the matrix. Thus, the dominant failure modes at the microscopic level included fiber/resin interfacial debonding and resin matrix cracking.

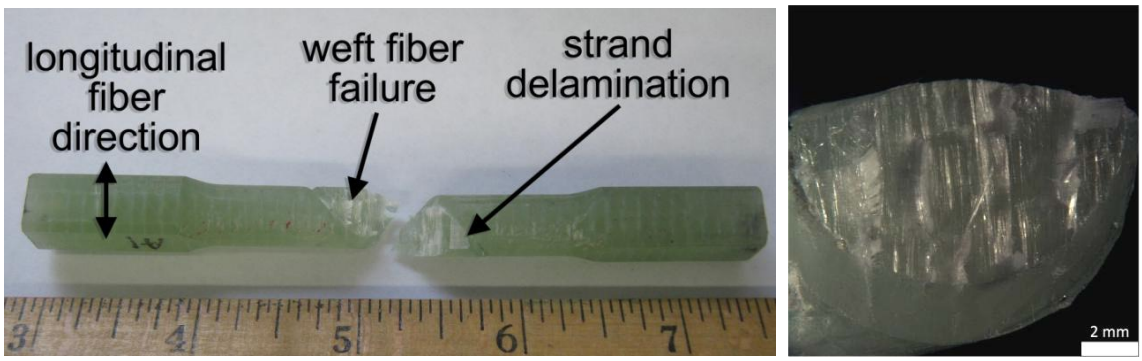

(a) (b)

Figure 45. Images showing (a) a failed A-type sample (#A-1) and (b) its fracture surface.

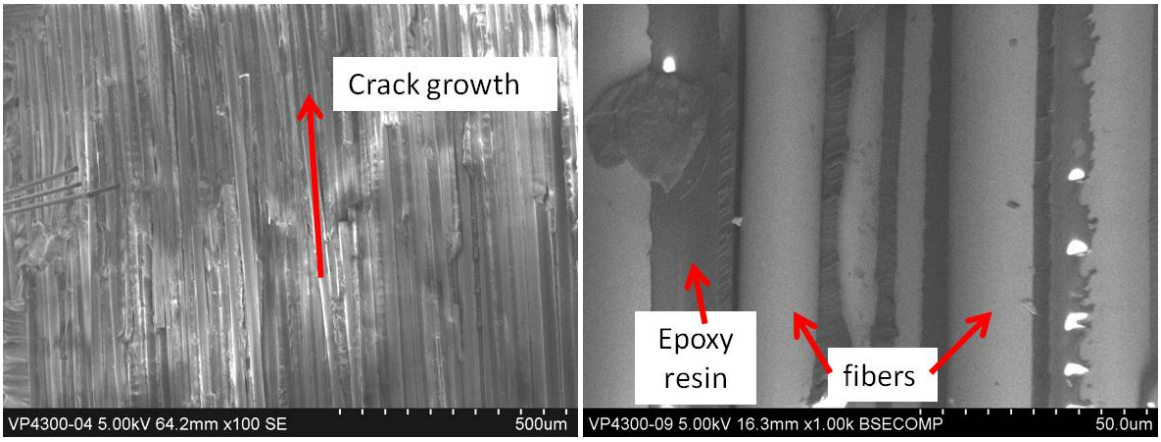

(a) (b)

Figure 46. SEM images of the fracture surface of a failed A-type sample (#A-1).

4.3.2 B-type samples

In contrast to the A-type sample where crack initiated at one location (Figure 44), no single bright spot was observed from the IR imaging results during the testing of a B-type sample (#B-12). Instead, the crack seemed to initiate uniformly (Figure 47a) and propagated (Figure 47b) along the spiral notch.

Due to the constraint of the glass fibers running along the sample axis, the primary crack in B-type samples could not propagate through the center of the sample. All B-type samples were held together by fibers after failure (or crack initiation), no complete separation was observed (Figure 48a). On the other hand, cracks running parallel to the sample axis were observed on the opposite sample surface near the end regions of the spiral notch (Figure 48b). This portion of SNTT sample is at the opposite site of tensile crack initiation site and in line with the maximum shear stress contour.

The cross-section view of the failed sample (Figure 48c) revealed that multiple fractures took place within the sample volume. Three crack systems were evident: 1) cracks along the fabric interfaces; 2) cracks between the fiber strands; and 3) a circular crack whose perimeter approximately corresponded to the projection of the spiral notch on this cross-section plane (Figure 48c). Thus, although no complete separation was observed in B-type samples, multiple delamination events occurred internally. Thus, the interfacial regions seemed to be the most vulnerable in this sample geometry/loading configuration.

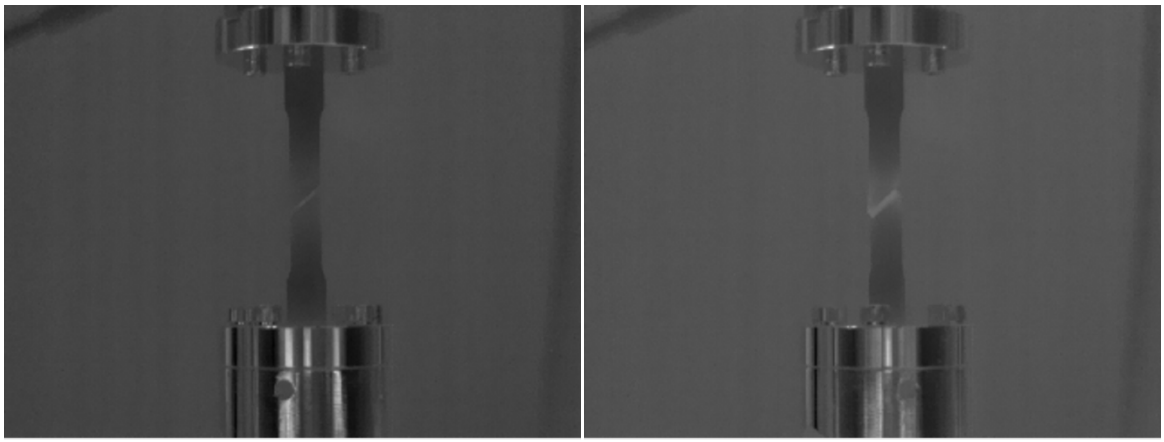

(a) (b)

Figure 47. IR images showing the loading of a B-type sample (#B-12) (a) when a crack initiated and (b) further propagated.

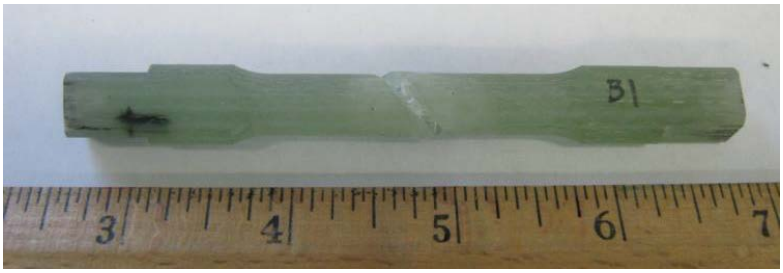

(a)

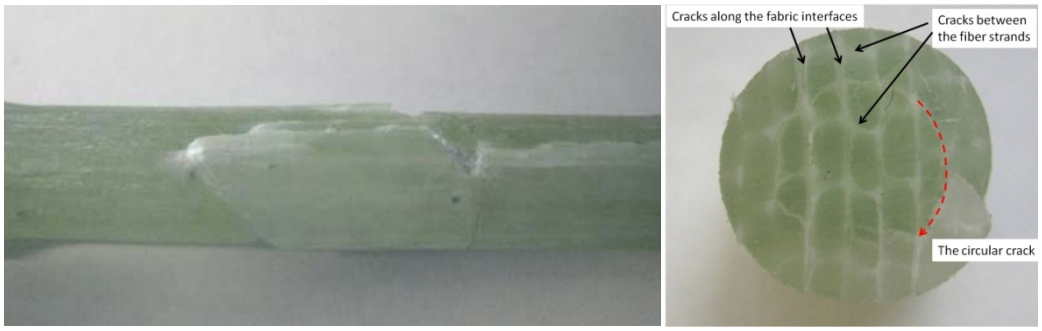

(b) (c)

Figure 48. Pictures of a failed B-type sample (#B1).

4.3.3 C-type samples

C-type samples showed similar behavior as A-type samples during testing, where a crack initiated from a single location on the spiral notch (Figure 49a) and propagated along the notch (Figure 49b). C-type samples also failed into two completely-separated halves (Figure 50a). However, a curvature was observed on the fracture surface (Figure 50b). In contrast, the fracture surfaces of A-type samples were flat (Figure 45).

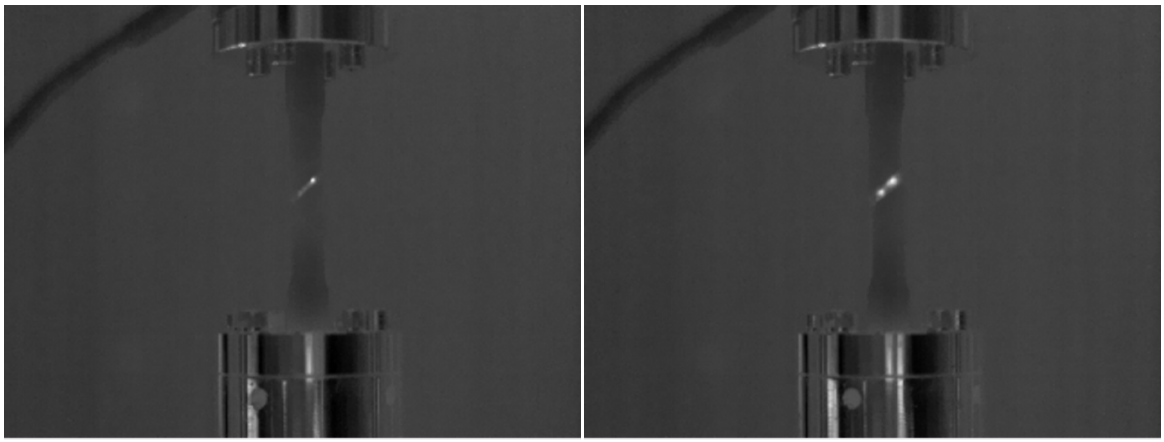

(a) (b)

Figure 49. IR images showing the loading of a C-type sample (#C-10) (a) when a crack initiated and (b) further propagated.

(a) (b)

Figure 50. Pictures of a failed C-type sample (#C-2).

4.4 Effect of fiber orientations

With a loading rate of 5 lbf-in per second, the representative torque-displacement curves of the SNTT experiments were shown in Figure 51 to Figure 53, showing that the failure torque was dependent on fiber orientations. In Figure 51, the failure torque of composite sample A was estimated as 35 lbf-in at peak failure torque. In Figure 52, the failure torque of composite sample B was estimated at the on-set of fracture about 70 lbf-in. In Figure 53, the failure torque of composite sample C was estimated to be 45 lbf-in. Similar load-deformation trends were also observed for SNTT experiments at other loading rates.

The reasons of the variation on the failure loads among different composite samples were the difference of the embedded lengths and orientations of the composite fibers. In composite sample A, the fiber orientations were orthogonal to the rotational axis. The interfaces between the fiber and the matrix were aligned with the fiber orientations. The maximum fiber lengths were the same length as the cylindrical diameter. Therefore, the composite sample A experienced a completely cut-through failure when cracks propagated along the interfaces between the fiber and matrix.

In composite sample B, the fiber orientations were parallel to the rotational axis of the cylinder. The maximum fiber length in the sample B was about the same length as that of the SNTT sample. When the composite sample B was loaded, cracks also propagated through the fiber-matrix interfaces. When the fiber and matrix were delaminated near the crack initiation sites, however, the anchored fibers located far away from the crack initiation sites still remained intact and could still sustain the fracture torque to the far field. Therefore, sample B's load-displacement curve revealed a horizontal plateau till significant plastic deformation reached. The disturbance along the plateau corresponded to the localized delamination in the composite sample B. The lengths and orientations of the fibers induced loading transfer mechanism ensured sample B to sustain a much higher failure load than sample A.

In composite sample C, the angle between the fiber orientations and the rotational axis was at 45° angle. The fiber-matrix interfaces were also along these orientations, while the fiber embedded lengths were $\sqrt{2}$ times longer than that of composite sample A. When the composite sample C failed, a cut-through surface also observed along the fiber-matrix interfaces. The failure loads of composite sample C was between those from sample A and sample B, which was also due to load transferring mechanism involved in the fiber orientations of composite sample C.

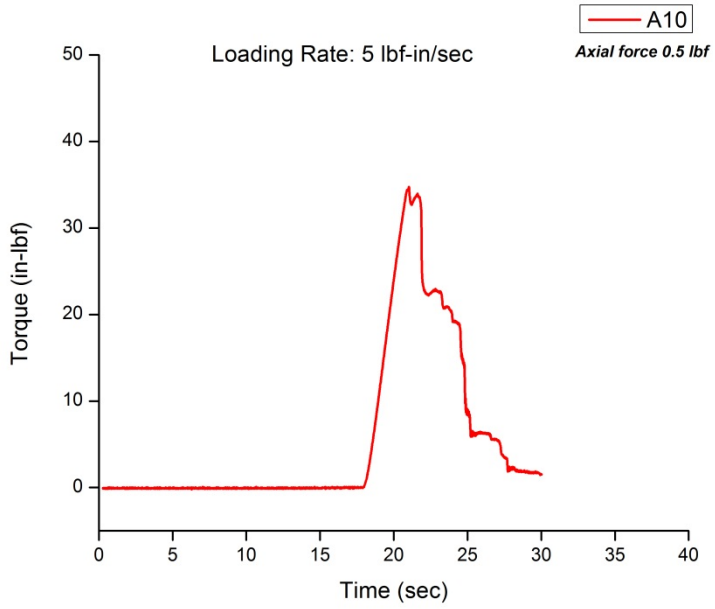

Figure 51. A representative load-displacement curve of composite SNTT sample A

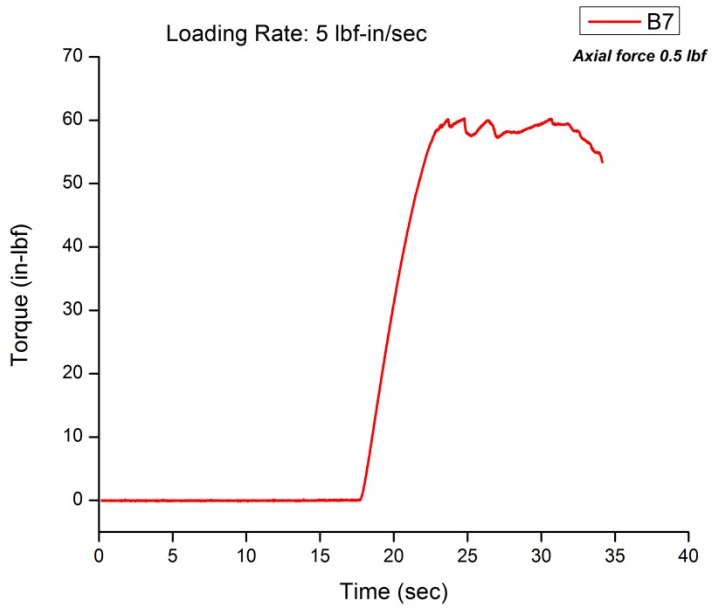

Figure 52. A representative load-displacement curve of composite SNTT sample B

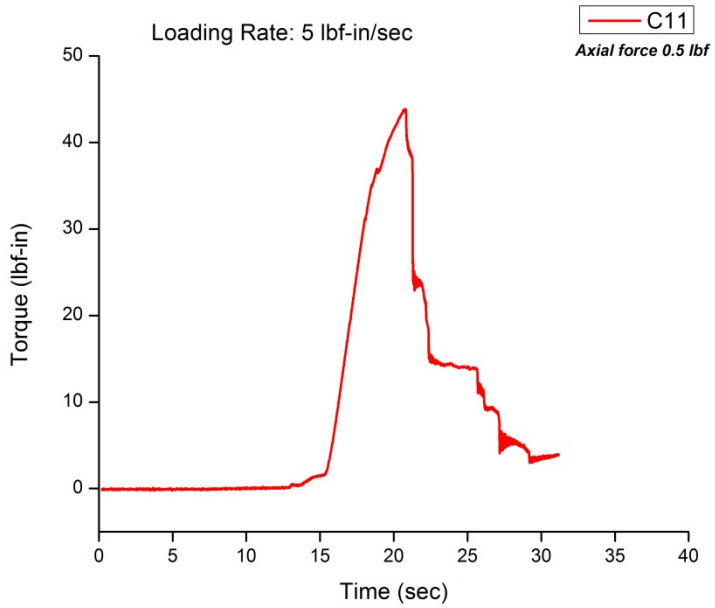

Figure 53. A representative load-displacement curve of composite SNTT sample C

4.5 Effect of loading rate

Three loading rates were selected for SNTT samples of each orientation. For each loading rate, three tests were repeated to perform statistics analysis. A summary of SNTT experimental results were shown in Figure 54. Under each loading rate, the failure load was the highest in the composite sample B and lowest in composite sample A. The failure load of the composite sample C was in between that of the composite sample A and the composite sample B. The rationale of the fiber orientation effects was discussed in the section 4.4.

For the loading rate effect investigation, two axial constraints were considered and applied to the SNTT experiments. For the loading rates of 5 lbf-in per second and 20 lbf-in per second, the axial compressive force was set as 0.5 lbf. For the loading rate of 10 lbf-in per second, the axial compressive force was set as 5 lbf. There was no significant difference in failure loads among selected loading rates for the same category of composite samples.

A few hints could still be obtained from the available results. For instance, for the same axial forces, the failure loads at the loading rate of 20 lbf-in per second were slightly higher than that with lower loading rate of 5 lbf-in per second. This seemed to be reasonable since higher loading rates reduced the time-dependent stress relaxation effect of the composites structure. More data were needed to further quantify this phenomenon. Furthermore, for the intermediate loading rate of 10 lbf-in per second with high compressive load of 5 lbf, it appeared to have similar failure toques level as that of higher loading rate data but with less axial compressive forces. This could be the increased localized constraint due to higher compressive stress in the intermediate loading rate data achieved the same effect of the higher loading rate data with smaller axial compressive stress.

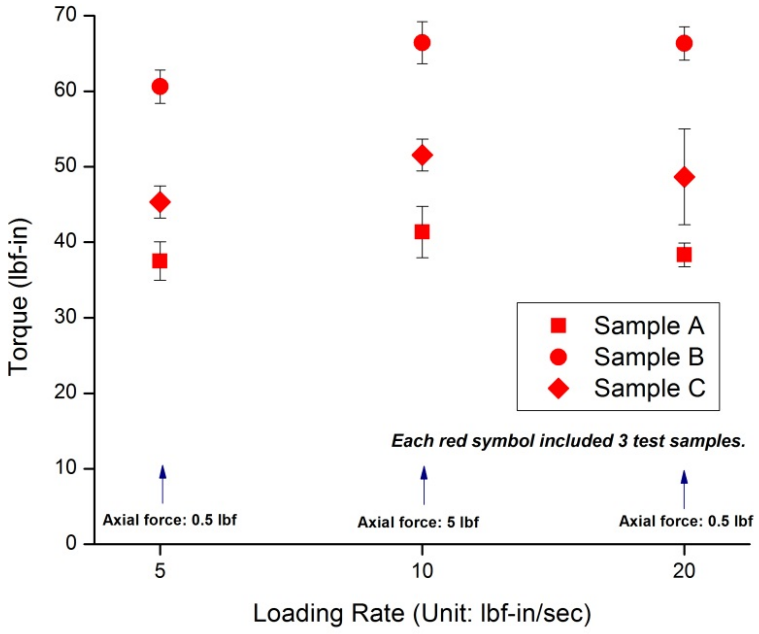

Figure 54. Experimental results of composite SNTT samples

4.6 Finite element analysis

4.6.1 Geometries

The geometries of the composite SNTT samples were shown in Figure 55. The diameter of the SNTT torsion bar was 0.39 inches with a notch angle at 45 degrees. The length of the numerical model was a quarter of the pitch length and the spiral rotated 90 degree on the projection in the cylindrical cross section.

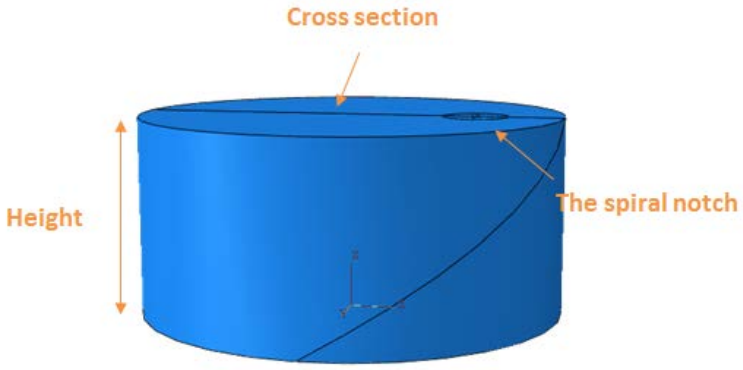

.

Figure 55. The geometry of the composite SNTT model

4.6.2 Meshing

The mesh of the composite SNTT sample followed the same rule as those in epoxy samples. Different element types were assigned to various areas. In order to capture local stress concentration, the element C3D15R in ABAQUS was assigned to the crack tip area. The element C3D20R in Abaqus was assigned to web areas around the crack tip circle area and the rest of the model. The mesh of the composite SNTT model was shown in Figure 56.

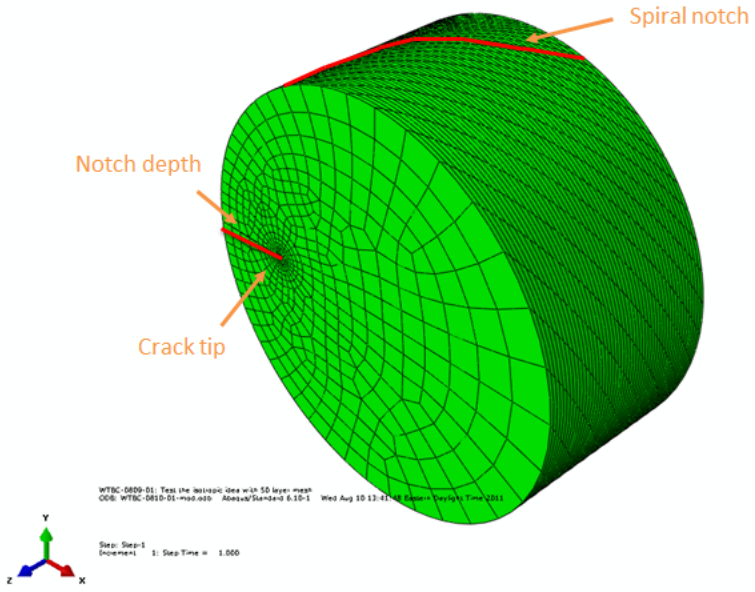

Figure 56. The finite element mesh of the composite SNTT sample

4.6.3 Materials

4.6.3.1 Orthotropic material

The SNTT samples used in this study were fabricated from fiber reinforced composite. The composite material was assigned to be orthotropic in the model. The constitutive relation of orthotropic material was given by:

$$\begin{Bmatrix} \varepsilon_{11} \\ \varepsilon_{22} \\ \varepsilon_{33} \\ \gamma_{12} \\ \gamma_{13} \\ \gamma_{23} \end{Bmatrix} = \begin{bmatrix} 1/E_1 & -\upsilon_{21}/E_2 & -\upsilon_{31}/E_3 & 0 & 0 & 0 \\ -\upsilon_{12}/E_1 & 1/E_2 & -\upsilon_{32}/E_3 & 0 & 0 & 0 \\ -\upsilon_{13}/E_1 & -\upsilon_{23}/E_2 & 1/E_3 & 0 & 0 & 0 \\ 0 & 0 & 0 & 1/G_{12} & 0 & 0 \\ 0 & 0 & 0 & 0 & 1/G_{13} & 0 \\ 0 & 0 & 0 & 0 & 0 & 1/G_{23} \end{bmatrix} \begin{Bmatrix} \sigma_{11} \\ \sigma_{22} \\ \sigma_{33} \\ \sigma_{12} \\ \sigma_{13} \\ \sigma_{23} \end{Bmatrix} \tag{5}$$

where E_1, E_2, E_3 are Young's moduli in the orientation 1, 2 and 3; G_{12}, G_{23}, G_{31} are the shear moduli associated; $\upsilon_{12}, \upsilon_{23}, \upsilon_{31}$ are Poisson's ratios. The terms $\upsilon_{21}, \upsilon_{32}, \upsilon_{13}$ are given by:

$$\upsilon_{21} = \frac{\upsilon_{12}}{E_1} E_2 \tag{6}$$

$$\upsilon_{32} = \frac{\upsilon_{23}}{E_2} E_3 \tag{7}$$

$$\upsilon_{13} = \frac{\upsilon_{31}}{E_3} E_1 \tag{8}$$

The composite mechanical properties [Agastra 2010] used in this study were summarized in Table 6.

Table 6. Orthotropic material properties used in the finite element model

E_1 (GPa)	41.80
E_2 (GPa)	7.38
E_3 (GPa)	14.00
G_{12} (GPa)	2.63
G_{12} (GPa)	2.63
G_{13} (GPa)	2.63
Density (kg/m³)	1924
ν_{12}	0.28
ν_{23}	0.28
ν_{31}	0.28

4.6.3.2 Fiber orientations

The SNTT composite samples were fabricated along different orientations with respect to the fibers. A system identification scheme was developed to assign the names of the fiber orientations within the composite, as shown in Figure 57. The stacking orientation was defined as the out-of-plane orientation orthogonal to the fibers. The fiber orientation was defined as the in-plane orientation parallel to the fibers; while the trans-fibers orientation was defined as the in-plane orientation orthogonal to the fiber orientation.

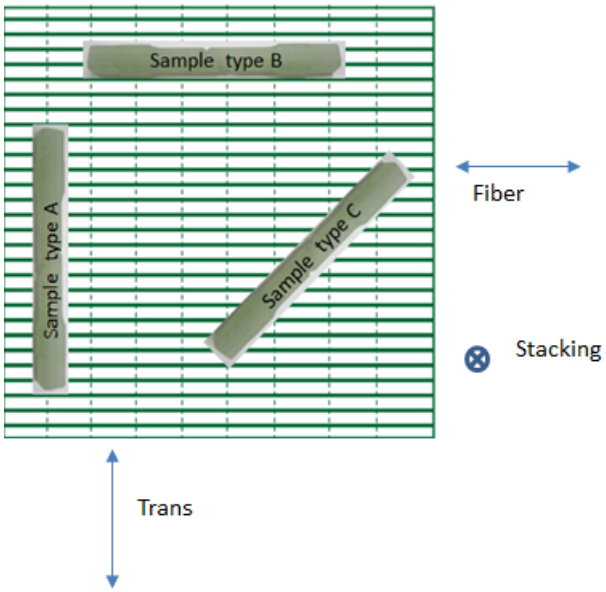

Figure 57.The name coordinate of the fiber-reinforced composite

Material models were created accordingly for composite SNTT samples A, B and C, respectively, as shown in Figure 58 to Figure 60. The orange arrow denoted the stacking orientation; the blue arrow denoted the fiber orientation; and the yellow arrow denoted the trans-fiber orientation. For composite sample A, Figure 58 showed that trans-fiber orientation is along with the axial orientation of the composite SNTT cylinder; while the fiber orientation was pointing out of the cylinder. This was consistent with the fiber orientations shown in Figure 57.

For composite sample B, Figure 59 shows that the fiber orientation was along the axial orientation of the SNTT cylinder; while the trans-fiber orientation and the stacking orientation was pointing out of the SNTT cylinder. For composite sample C, Figure 60 showed that the angle between the fiber orientation and the axial orientation of the SNTT cylinder was at 45°. The stacking orientation was pointing out of the SNTT cylinder. All the orientations were consistence with the sample fabricated, shown in Figure 57.

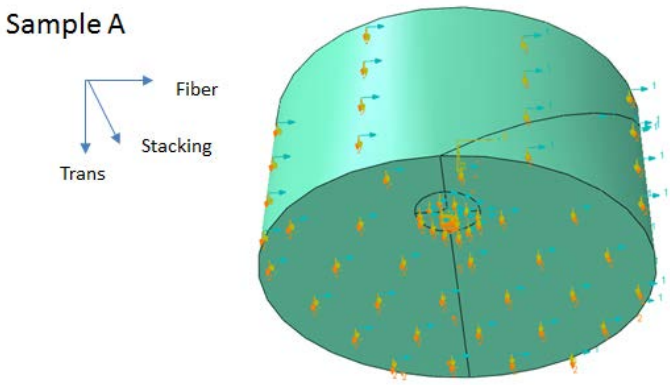

Figure 58. Matrial orientations of composite sample A

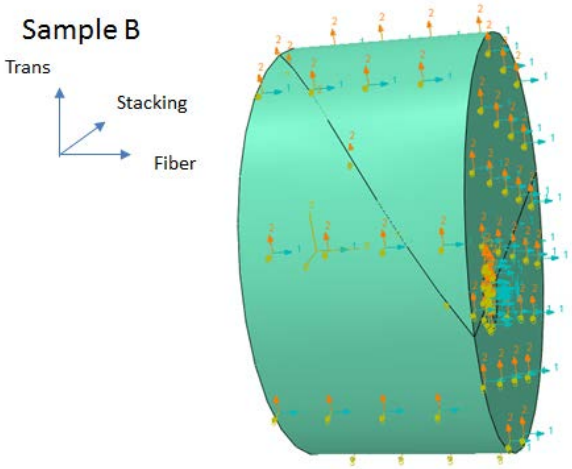

Figure 59. Matrial orientations of composite sample B

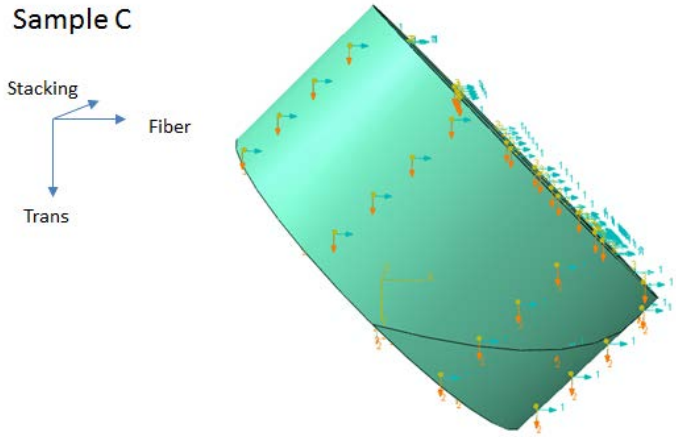

Figure 60. Matrial orientations of composite sample C

4.6.4 Loads and boundary conditions

The loading and boundary conditions were applied in the same way as those shown in Figure 17. A concentrated torque was applied at the center one surface. On the other surface, translations were fixed in the cross-section plane.

4.6.5 Results

4.6.5.1 Displacement distributions

A cylindrical coordinate system defined in Figure 18 was applied to show the displacement distributions of the composite SNTT samples. The displacement contour of the deformed composite SNTT sample B was shown in Figure 61 to Figure 63. Similar contours were also observed for displacement distributions of composite SNTT sample A and C. Compared with Figure 19 to Figure 21, the displacement contours in deformed composite SNTT sample B were closely resemble to those in deformed epoxy samples, which indicates the self-consistency of the SNTT experiments.

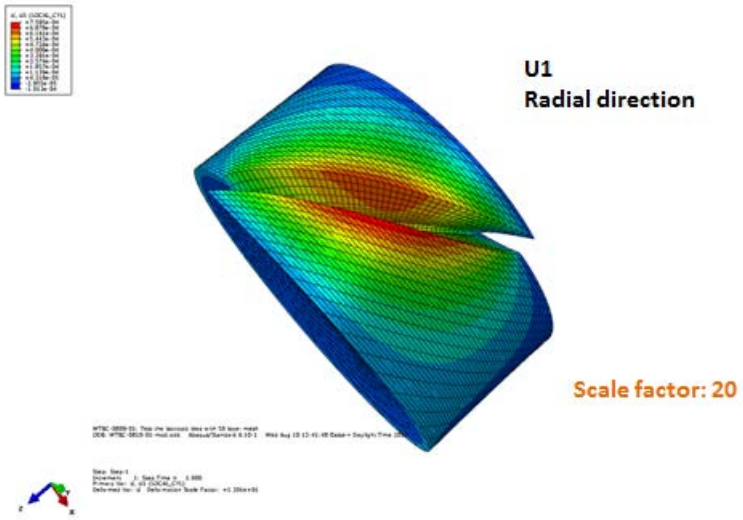

Figure 61. Radial displacement contours of the deformed composite SNTT sample

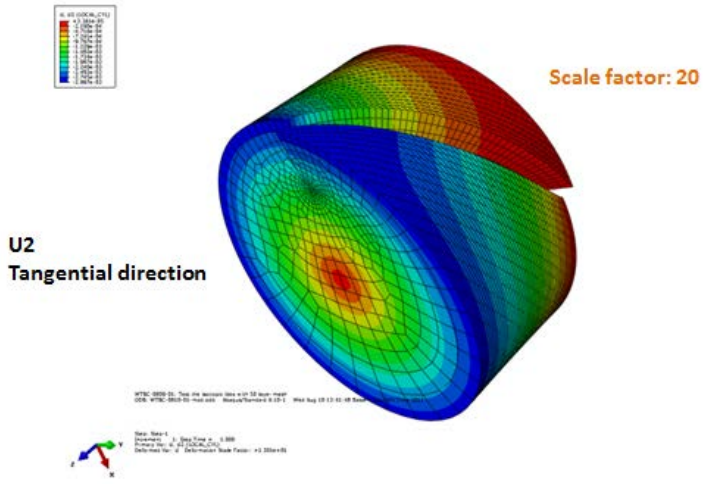

Figure 62. Tangential displacement contours of the deformed epoxy SNTT sample

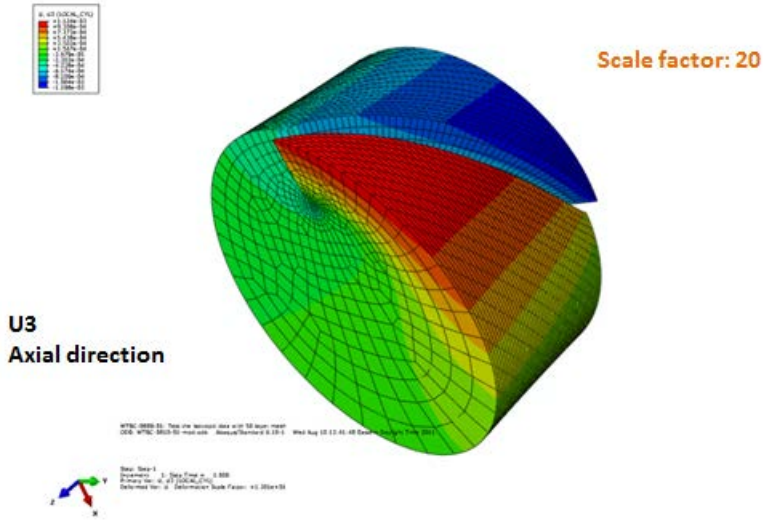

Figure 63. Axial displacement contours of the deformed epoxy SNTT sample

4.6.5.2 Von Mises stress distributions

The von Mises stress distributions of the deformed composite samples were shown in Figure 64 to Figure 69. The von Mises stress distributions of composite SNTT sample A were shown in Figure 64 and Figure 65. Figure 64 showed the stress concentration near the vicinity of the spiral crack front area. An element group was created to include all wedge elements around the crack tip in a single layer, and the von Mises stress distributions were shown for this element group in Figure 65. It showed that von Mises stress contours within the plastic process zone were not symmetric or self-similar. The root cause could be the fiber orientations within the composite SNTT sample. In composite sample A, the trans-fiber orientation was perpendicular to the axial

orientation of the SNTT cylinder. The fiber orientation and the stacking orientation were point out of the cylinder. The orthotropy of the composite induced the asymmetry of the von Mises stress distributions around the crack front area. Since the mechanical properties between the fiber orientation and the stacking orientation were very different, the asymmetry of the von Mises stress zone could be notably detected in Figure 65.

The von Mises stress distributions of composite SNTT sample B were shown in Figure 66 and Figure 67. Figure 66 showed the stress concentration near the vicinity of the spiral crack front area. Figure 67 illustrated von Mises stress distributions in the crack front area with higher scale. In sample B, the fiber orientation was parallel to the axial orientation of the SNTT cylinder. The trans-fiber orientation and the stacking orientation were two orthogonal orientations pointing out of the cylinder. Since the mechanical properties were similar between the trans-fiber orientation and the stacking orientation, the asymmetry of the plastic process zone around the crack tip was not as significant as that of sample A.

The von Mises stress distributions of composite SNTT sample C were shown in Figure 68 and Figure 69. The stress concentrations near the vicinity of the spiral crack front were shown in Figure 68. The von Mises stress distributions of the crack tip area with higher scale were shown Figure 69. Asymmetry of the plastic process zone was also observed for composite sample C, but different shape compared to that observed in sample A and sample B, due to fiber orientation effect.

In Figure 70, the von Mises stress distributions around the crack tip area for composite SNTT sample A, B and C were all scaled to composite sample B. It was shown that the von Mises stress distributions were highest in composite sample B; resulting in the highest energy release rates observed in sample B.

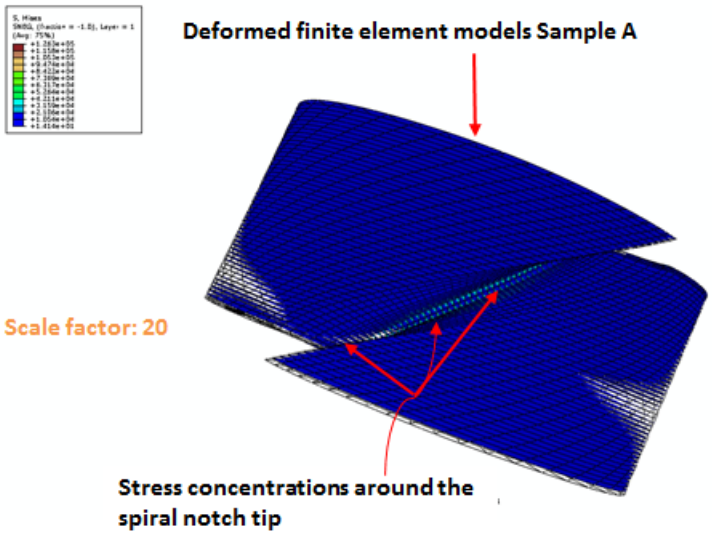

Figure 64. Von Mises stress distributions of composite SNTT sample A

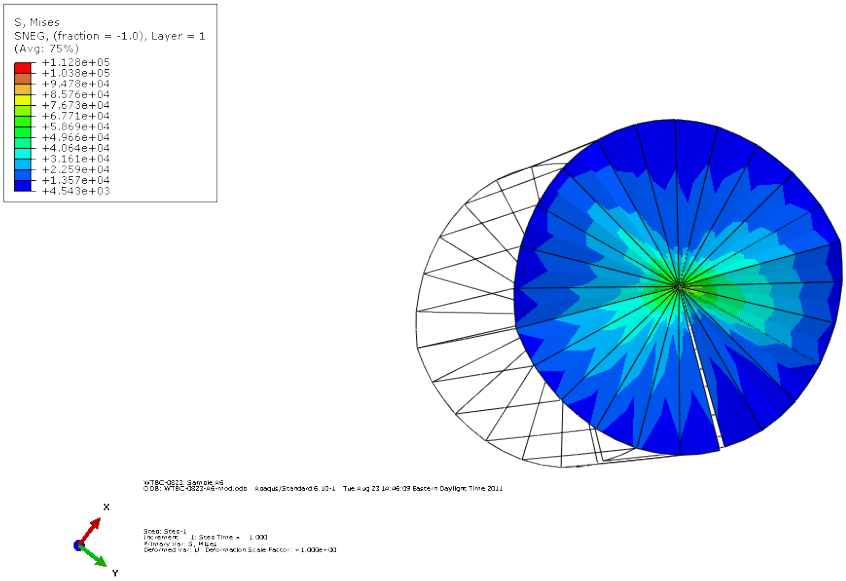

Figure 65. Mises stress distributions in the crack tip area of composite SNTT sample A

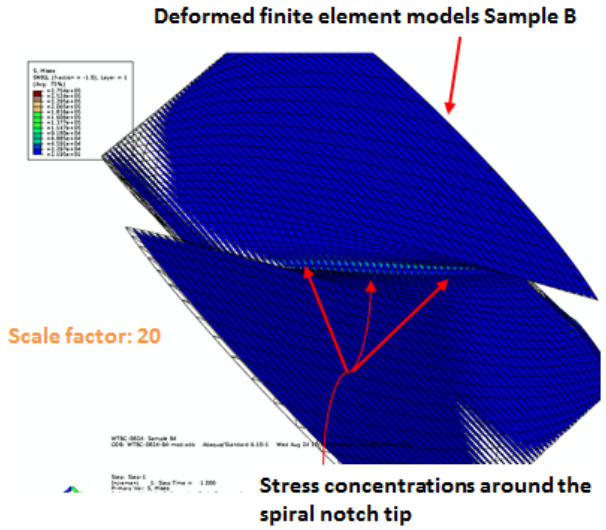

Figure 66. Mises stress distributions of composite SNTT sample B

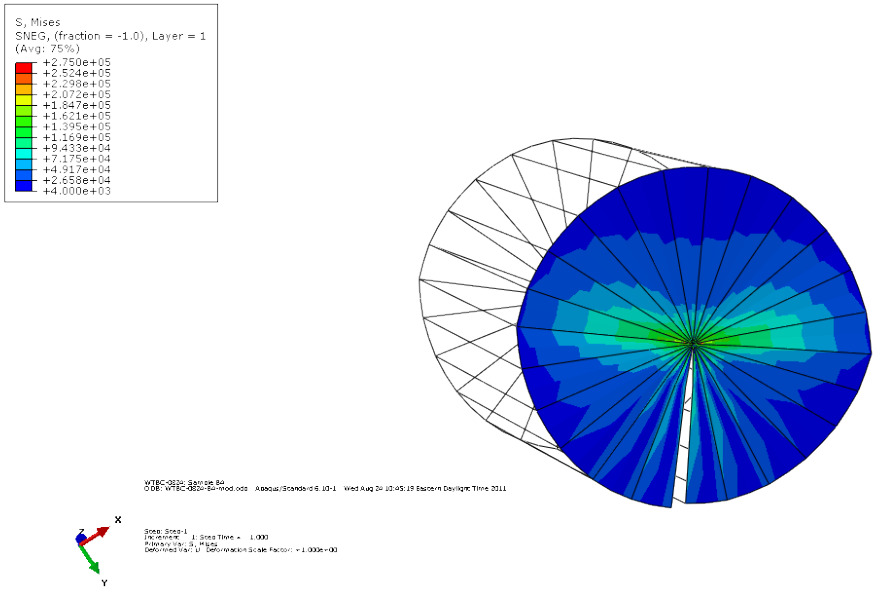

Figure 67. Mises stress distributions in the crack tip area of composite SNTT sample B

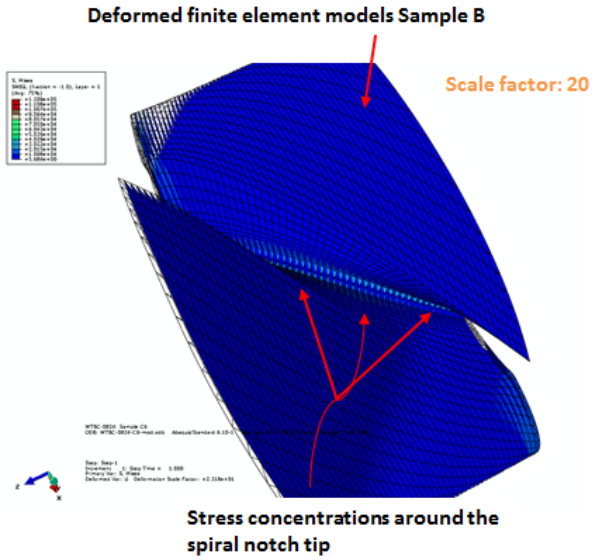

Figure 68. Mises stress distributions of composite SNTT sample C

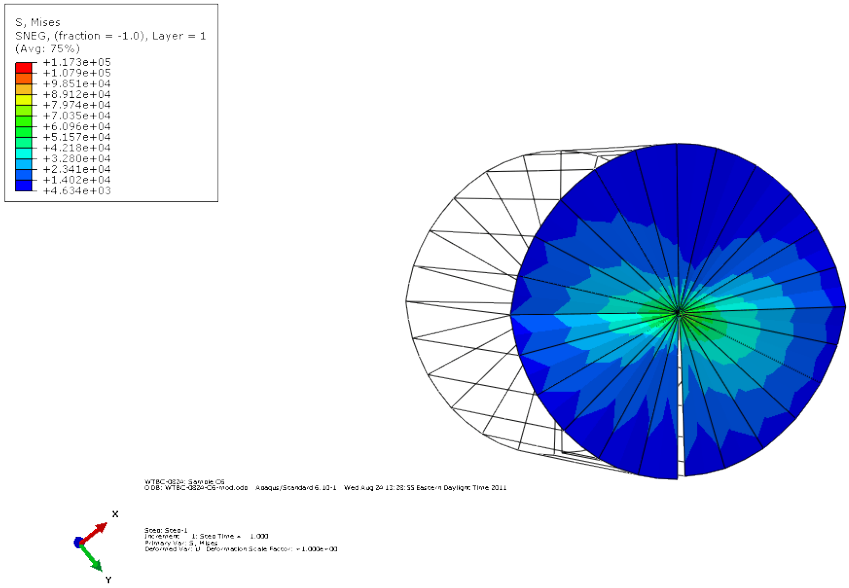

Figure 69. Mises stress distributions in the crack tip area of composite SNTT sample C

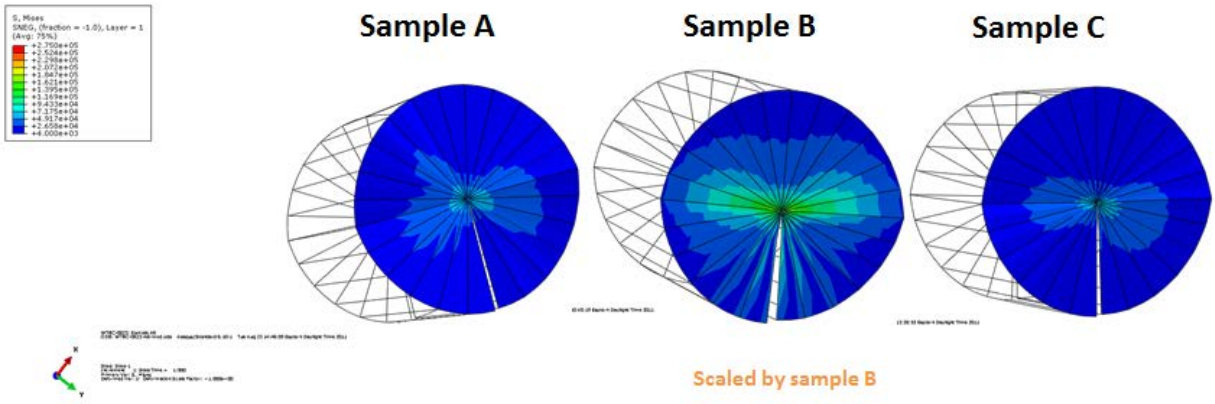

Figure 70. Scaled von Mises stress distributions of composite samples

4.6.5.3 Statistical analysis of composite SNTT experiment

Finite element analyses were performed to obtain the energy release rates associated with the experiment results presented in Figure 54. The distributions of the estimated energy release rates were shown in Figure 71 for various composite SNTT samples.

For each loading rate, the energy release rates of composite sample B were the highest; while the energy release rates of composite sample A were the lowest. The energy release rates of

composite sample C were in between those in sample A and sample B. For all composite samples, primary failures were caused by the interfacial delamination between the fibers and the matrix. But the energy release rates varied with the lengths and orientations of fibers in each type of composite sample.

For composite sample B, fibers were along the axial orientation of the SNTT cylinder, which provided effective (or sufficient long) anchor length across the spiral notch and within the SNTT samples. For composite sample A, the fiber orientations were orthogonal to the axial orientation of the SNTT cylinder and have the shortest continuing fiber lengths. Therefore, delamination failure occurred easily along the interface between the fibers and the matrix, resulting in the lowest energy release rates. For composite sample C, the angle between the fiber orientation and the axial orientation of the SNTT cylinder was at 45° angle. The continuing fiber length of composite sample C was between those of composite sample A and composite sample B. This caused an intermediate energy release rates of composite sample C compared to that of composite sample A and composite sample C. The variations of energy release rates among different composite samples could also be indicated by the von Mises stress distributions shown in Figure 70.

In general, the energy release rates of the same type of composite samples stayed at the same level or intensity for different loading rates. The energy release rates at the loading rate of 20 lbf-in per second appeared to be higher than that of loading rate at 5 lbf-in per second. Over the range of loading rates tested, the time-dependent effect was not significant to energy release rates of the SNTT composite samples. Nevertheless, a more thorough loading rate investigation with higher loading rate spectrum needed be considered to further quantify the loading rate effect of composite materials.

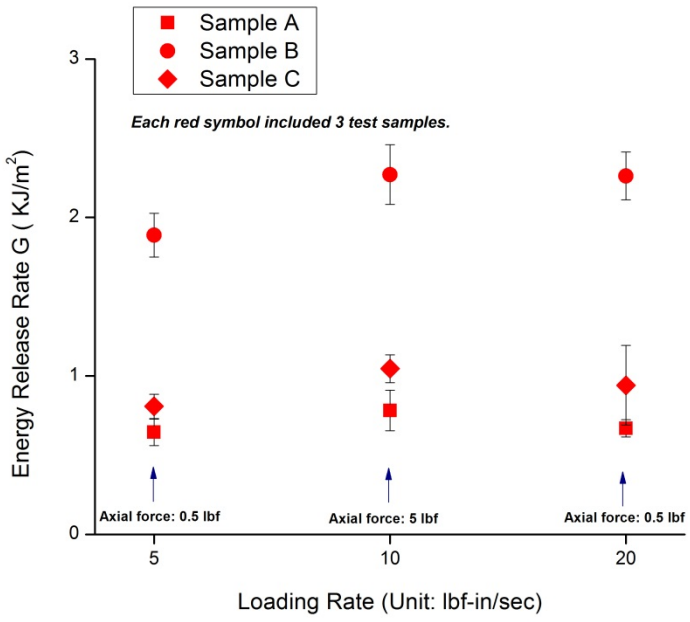

Figure 71. Energy release rates of composite SNTT samples

Table 7 Summary of energy release rate and stress intensity factors of composite SNTT samples.

Composites						
	G	KI	KII	KIII	a/D	Pitch
	kN/m	$MPa\sqrt{m}$	$MPa\sqrt{m}$	$MPa\sqrt{m}$		Degree
5 lbs-in/sec						
A2	0.65	2.61	0.22	0.00	0.21	45.00
A10	0.55	2.40	0.20	0.00	0.21	45.00
A11	0.72	2.75	0.23	0.00	0.21	45.00
B7	1.76	4.72	-0.20	1.43	0.21	45.00
B8	1.87	4.86	-0.21	1.47	0.21	45.00
B9	2.03	5.07	-0.22	1.53	0.21	45.00
C1	0.77	2.61	0.25	0.50	0.21	45.00
C9	0.90	2.81	0.27	0.54	0.21	45.00
C11	0.75	2.58	0.25	0.49	0.21	45.00
10 lbs-in/sec						
A3	0.89	3.05	0.26	0.01	0.21	45.00
A4	0.66	2.64	0.23	0.00	0.21	45.00
A5	0.90	3.06	0.26	0.01	0.21	45.00
A6	0.68	2.67	0.22	0.00	0.21	45.00
B1	2.40	5.51	-0.24	1.67	0.21	45.00
B2	2.05	5.10	-0.22	1.54	0.21	45.00
B3	2.35	5.46	-0.24	1.65	0.21	45.00
C2	0.99	2.95	0.29	0.57	0.21	45.00
C3	1.02	2.99	0.29	0.57	0.21	45.00
C4	1.00	2.96	0.29	0.57	0.21	45.00
C5	1.18	3.22	0.31	0.06	0.21	45.00
20 lbs-in/sec						
A7	0.61	2.53	0.21	0.00	0.21	45.00
A8	0.67	2.65	0.22	0.00	0.21	45.00
A9	0.72	2.74	0.23	-0.02	0.21	45.00
B4	2.23	5.31	-0.23	1.60	0.21	45.00
B5	2.13	5.19	-0.22	1.43	0.21	45.00
B6	2.43	5.54	-0.24	1.67	0.21	45.00
C6	0.79	2.64	0.26	0.51	0.21	45.00
C7	1.23	3.29	0.32	0.63	0.21	45.00
C8	0.80	2.65	0.26	0.29	0.21	45.00

5. Future work

It has been demonstrated that fiber/resin interfacial debonding and resin matrix cracking are two major failure modes in the polymeric composite materials investigated in this study. Using SNTT technique, the fracture behavior of neat epoxy resins were studied in detail in the first stage of this project. In the second stage, the performance of the composites was examined from a macroscopic approach, where the fiber/resin composites were considered orthotropic.

This macroscopic approach can be readily implemented in evaluating industrial wind turbine components. By testing surveillance samples obtained from various locations of turbine blades, a database can be compiled while the fracture toughness can be mapped. These results will provide useful information to industrial manufactures to help the evaluation, design, and improvement of wind turbine blades. In addition, wind turbines are designed to serve 20 or more years, during which turbine components are subject to frequent sub-critical loading. Thus, fatigue testing of composite samples will also be beneficial to the wind industry.

On the other hand, in order to predict the microscopic fracture behavior of these composite materials, detailed models are necessary, which requires the knowledge of the response of the interfacial regions under both Mode I and mixed-mode loading conditions. Interfacial fracture has been a very difficult task to resolve, partially due to the uncontrollable crack propagation. Due to its unique geometry, SNTT configuration imposes large constraints on the samples. Moreover, the testing results obtained on the epoxy samples demonstrated that crack propagation can be well controlled. Thus, the SNTT technique could provide valuable merits to the interfacial fracture testing.

As discussed in Sections 4.1.3 and 4.1.4, artificial interfaces between resin and reinforcement fibers can be created using the infusion technique. Combining advanced monitoring methods (e.g. acoustic emission) and finite element analysis, the fracture events at the interfaces could be accurately monitored and modeled. As mentioned above, these results will provide necessary information to detailed understanding of interfacial fracture phenomena. In addition, the successful experience can be further extended to investigating the integrity of the adhesive bonding, which is heavily used in industrial manufacturing of large wind turbines.

Another future direction would be conducting SNTT testing in simulated environments, such as offshore conditions. One of the advantages of SNTT is its reduced sample size. While many traditional fracture mechanics tool relies on large samples to obtain accurate fracture toughness results, SNTT can utilize much smaller sample sizes due to its intrinsic geometrical constraint. Thus, it is more practical to build environmental testing facilities around SNTT testing machine than many other methods. And experimental testing in simulated conditions will provide important and irreplaceable data for wind energy industry.

6. Summary

In this study, the spiral notch torsion test (SNTT) has been utilized to investigate the fracture behavior of polymeric composites and epoxy resins used for manufacturing wind turbine blades.

Three epoxy materials received from two industrial partners (Gougeon Brothers and Molded Fiber Glass Companies) were used to fabricate SNTT samples with various notch depths and pitch angles. Fractures with and without fatigue precracks were studied.

All epoxy samples tested exhibited linear elastic behavior until fracture, which is consistent with the brittleness characteristic of these materials. During fracture tests, both Mode I (pitch angle = 45^o) and some mixed-mode (pitch angle $\neq 45^o$) samples tended to fracture along a spiral plane that has a 45^o pitch angle with respect to the sample axis, indicating that Mode I fracture dominated in these brittle materials.

Under cyclic fatigue loading different fatigue process zones were observed on Mode I and mixed-mode samples. On Mode I samples, a uniform extended fatigue zone was formed due to fatigue crack growth, which then grew into a uniform band of mirror region. In contrast, a semi-elliptical fatigue zone was discovered on mixed-mode samples subject to fatigue. A transition region was found between the semi-elliptical fatigue zone and the mirror region. It was likely that during the fatigue process cracks grew in the mixed mode. When tested after cyclic fatigue, the crack changed from mixed-mode growth to Mode I growth, leaving a transition region beyond the fatigue zone. The smooth mirror region was the evidence that the crack propagated in a Mode I manner during the proceeding fracture loading.

Finite element analysis indicated the energy release rate of some mixed-mode samples was higher than those of Mode I samples; while samples of mixed-mode fracture along the mixed-mode fracture contour appear to have much lower toughness that that of mixed-mode samples fracture along 45° pitch fracture plane. The fatigue precrack samples had much lower energy release rates compared to that of samples without fatigue precrack, due to sharper crack front. Samples failed during the fatigue precrack process had much lower energy release rates compared to that of SNTT test results, due to significantly higher loading rates, ~ 2 orders of magnitude, than that of typical SNTT testing.

Shallow notch depth, where the majority of epoxy SNTT samples had initial notch depth to sample diameter ratio around 0.1, and insufficient precision control on the notch root sharpness, could result in less constraint boundary conditions in the vicinity of the crack front. This may result in a relative higher energy release rate and fracture toughness compared to that of SNTT sample with sharper notch root and higher a/D ratio. As regarding the mixed-mode study, the above mentioned constraint issues can also affect the mixed-mode failure investigation, such as

fracture contour aligns with mixed-mode contour or climbs back to 45° principal stress plane. Therefore, more investigation on epoxy fracture behaviors will be performed in the future on refined SNTT samples with sharper crack fronts and relatively deeper crack penetration length to reaching higher a/D ratios. By doing so we can further increase the SNTT sample geometry constraint to increase the accuracy of obtaining intrinsic fracture toughness of these materials.

The successful SNTT testing protocols were further extended to study composite materials. In order to fabricate suitable composite samples for SNTT testing, different approaches were trialed. The attempt to make resin/composite/resin sandwich structures failed because a large empty space was left after infusion and the fabrics were only partially saturated. Thus, an alternative approach was utilized such that thick composite plates were prepared, from which SNTT samples were cut and machined. Three types of composite samples were obtained. The angle between the sample axis and the fiber orientations were 90^o for A-type, 0^o for B-type, and 45^o for C-type samples.

During SNTT testing, A-type and C-type samples exhibited similar behavior. The cracks tended to initiate at single locations along the notch root and then extended to the entire notch length. The fracture plane propagated through the samples, completely separating A-type and C-types samples into halves. However, the fracture surfaces of A-type were flat; while a curvature was observed on the fracture surfaces of C-type samples.

In contrast, B-type samples were held as a whole by glass fibers after failure. Post mortem examination showed a very complex crack pattern on the cross section of B-type samples. Three crack systems were observed: 1) cracks along the fabric interfaces; 2) cracks between the fiber strands; and 3) a circular crack approximately corresponded to the projection of the spiral notch on the cross-section plane.

Finite element models were used in this study to evaluate the energy release rates of the composite SNTT samples with different fiber orientations. The composite materials were assumed to be orthotropic. The energy release rates were the highest for B-type composite samples and the lowest in A-type composite samples. It was also found that the energy release rates of composite samples were not significantly affected by the tested loading rates. The testing results demonstrated that the embedded lengths and orientation of fibers were important to the failure loads and energy release rates of the composite samples.

In addition to the composite samples machined from the bulk plates, two additional types of samples were fabricated: 1) fiber strands embedded in the groove of epoxy SNTT samples, and 2) epoxy resin embedded in the groove of composite samples. These pilot experiments demonstrated infusion could be a promising technique to fabricate interfacial samples for SNTT testing, which is an important direction in future studies.

Other areas of interests to investigate in the future include testing of samples obtained from industrial wind turbines, testing under cyclic loadings, and testing under simulated offshore conditions. Furthermore, our industrial partner, Molded Fiber Glasses Companies agreed to provide composite materials from their existing decommissioned wind turbine blades in the near future. Such aged wind turbine blade composite materials are extremely useful in benchmarking current available aging models or developing new prediction models for estimating the effective lifetime of wind turbine blade composites during service. These proposed future works will significantly improve our understanding of the fracture behavior of wind composite materials and provide precious data and guidelines for the development of the wind energy industry.

References

[Abaqus 2010] Abaqus software manual (2010), Simulia, Dassault Systèmes.

[Agastra 2010] Agastra, P. and J.F. Mandell, "Testing and simulation of damage growth at ply drops in wind turbine blade laminates," in Proceedings of SAMPE 2010, paper # 398, Seattle, 2010.

[ASTM C1322] ASTM C1322, Standard Practice for Fractography and Characterization of Fracture Origins in Advanced Ceramics, ASTM International, West Conshohocken, PA, USA, 2005.

[Brondsted 2005] P. Brondsted, H. Lilholt, A. Lystrup, Annual Review of Materials Research, 35 (2005) 505-538.

[Hayman 2008] Hayman, B., J. Wedel-Heinen and P. Brondsted (2008). "Materials challenges in present and future wind energy." *Mrs Bulletin* **33**(4): 343-353.

[Hull 1999] D. Hull, Fractography: observing, measuring, and interpreting fracture surface topography, Cambridge University Press, Cambridge, UK, 1999.

[Kensche 2006] Kensche, C. W. (2006). "Fatigue of composites for wind turbines." *International Journal of Fatigue* **28**(10): 1363-1374.

[Owen 1975] Owen, M. J. and R. G. Rose (1975). "FRACTOGRAPHY OF POLYESTER RESINS." *Journal of Materials Science* **10**(10): 1711-1718.

[Sanford 2003] R.J. Sanford, Principles of fracture mechanics, Pearson Education, Inc., Upper Saddle River, NJ, 2003.

[Sih 1974] Sih, G. C., "Strain Energy Density Factor Applied to Mixed Mode Crack Problem," *International Journal of Fracture*, 1974, Vol. 10, pp. 305-321.

[Wang 2000] Wang, J. A., K. C. Liu, D. E. McCabe and S. A. David (2000). "Using torsional bar testing to determine fracture toughness." *Fatigue & Fracture of Engineering Materials & Structures* **23**(11): 917-927.

[Wang 2002a] Wang, J.-A. and K. C. Liu (2002). ORNL Spiral-Notch Torsion Test (SNTT) System. *2002 R&D 100 Award*, R&D Magazine.

[Wang 2002b] J. A. Wang, K. C. Liu, and D. E. McCabe, "An Innovative Technique for Measuring Fracture Toughness of Metallic and Ceramic Materials," *Fatigue and Fracture Mechanics: 33rd Volume*, ASTM STP 1417, W. G. Reuter and R. S. Piascik, Eds., pp. 757-770, December 2002

[Wang 2010] John Jy-An Wang and Fei Ren, "An Innovative Technique for Evaluating the Integrity and Durability of Wind Turbine Blade Composites", ORNL Report ORNL/TM-2010/191, Oak Ridge National Laboratory, 2010.

APPENDIX A: DOE Wind Turbine Blade Integrity Project - FY2010 Progress Report

ORNL/TM-2010/191

Materials and Technology Division
Oak Ridge National Laboratory

An Innovative Technique for Evaluating the Integrity and Durability of Wind Turbine Blade Composites

FY2010 Report

Jy-An John Wang and Fei Ren

Date Published: September 2010

Prepared by
OAK RIDGE NATIONAL LABORATORY
Oak Ridge, Tennessee 37831-6283
Managed by
UT-BATTELLE, LLC

For the
U.S. DEPARTMENT OF ENERGY
under contract DE-AC05-00OR22725

ACKNOWLEDGEMENTS

This research was sponsored by the Wind Energy Program of Department of Energy and was carried out at Oak Ridge National Laboratory under contract DE-AC05-00OR22725 with UT-Battelle, LLC. The authors are grateful to Mr. Stanton Hadley and Dr. Brennan Smith supporting this project.

The epoxy materials included in this study were provided by Gougeon Brothers, Inc. and Molded Fiber Glass Companies (MFG). The authors would like to thank Mr. Williams Bertelsen at Gougeon Brothers, Inc. and Mr. Carl LaFrance at Molded Fiber Glass Companies for their support and helpful discussions.

The authors would like to thank Dr. Hsin Wang and Mr. Charles Chan of ORNL for their assistance and helpful discussions regarding the infrared imaging, and Dr. Dan Naus and Dr. James Hemrick of ORNL for their comments and suggestions after reviewing this report.

Table of Contents

LIST OF FIGURES

LIST OF TABLES

EXECUTIVE SUMMARY

Wind turbine blades are subjected to complex multiaxial stress states during operation. A review of the literature suggests that mixed mode fracture toughness can be significantly less than that of the tensile opening mode (Mode I), implying that fracture failure can occur at a much lower load capacity if the structure is subject to mixed-mode loading. Thus, it will be necessary to identify the mechanisms that might lead to failure in blade materials under mixed-mode loading conditions.

Meanwhile, wind turbine blades are typically fabricated from fiber reinforced polymeric materials, e.g. fiber glass composites. Due to the large degree of anisotropy in mechanical properties that is usually associated with laminates, the fracture behavior of these composite materials is likely to be strongly dependent on the loading conditions. This may further strengthen the need to study the effect of mixed-mode loading on the integrity and durability of the wind turbine blade composites.

To quantify the fracture behavior of composite structures under mixed mode loading conditions, particularly under combined Mode I (flexural or normal tensile stress) and Mode III (torsional shear stress) loading, a new testing technique is proposed based on the spiral notch torsion test (SNTT). As a 2002 R&D 100 Award winner, SNTT has been recognized as a novel fracture testing technology which should be suitable for analyzing the expected loading behaviors. SNTT has many advantages over conventional fracture toughness methods and has been used to determine fracture toughness values on a wide spectrum of materials. The current project is the first attempt to utilize SNTT on polymeric and polymer-based composite materials. It is expected that mixed-mode failure mechanisms of wind turbine blades induced by typical in-service loading conditions, such as delamination, matrix cracking, fiber pull-out and fracture, can be effectively and economically investigated by using this methodology.

This project consists of two phases. The Phase I (FY2010) effort includes (1) preparation of testing material and testing equipment set-up, including calibration of associated instruments/sensors, (2) development of design protocols for the proposed SNTT samples for both polymer and composite materials, such as sample geometries and fabrication techniques, (3) manufacture of SNTT samples, and (4) fracture toughness testing using the SNTT method. The major milestone achieved in Phase I is the understanding of fracture behaviors of polymeric matrix materials from testing numerous epoxy SNTT samples.

A total of 30 epoxy SNTT samples were fabricated from two types of epoxy materials provided by industrial partners Gougeon Brothers, Inc. and Molded Fiber Glass Companies. These samples were tested with SNTT in three groups: (1) fracture due to monotonic loading, (2) fracture due to fatigue cyclic loading, and (3) monotonic loading applied to fatigue-precracked samples.

Brittle fractures were observed on all tested samples, implying linear elastic fracture mechanics analysis can be effectively used to estimate the fracture toughness of these materials with confidence. Appropriate fatigue precracking protocols were established to achieve controllable crack growth using the SNTT approach under pure torsion loading. These fatigue protocols provided significant insight in to the mechanical behavior of epoxy polymeric materials and their associated rate-dependent characteristics. Study of the effects of mixed-mode loading on the fracture behavior of epoxy materials found that all epoxy samples failed in brittle tensile failure mode; the fracture surfaces always follow a 45^o spiral plane that corresponded to Mode I tensile failure, even when the initial pitch angle of the machined spiral grooves was not at 45^o. In addition, general observation from the fatigue experiments implied that loading rate played an important role determining the fracture behavior of epoxy materials, such that a higher loading rate resulted in a shorter fatigue life. A detailed study of loading rate effect will be performed in Phase II of the project.

Fracture toughness evaluation by analytical finite element analysis is also an integral part of the research program. In the report period this analysis was also initiated with preliminary progress resulting in the building of geometric models and designs with appropriate meshing protocols for epoxy polymeric samples.

Based on the experience learned from the Phase I study, in FY2011 we will carry out Phase II efforts to continue the finite element analysis to simulate the fracture process of both epoxy and composite materials. Experimental investigation will be focused on blade composite materials and the proposed SNTT composite samples will be jointly developed by the ORNL team and Prof. John Mandell’s group at Montana State University.

1. Introduction and background

Improvement of wind turbine performance depends upon enhancing the reliability of turbines and components. To increase the energy capture capability, future designs will utilize larger rotors with longer blades fabricated with advanced composite materials with high strength and stiffness-to-weight ratios [Hayman 2008]. This will require more thorough knowledge of materials and safety factors, as well as further investigation into new materials. In particular, the basic understanding of damage and failure mechanisms, the effects and interpretation of stochastic loadings, multiple stress states, environmental effects, size effects, and thickness effects shall be obtained [Kensche 2004].

1.1 Mixed mode loading of wind turbine blades

During operation wind turbine blades are subjected to complex multiaxial stress states. To ensure that the next generation of wind power systems operate safely and reliably it will be necessary to identify the mechanisms that might lead to failure in blade materials and to fully characterize their behavior under extreme conditions. This may further strengthen the need to study the mixed-mode loading effect on the integrity and durability of the wind turbine blade composites.

Fracture is one of the most dramatic failure modes of any engineering structure. A material's intrinsic capacity to resist fracture is known as ***fracture toughness***. Although there are an extensive number of studies on fracture toughness under tensile loading (Mode I fracture), little information is available for fracture toughness under mixed loading conditions that involves sliding (Mode II) and/or tearing (Mode III). As mentioned previously, wind turbines are unfortunately subject to mixed mode loading. Literature data indicates that mixed mode (Mode I + Mode III) fracture toughness and dynamic tearing modulus values are reduced by 50% and 70%, respectively from those under Mode I conditions [Li 1996].

1.2 Mixed loading of polymeric composites

Typical composite materials used in wind turbine blade manufactures are fiber (glass and/or carbon fibers) reinforced polymeric (especially thermosetting polymers) materials. Compared to fibers, the polymeric matrices possess a much lower stiffness. The toughness and especially failure strain is moderate for thermosets, 5–8%, and the polymeric matrices thus induce toughness in the composites, in particular via energy absorbing mechanisms related to the fiber-matrix interface [Kelly 2000]. Thus, the mixed-mode failure mechanism of the resin matrix deserves attention.

Because the composite materials used for the manufacture of these components are laminated, fracture behavior of the interfacial region between layers in the lamina and between fibers and the polymeric matrix, tend to be the weakest elements in the

composite. Therefore, this needs to be characterized to ensure the structural reliability of the composites. The availability of simplified test methods to characterize the fracture behavior of composite materials under mixed modes of fracture is essential to enable the qualification and use of these materials for the next generation of wind turbines.

1.3 Spiral notch torsion test (SNTT)

1.3.1 SNTT approach and FEM analyses

To quantify the fracture behavior of composites under combined Mode I (flexural tensile stress) and Mode III (torsion shear stress) loading, this project aims to develop novel methods to test polymeric composite materials, based on the spiral notch torsion test (SNTT), an ORNL patented [Wang 2003a] R&D 100 Award winning technology [Wang 2002a].

The SNTT test method uses a round-rod specimen having a V-grooved spiral line at a 45° pitch (Figure 1), subjected to pure torsion. When the grooved specimen is sectioned into segments perpendicular to the groove line, each of the segments can be viewed as a CT specimen with a notch. Since all the imaginary CT specimens are bonded side-by-side seamlessly, the compatibility condition is automatically satisfied, and remains in place before and after application of torsion loading. In the absence of the V-groove, the stress state of a generic element in a round bar under pure torsion can be depicted as tension (normal to the 45° pitch) and compression (tangential to 45° pitch) of equal magnitude. When a notch is introduced (Figure 1), a tri-axial tensile stress field will evolve in the neighborhood of the notch root area. This observation has been experimentally and analytically validated [Wang 2000, 2002b]. Therefore, when a V-grooved spiral line with a 45° pitch is machined on the surface of the specimen, the grooved line effectively becomes a Mode I crack mouth opening.

Due to the 3-D non-coplanar crack front of the SNTT configuration and the lack of closed form solutions, K_{IC} of the SNTT method was evaluated using 3-D finite element analysis and derived from minimum strain energy density criterion [Sih 1974] or J-Integral based on the domain integral method [Wang 2000, 2002b]. Typically, a finite element model shown in Figure 2a is used for brittle SNTT specimens, such as concrete, with shallow crack fronts and while the model shown in Figure 2b is used for ductile specimens. The SNTT FEM model normally contains about 8,000 20-node quadratic brick elements with reduced integration and 35,000 nodes.

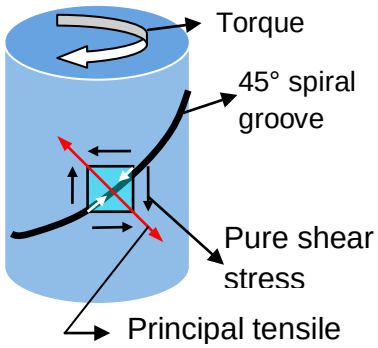

Figure 1. SNTT configuration.

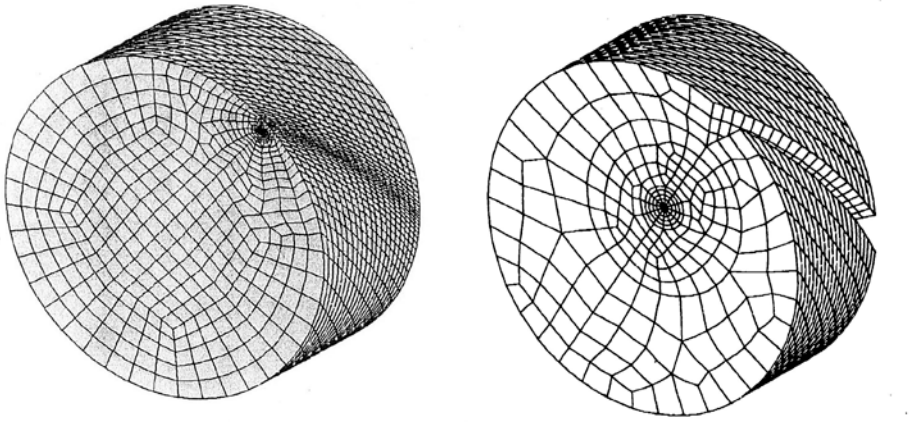

(a) Shallow notch crack (b) Deep fatigue precrack

Figure 2. SNTT FEM Models.

1.3.2 SNTT specimen size reduction

The CT specimen, as shown in Figure 3, has been widely used in existing fracture toughness test methods because the general consensus indicates it is the next-best basic configuration that nearly conforms to the strict requirements of the classical theory of fracture mechanics. Despite the simplification, the theoretical conditions (i.e., the conditions required to achieve uniformly distributed applied stress over the thickness and plane-strain condition) can never materialize as long as free surfaces exist at both ends of the specimen. The end effects will be further amplified when the thickness decreases to a thin plate, as shown in Figure 3. Another dilemma is that an increase in specimen thickness will automatically accompany an increase in specimen length and width in order to maintain specimen rigidity under load. Miniaturization is an important

goal of the SNTT method. This is made possible because the K_{IC} values determined by the SNTT method are virtually independent of specimen size. A cursory review of the stress and strain fields in a CT specimen indicates that the key information needed for determining the K_{IC} values is manifested within a small region near the crack tip; therefore, the rod specimen can be miniaturized substantially without the loss of general validity (Figure 3). The purpose of the vast volume of the material outside the critical zone in conventional samples is to poise the ideal far field of stress and to provide a means to accommodate loading devices. This redundancy is eliminated to the optimum condition in the round rod specimen; therefore, specimen miniaturization is achievable.

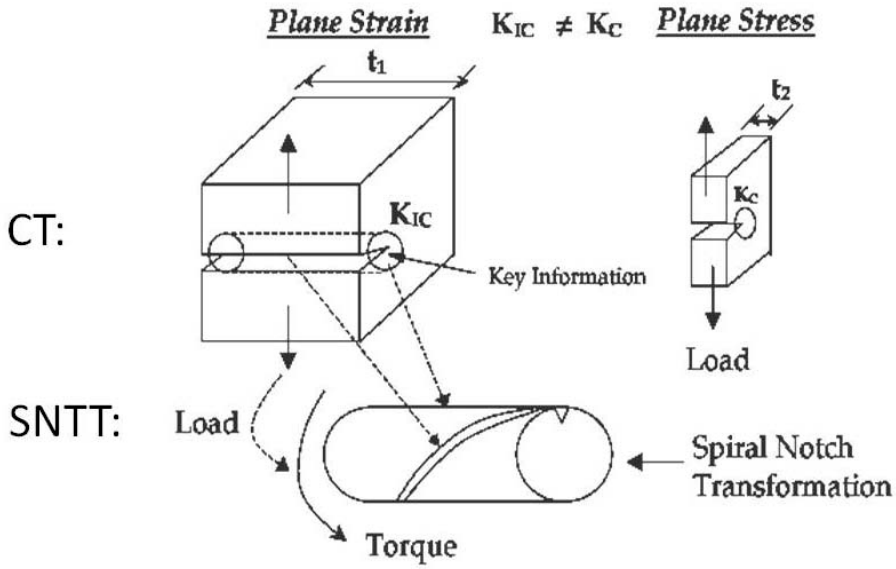

Figure 3. Specimen size effect.

Figure 4 illustrates the fracture toughness testing methods for brittle materials (such as graphite or carbon composite), which indicates that a test specimen machined with a deep notch is required. However, for the SNTT method only a shallow surface notch is required for testing of brittle materials. This will further reduce the specimen size as compared to a conventional test as shown in Figure 4.

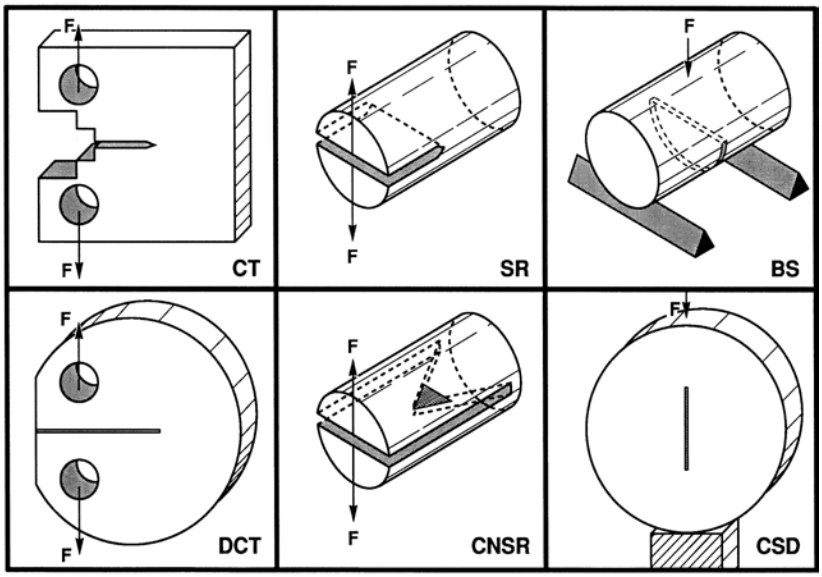

CT: Compact Tension; SR: Short Rod; BS: Bending Short Rod; DCT: Disk shape CT; CNSR: Chevron Notched Short Rod; CSD: Central loaded Short Disk.

Figure 4. Brittle material toughness testing methods.

Because of the plane strain and axisymmetric constraint and the uniformity in the stress and strain fields of the SNTT configuration, the crack front must propagate perpendicularly toward the specimen axis and along the conoids. Post-mortem examination verified such crack propagation behavior (see Figure 5) which was also verified from epoxy fatigue precracked samples.

Figure 5. SNTT sample made from aluminum 7475-T7351

1.3.3 Mixed-mode fracture toughness

In a recent study of mixed-mode fracture [Li 1996], utilizing a complex test set-up with a specially machined CT specimen, test results indicate that mixed-mode (Mode I + Mode III) toughness and tearing modulus reduced to 50% and 30%, respectively, compared to those under Mode I only for the ductile materials. Therefore, the implication or the potential of the synergistic impact due to the combination of flexural normal stress (Mode I fracture) and the torsion shear stress (Mode III fracture) to the fracture toughness for the composite materials needs a close look. As for the brittle materials, the Mode I is still the dominate failure mode, such as for epoxy materials, as revealed from the current study on the epoxy materials. In applying the SNTT approach for the mixed Mode I + Mode III failure study, this can be achieved by simply varying the pitch angle of the spiral notch. A radiator hose was used to illustrate the SNTT approach under pure torsion loading Figure 6. As shown in Figure 6a, a slit was cut along the principal shear direction, i.e., along 0 or 180°, and the deformation appears to be pure shear Mode III failure. As shown in Figure 6b if a slit was cut along 45° angle, along the principal tensile stress orientation, the deformation appears to be opening Mode I failure. Therefore, by varying the pitch angle, Mode I and Mode III loading can be achieved with a SNTT sample under pure torsion loading.

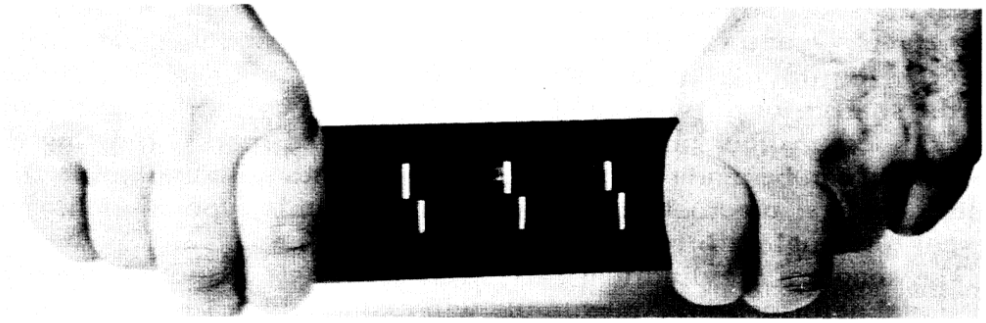

(a)

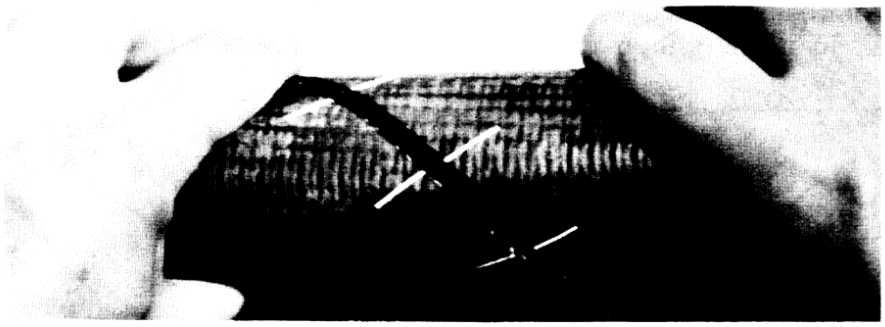

(b)

Figure 6. Illustration of SNTT approach using a radiator hose.

2. Scope of current research

The objective of this research is to develop a mixed-mode SNTT methodology for evaluation of mixed-mode, static and dynamic fracture behaviors of composite materials used for wind turbine blades. The project is divided into the following steps:

1) Equipment and sample preparation;
2) SNTT testing and simulation of matrix polymeric materials;
3) SNTT testing and simulation of composite materials;
4) Study on the effects of loading rates and environmental factors

During FY2010 progress has been made in preparing the testing equipment, sample design and fabrication, testing of epoxy materials, and finite element modeling of epoxy SNTT samples. Specifically, the effects of sample geometry and loading conditions (Mode I vs. mixed mode) have been extensively studied. A great effort has also been put into characterization of the fracture surfaces of the test epoxy samples.

The first year accomplishment demonstrated the applicability of the SNTT technique for the evaluation of polymeric materials and provided understanding of the fracture behavior of these materials under tensile loading and mixed mode loading.

The encouraging results to date led to further exploration into the composite regime. The ORNL research team is currently working closely with Prof. John Mandell's group at Montana State University on designing and fabricating composite samples for SNTT experiments.

3. Equipment and sample preparation

3.1 Equipment preparation

In this study, a biaxial (axial/torsional) hydraulic-servo testing machine (Model 809, MTS Systems Corp. Eden Prairie, MN, USA) is used to conduct the SNTT testing (Figure 7). The maximum load and torque of this test machine are 22,000 lbf and 10,000 lbf-in, respectively. During the first quarter of 2010, the loading frame was realigned, the filters for the hydraulic pump were replaced, and a hydraulic lock seal was replaced. A pair of sample grip fixtures were also designed and fabricated. Figure 7 shows the SNTT test set-up with an epoxy sample being tested under pure torsion loading.

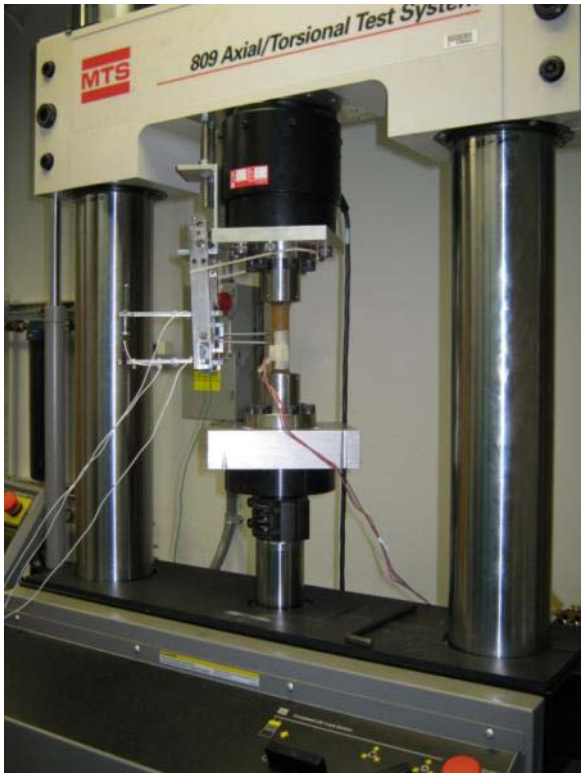

Figure 7. MTS 809 Axial/torsional test system used for SNTT.

An in-house built biaxial extensometer was utilized for displacement measurements (Figure 7). The extensometer consists of three pairs of capacitive sensors used to measure the relative displacement of the two probe pins both in the axial direction and torsional directions. Prior to testing, the extensometer was calibrated with a biaxial extensometer calibration block (Figure 8).

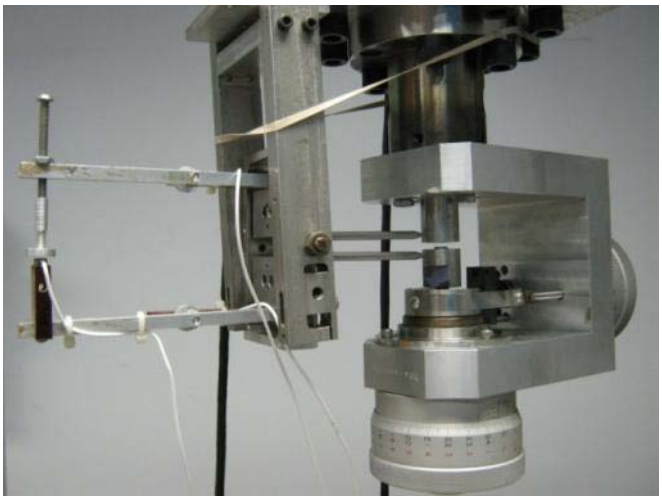

Figure 8. Calibration of the biaxial extensometer.

The data acquisition system consists of three capacitive amplifiers (Model 4100-L, Capacitec Inc. Ayer, MA, USA) and a clock drive with LED meter (Model 4100-CM4, Capacitec Inc. Ayer, MA, USA), all enclosed by a rack enclosure (Model 4016-C, Capacitec Inc. Ayer, MA, USA). The Capacitec system is connected to a computer by coaxial cables for data recording (Figure 9).

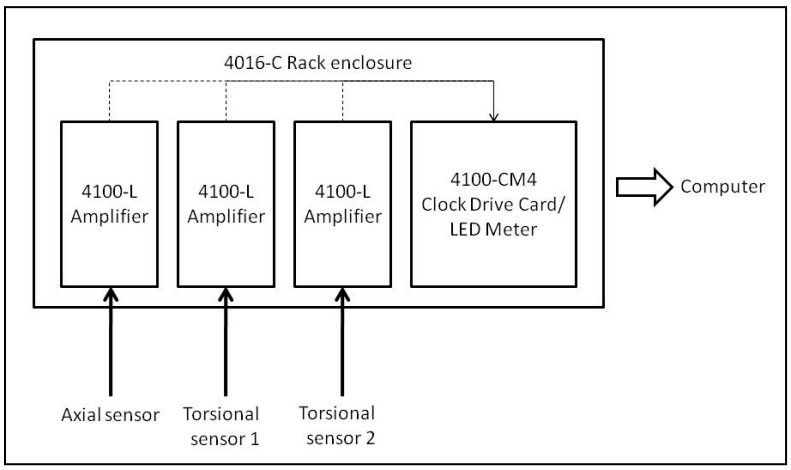

Figure 9. Block diagram of the capacitive data acquisition system.

In order to monitor and record the in-situ temperature on the sample surface during SNTT testing, an infrared imaging system (Model A325, FLIR Systems, Boston, MA, USA) has been set up (Figure 10). In addition, thin film thermocouples (CO1-K, Omega Engineering, Inc. Stamford, CT, USA) are also used as a temperature reference.

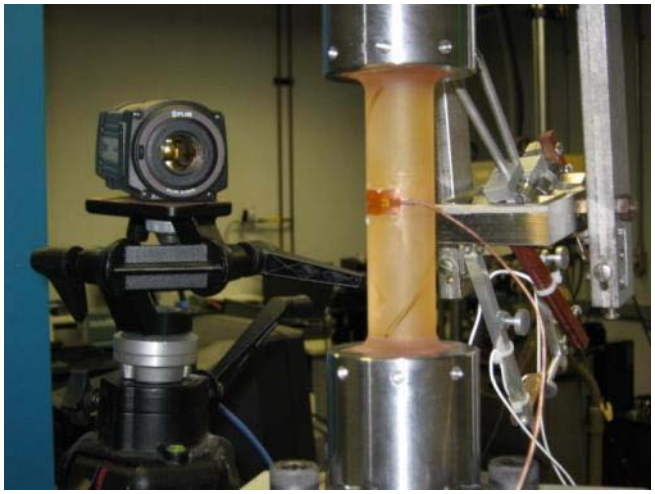

Figure 10. The IR imaging system used to monitor SNTT samples.

3.2 Epoxy sample preparation

Raw epoxy materials were obtained from two of our industrial partners: Pro-Set® epoxy, Gougeon Brothers (GB), Inc. Bay City, MI; and Hexion® EpikoteTM MGS® epoxy, Molded Fiber Glass Companies (MFG), Ashtabula, OH (Table 1) (Figure 11). Basic mechanical properties, as provided by the vendors are summarized in Table 1and the chemical compositions for each epoxy system are listed in Table 2.

Table 1. Processing and mechanical properties of the received epoxy materials

Mechanical properties	117LV/229	117LV/XH10B	RIM135/RIMH1366
Supplier	GB	GB	MFG
Product family	Pro-Set®	Pro-Set®	Hexion® Epikote^{TM} MGS®
Resin to hardener ratio	100:31	100:33.9	100:30
Curing conditions	Overnight at room temperature followed by 8 hrs at 60^{o}C		Cured through the exotherm, and post-cured for 6.5 hours at 70^{o}C.
Elastic modulus (GPa)	3.4	3.1	2.7-3.2
Tensile strength (MPa)	70	66	60-75
Tensile elongation (%)	3.2	4.3	8-16
Compressive strength (MPa)	102	104	80-90
Impact strength	28.3 J/m	57.6 J/m	70-80 KJ/m^{2}

Table 2. Chemical composition of the resins and hardeners used in the study.

Epoxy component	**Ingredient**	**concentration**
Pro-Set® 117LV infusion resin	Bisphenol-A type epoxy resin	
	Bisphenol-F type epoxy resin	
	Neopentyl glycol diglycidyl ether	< 25%
PRO-SET® 229 Hardener	Polyoxypropylenediamine	25-50%
	Reaction products of isophoronediamine with phenol/formaldehyde	< 25%
	Isophoronediamine	< 25%
	Triethylenetetramine (TETA)	<12%
	Hydroxybenzene	<7%
Developmental Hardener XH 00-099-10B	Polyoxypropylenediamine	25-50%
	Reaction products of isophoronediamine with phenol/formaldehyde	<25%
	Isophoronediamine	< 25%
	Triethylenetetramine (TETA)	<10%
	Hydroxybenzene	<7%
EPIKOTE™ Resin MGS RIMR 135	4,4'-Isopropylidenediphenol-Epichlorohydrin Copolymer	70-100%
	1,6-Hexanediol Diglycidyl Ether	10-30%
EPIKURE™ Curing Agent MGS RIMH 1366	Alkyletheramine	25-50%
	Isophoronediamine	20-25%
	Aminoethylpiperazine	<20%

(a) (b)

Figure 11. Pictures showing raw epoxy materials received from (a) Gougeon Brothers, Inc. and (b) Molded Fiber Glass Companies.

The geometry of the epoxy samples for SNTT testing is illustrated in Figure 12. The samples are 1” in diameter with a gauge length of 4”and a V-shaped spiral groove machined on the sample surface. Most samples have a V-groove with $\psi = 45^{o}$ angle, while a few samples were made with $\psi = 90^{o}$.Three depths of groove were used: 0.1”, 0.2”, and 0.3” to simulate different crack lengths. The pitch angle θ, varies between 45^{o}

and 20°. When $\theta = 45^{o}$, the principal stress σ_1 (tensile) is perpendicular to the notch, and the associated failure mode will be Mode I (tensile opening mode). When $\theta < 45^{o}$, the notch is subject to a mixed loading of Mode I and Mode III (tearing mode, torsional shear mode). Figure 13 shows some pictures of SNTT epoxy samples. To date (by August. 24th 2010), a total number of 31 epoxy samples were fabricated (Table 3).

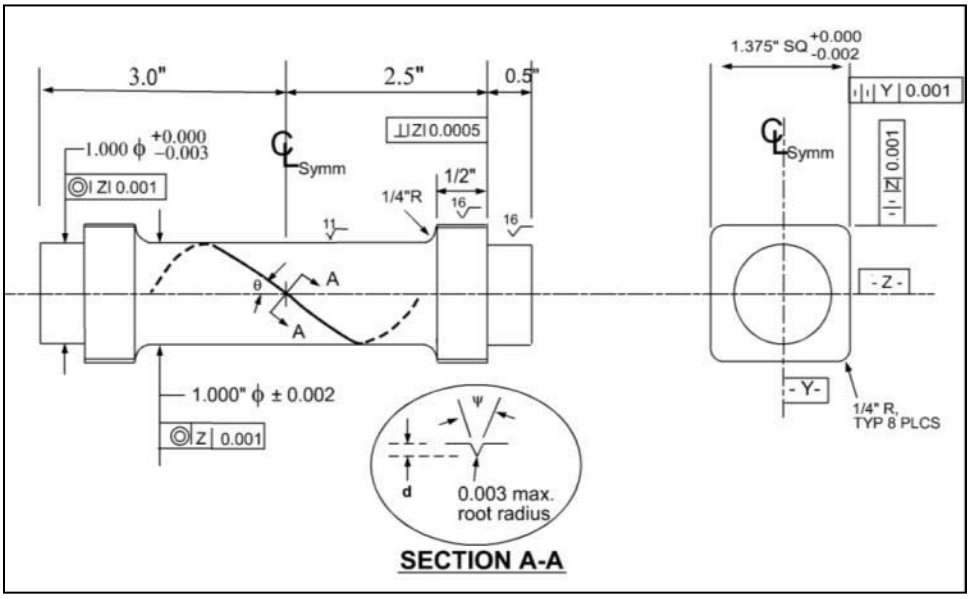

Figure 12. SNTT sample geometry.

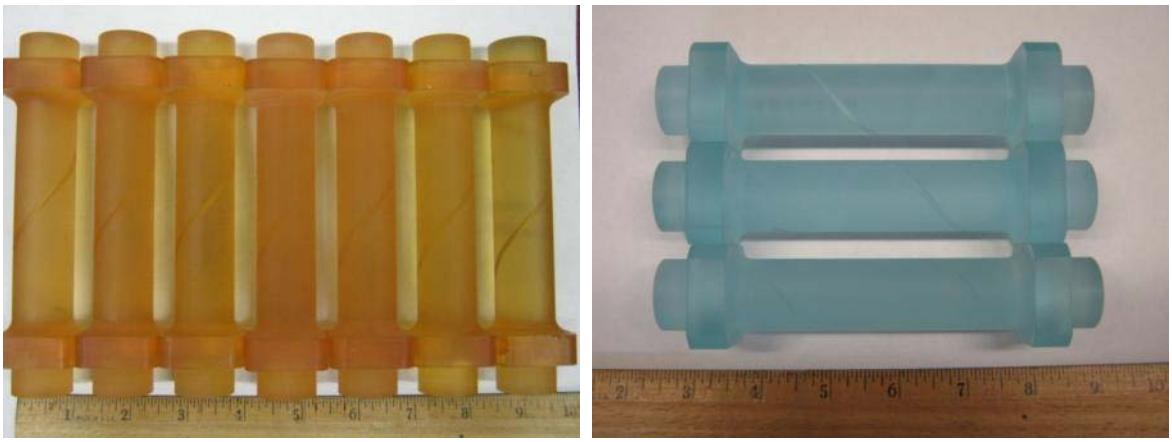

(a) (b)

Figure 13. Pictures showing machined samples made from epoxy materials provided by (a) Gougeon Brothers, Inc. and (b) Molded Fiber Glass Companies.

Table 3. Geometries of SNTT epoxy samples.

Depth		Pitch angle	Sample ID
d = 0.1”	$\psi = 45^o$	$\theta = 45^o$	GB 3-4, 3-5, 3-6, 3-7
			GB 4-4, 4-5, 4-6
			MFG 1, 2, 3
		$\theta = 36^o$	GB 1-1, GB 1-2, GB 1-3, GB 1-4, GB 1-5, GB 1-6, GB 1-7
			GB 2-1, GB 2-2
d = 0.115”	$\psi = 90^o$	$\theta = 45^o$	GB 3-1, 3-2, 3-3
			GB 4-1, 4-2, 4-3
d = 0.2”	$\psi = 45^o$	$\theta = 28^o$	GB 2-3, GB 2-4
		$\theta = 45^o$	GB 3-8
d = 0.3”	$\psi = 45^o$	$\theta = 20^o$	GB 2-5, GB 2-6
		$\theta = 45^o$	GB 3-9

Note on sample ID: GB = Gougeon Brothers, Inc., MFG = Molded Fiber Glass Companies, the first number denotes the batch number; the second number denotes the sample number in a given batch.

3.3 Composite sample design

To date, more than 30 epoxy samples have been successfully fabricated through machining based on the geometry shown in Figure 12. However, making composite samples presents many challenges. One of the challenges is related to the anisotropic nature of composite materials used in turbine blades, such as fiber glass composites. Epoxies can be treated as isotropic materials. In contrast, reinforcement fibers not only possess different mechanical properties, such as higher stiffness, but also exhibit large anisotropy such that the properties in the axial direction can vary significantly from transverse direction. In addition, the composites may exhibit increased toughness when fiber is added.

Thus, different approaches are proposed to fabricate composite samples. One approach is to build composite structures on top of epoxy bars, by either filling in a machined groove with epoxy/fiber (Figure 14a) or gluing fiber layers on to the epoxy surface (Figure 14b). In these configurations, the epoxy bar functions as a mandrel. In a different approach sandwich structures will first be made from epoxy and fiberglass layers, followed by core-drilling to form cylindrical samples (Figure 14 c-d). Depending on the relative orientation of the sample axis after core-drilling of the original sandwich structure, a spiral notch may (Figure 14c) or may not (Figure 14d) be needed.

Further improvements in sample design and composite sample fabrication are in progress as a joint effort between the ORNL team and the MSU group.

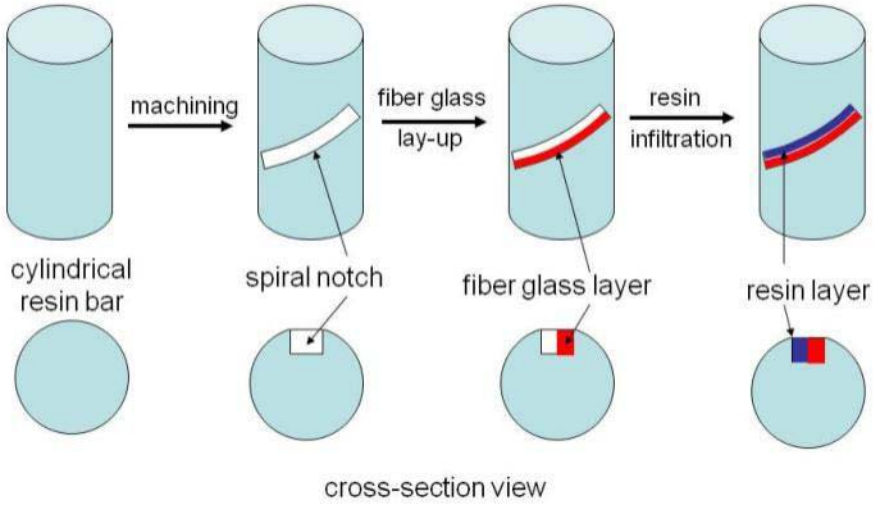
machining
fiber glass
lay-up
resin
infiltration
cylindrical
resin bar
spiral notch
fiber glass layer
resin layer
cross-section view

(a)

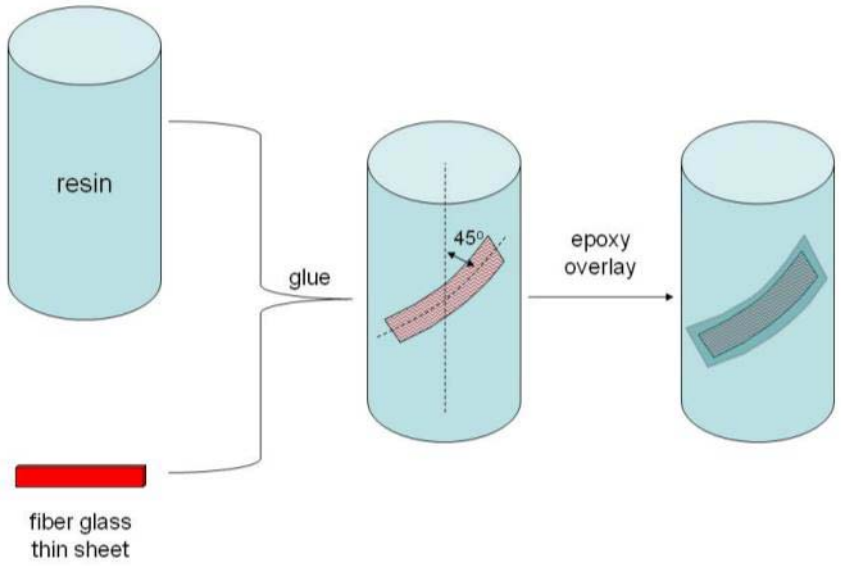
resin
glue
45°
epoxy
overlay
fiber glass
thin sheet

(b)

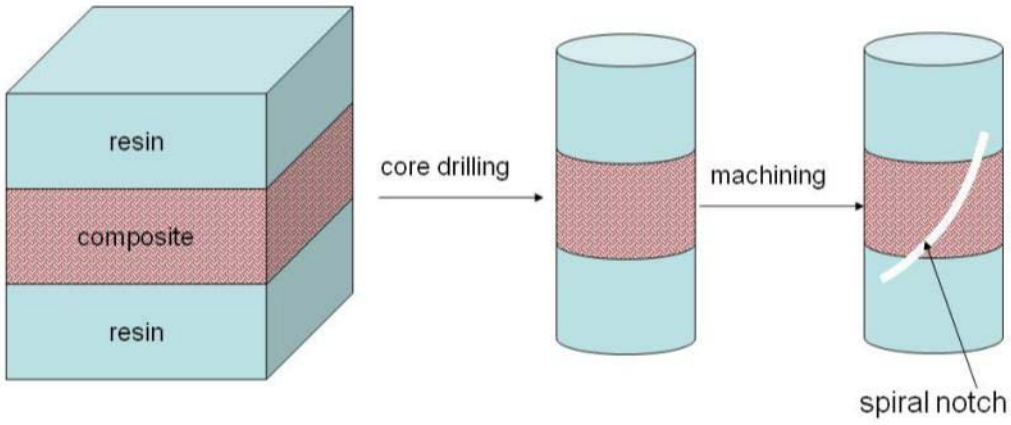

(c)

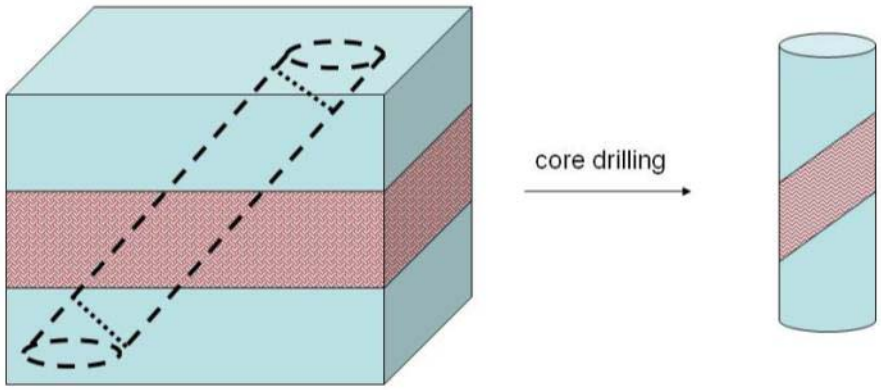

(d)

Figure 14. Proposed methods for fabricating composite SNTT samples.

4. SNTT testing of epoxy samples

Three types of torsional testing were performed on epoxy samples:

1) *Monotonic loading*;
2) *Fatigue*;
3) *Monotonic loading* of fatigued samples;

For monotonic loading, pure torsion loading was applied to the samples with axial loading maintained as close to zero as possible. For a SNTT sample, the tensile principal stress is normal to the groove line with a 45° pitch angle. Torque was monotonically increased until the sample fractured at a constant loading rate of 40 lbf-in/sec. Meanwhile, a small compression force of 5 lbf was maintained along the sample axis to prevent the sample from dropping off the grips.

For fatigue testing, various loading conditions have been explored. Two controlling modes were used: angle control (A control) by cycling between two selected rotation angles registered by RVDT, and torque control (T control) by cycling between two selected torque values (T_{max} and T_{min}). Table 4 summarizes SNTT tests performed on Aug. 16th 2010. $R = T_{min}/T_{max}$. N = number of fatigue cycles. The first sample tested, GB1-1, is not included in Table 4 because it was fractured accidentally when tuning the testing machine.

4.1 SNTT deformation process via IR imaging

Using an infrared camera, the in-situ fracture process of epoxy samples during SNTT was examined. Figure 15 shows IR images and temperature profiles across the notch, as marked with blue line in Fig. 14, obtained from sample GB2-6 during monotonic loading.

Without loading, the temperature was uniform on the sample surface (Figure 15a). When torque was applied, the vicinity of the notch root region was subject to a tri-axial tensile stress state. In general, under IR imaging material at peak (or principal) tri-axial tensile stress (or at a localized material stretched state) region will show a relatively lower temperature compared to nearby lower tensile stress regions [Wang, H. 2002]. The temperature profile shown in Figure 15b exhibits this behavior where a relatively small temperature drop was observed in the vicinity of the notch region. It is noted that due to increase in strain energy in the sample, the overall temperature profile was increased as also shown in Fig. 14b. At the moment of the SNTT sample fracture, surface temperatures peaked at the notch location (Figure 15c) due to the release of surface energy upon fracture.

Table 4. Epoxy samples testing summary

	Monotonic loading								
Sample	**Material**	**Nominal geometry**	**Fracture Torque**	**Note**					
GB2-1	2	d=0.1", ψ = 45°, θ = 36°	774 lbf-in						
GB2-6	2	d=0.3", ψ = 45°, θ = 20°	447 lbf-in						
GB3-1	1	d=0.115", ψ = 90°, θ = 45°	338 lbf-in						
GB3-6	1	d=0.1", ψ = 45°, θ = 45°	384 lbf-in						
GB3-8	1	d=0.2", ψ = 45°, θ = 45°	343 lbf-in	Blunt notch root; root sharpened with razor blade					
GB3-9	1	d=0.3", ψ = 45°, θ = 45°	430 lbf-in	Blunt notch root					
GB4-1	1	d=0.115", ψ = 90°, θ = 45°	305 lbf-in						
GB4-4	1	d=0.1", ψ = 45°, θ = 45°	404 lbf-in						
MFG-1	3	d=0.1", ψ = 45°, θ = 45°	1013 lbf-in						
Fatigue									
Sample	**Material**	**Nominal geometry**	**Fatigue conditions**						**Note**
			Fatigue mode	**T_{max} (lbf-in)**	**T_{min} (lbf-in)**	**R**	**Freq (Hz)**	**N**	
GB1-2	1	d=0.1", ψ = 45°, θ = 36°	A control (5.17° – 6.43°)	400*	300*	0.75*	1	100K	*Values at fatigue start
			T control	450	350	0.78	1	3000	
			A control (7.50° – 8.75°)	500*	400*	0.8*	2	~ 2Ks	*Values at fatigue start
GB1-3	1	d=0.1", ψ = 45°, θ = 36°	T control	200	150	0.75	1	70K	
			T control	250	200	0.8	1	90K	
			T control	300	250	0.83	1	50K	
			T control	400	350	0.88	1	30K	
			T control	450	400	0.89	1	100K	
			T control	550	500	0.91	2	50K	
			T control	650	600	0.92	2	50K	
			A control (0.5° – 6.1°)	400*	0*	0*	0.1	1000	*Values at fatigue start
			A control (0.4° – 6.0°)	400*	0*	0*	2	2700	*Values at fatigue start
GB1-4	1	d=0.1", ψ = 45°, θ = 36°	A control (1.2° – 4.8°)	300*	30*	0.1*	1	16164	*Values at fatigue start
GB1-5	1	d=0.1", ψ = 45°, θ = 36°	T control	200	20	0.1	1	50K	
			T control	300	30	0.1	1	6316	
GB2-3	2	d=0.2", ψ = 45°, θ = 28°	T control	300	30	0.1	2	100	root sharpened with razor blade
GB2-4	2	d=0.2", ψ = 45°, θ = 28°	T control	300	30	0.1	1	1660	root sharpened with razor blade
GB2-5	2	d=0.3", ψ = 45°, θ = 20°	T control	100	10	0.1	1	60K	
			T control	100	10	0.1	2	1.2M	
			T control	100	10	0.1	2	0.7M	
			T control	100	10	0.1	2	1M	
			T control	150	15	0.1	1	41795	root sharpened with razor blade
GB3-2	1	d=0.115", ψ = 90°, θ = 45°	T control	200	20	0.1	1	5139	
GB3-4	1	d=0.1", ψ = 45°, θ = 45°	T control	300	30	0.1	1	2369	
GB3-5	1	d=0.1", ψ = 45°, θ = 45°	T control	300	30	0.1	1	220	
GB4-2	1	d=0.115", ψ = 90°, θ = 45°	T control	200	20	0.1	1	3308	
GB4-5	1	d=0.1", ψ = 45°, θ = 45°	T control	200	20	0.1	1	~ 10K	Fractured after another 80 cycles between 25 and 250 lbf-in
MFG-2	3	d=0.1", ψ = 45°, θ = 45°	T control	600	60	0.1	1	500	
MFG-3	3	d=0.1", ψ = 45°, θ = 45°	T control	300	30	0.1	1	7084	

Monotonic loading of fatigued samples									
Sample	**Material**	**Nominal geometry**	**Fatigue conditions**					**Fracture Torque (lbf-in)**	**Note**
			Fatigue mode	**T_{max} (lbf-in)**	**T_{min} (lbf-in)**	**R**	**Freq (Hz)**	**N**	
GB1-6	1	d=0.1", $\psi = 45^o$, $\theta = 36^o$	T control	300	30	0.1	1	5500	596	
GB1-7	1	d=0.1", $\psi = 45^o$, $\theta = 36^o$	T control	200	20	0.1	1	260K	357	
GB2-2	2	d=0.1", $\psi = 45^o$, $\theta = 36^o$	T control	200	20	0.1	1	150K	865	
GB3-3	1	d=0.115", $\psi = 90^o$, $\theta = 45^o$	T control	200	20	0.1	1	3000	244	
GB3-7	1	d=0.1", $\psi = 45^o$, $\theta = 45^o$	T control	200	20	0.1	1	9000	618	Blunt notch root; root sharpened with razor blade
GB4-3	1	d=0.115", $\psi = 90^o$, $\theta = 45^o$	T control	200	20	0.1	1	4000	235	
GB4-6	1	d=0.1", $\psi = 45^o$, $\theta = 45^o$	T control	200	20	0.1	1	9000	281	

Material type: 1 – 117LV/229; 2 – 117LV/XH10B; 3 – RIM135/RIMH1366

The qualitative and quantitative measurement of temperature profiles obtained from this study proved to be very useful in SNTT failure characterization. However, accurate measurements require knowledge of surface emissivity, which is not only dependent on the material itself, but also on the surface roughness and the local curvature. Nevertheless, the preliminary IR results verified that the notch groove was subject to tensile states while under SNTT pure torsion loading (Figure 15b).

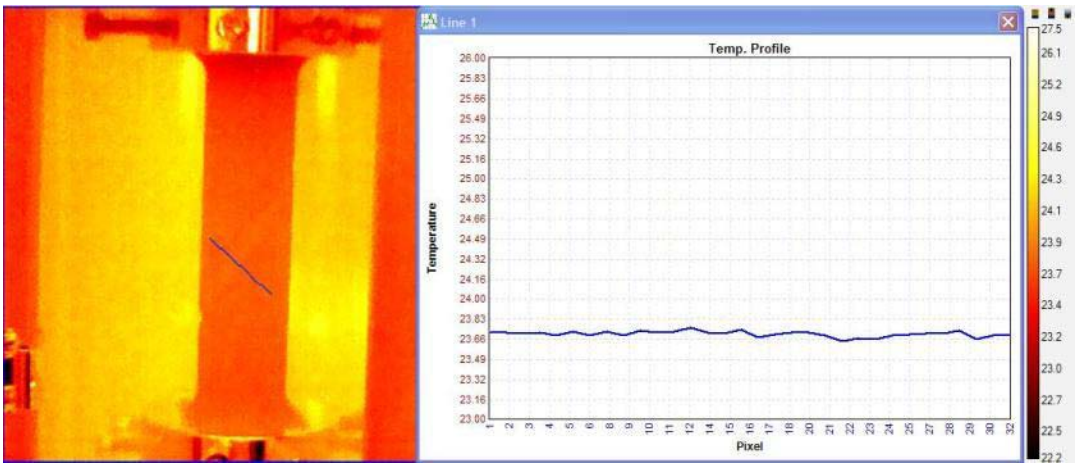

(a)

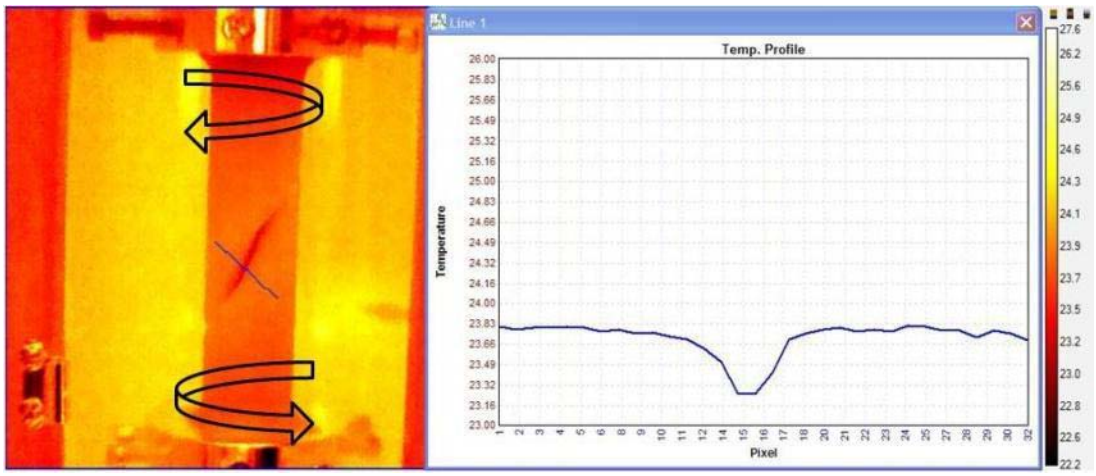

(b)

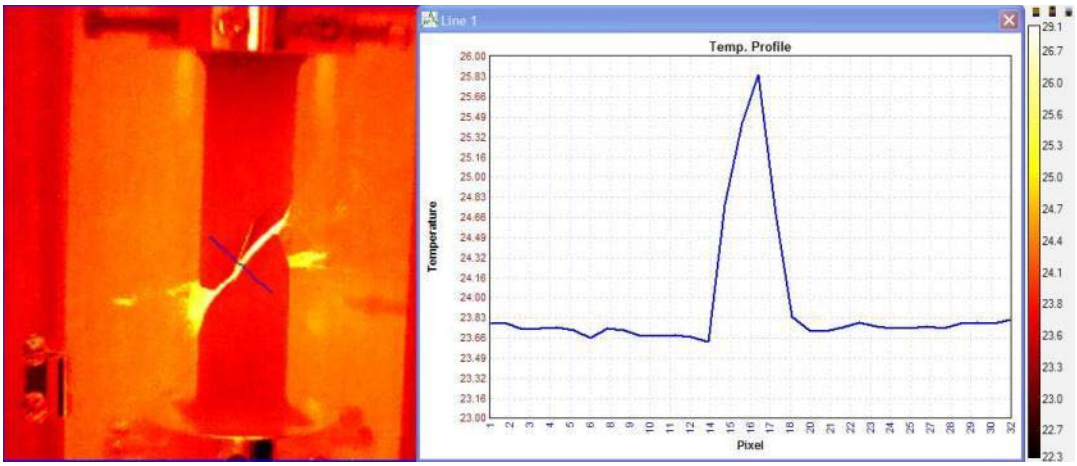

(c)

Figure 15. IR images of an epoxy sample during SNTT testing: (a) before testing, (b) during monotonic loading, and (3) at fracture instance.

4.2 Fracture due to monotonic loading

For tested epoxy samples, torque versus rotation angle curves showed typical brittle fracture behaviors with nearly linear load-displacement relationships (Figure 16). All samples failed near or below 400 lbf-in, except for the MFG-1 sample and two samples GB2-1 and GB2-6 that were made from toughened epoxies.

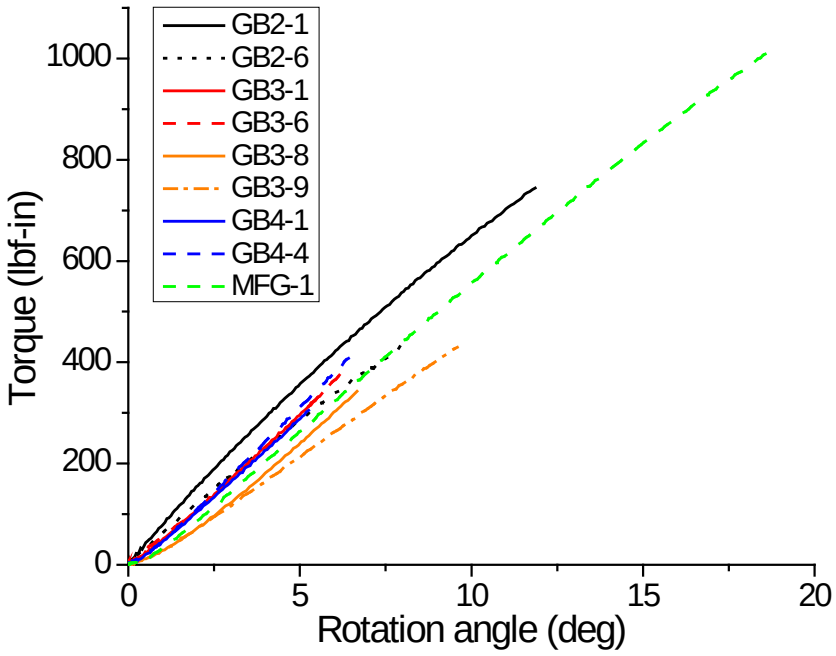

Figure 16. The torque-rotation plots of tested SNTT samples

Due to the geometric constraint and pure torsion loading, sample MFG-1 fractured into two halves along the spiral line (Figure 17a). However, the fracture surface showed a significant degree of roughness (Figure 17b). There were two distinct regions on the fracture surface: a quasi-circular region that had a smooth morphology and a rough region that surrounded the smooth region (Figure 17b). In contrast to the smooth region, which was relatively featureless, the rough region consisted of ridges and furrows that radiated from the border between the two regions and ran parallel along the crack propagation directions (indicated by arrows) (Figure 17b).

The smooth region, sometimes called “mirror” [Araki 2002], was likely formed as a result of slow unstable crack growth, this subsequently transformed to a rough region due to fast unstable crack growth [Owen 1975]. The rough region was sometimes termed as hackle [Phillips 1978, Yamini 1979] similar to those observed in glassy materials [Quinn 2007]. The ridged features in the rough region could be caused by secondary fractures as a result of the increased propagation speed of the primary crack [Owen 1975].

(a) (b)

Figure 17. Pictures showing (a) the fractured MFG-1 sample, and (b) its fracture surface.

The fracture surfaces of samples GB2-1 and GB2-6 showed similar features as those observed on MFG-1 (Figure 18). However, the size of the smooth region on GB2-1 and GB2-6 is larger than on MFG-1. In addition, some detached fibers were observed in the rough regions on samples GB2-1 and GB2-6 (Figure 18). These fibers could be formed by brittle cleavage from the ridges [Cherry 1981].

It is noted that both GB2-1 and GB2-6 were mixed-mode samples, because the pitch angles of the spiral notches were away from 45^{o} (Table 3). As mentioned in Section 3.2, when $\theta \neq 45^{o}$, the groove line region is subjected to Mode I + Mode III

stresses while under pure torsion loading. However, for both GB2-1 and GB2-6, the actual final brittle fracture still took place at a 45^{o} pitch angle with respect to the sample axis, rather than along the notch line (Figure 19).

The fracture torque of GB2-6 was 447 lbf-in, about 42% lower than the fracture torque of GB2-1 (774 lbf-in) because the notch depth of GB2-6 was nominally 0.3” while that of GB2-1 was 0.1” nominally (Table 4).

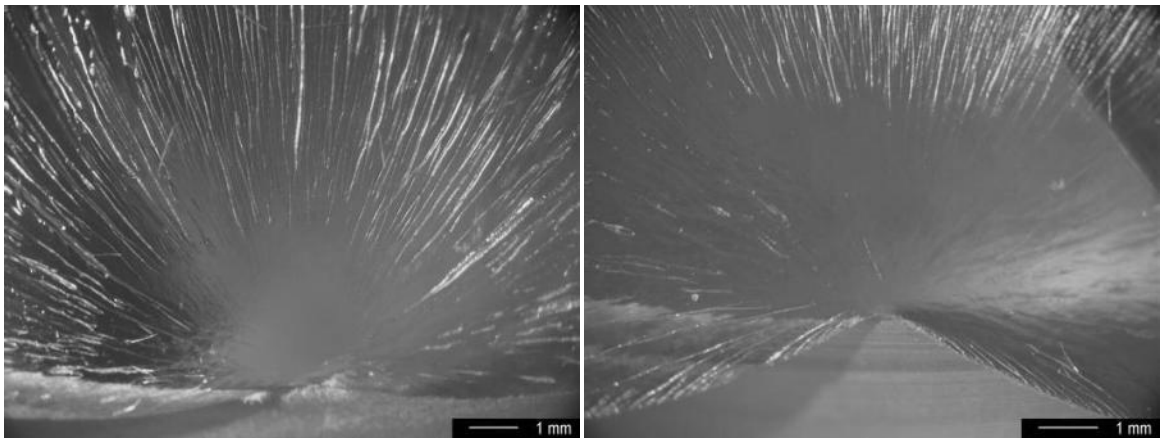

(a) (b)

Figure 18. Images showing the fracture surfaces of (a) GB2-1 and (b) GB2-6.

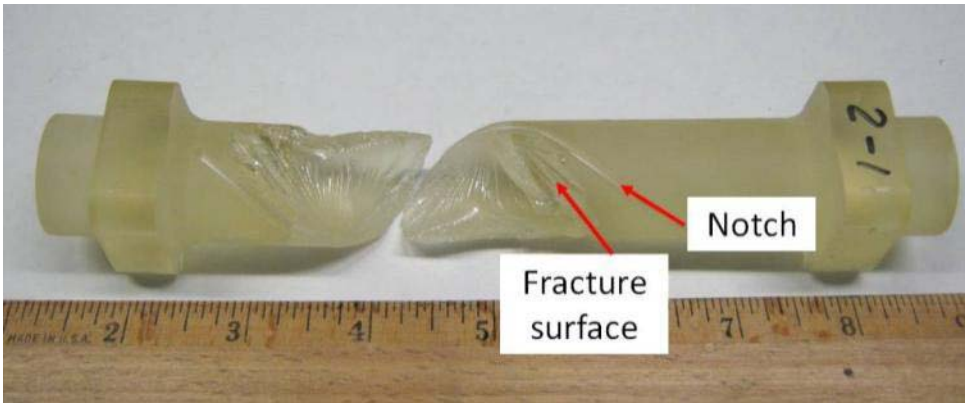

Figure 19. Sample GB2-1 after fracture.

Samples GB3-1, GB3-6, GB4-1, and GB4-4 all had a pitch angle of 45^{o} (Table 3), and their fracture surfaces resemble the “45^{o} spiral planes”. In another good example, Figure 20 shows the fracture surface of GB3-1, which initiated exactly along 45° spiral notch line.

The fracture surface of GB3-1 also contained both the smooth region and the rough region that was caused by slow and fast unstable crack propagations respectively (Figure 21a). A higher magnification image further revealed some fine river lines near the notch root (indicated by an arrow in Figure 21b). These river lines were characteristics of stable crack growth [Owen 1975]. The stable crack growth was a

small fraction of the entire fracture surface (Figure 21a), implying that under monotonic loading a crack would grow unstably shortly after its formation.

Figure 20. Picture showing one fractured half of sample GB3-1.

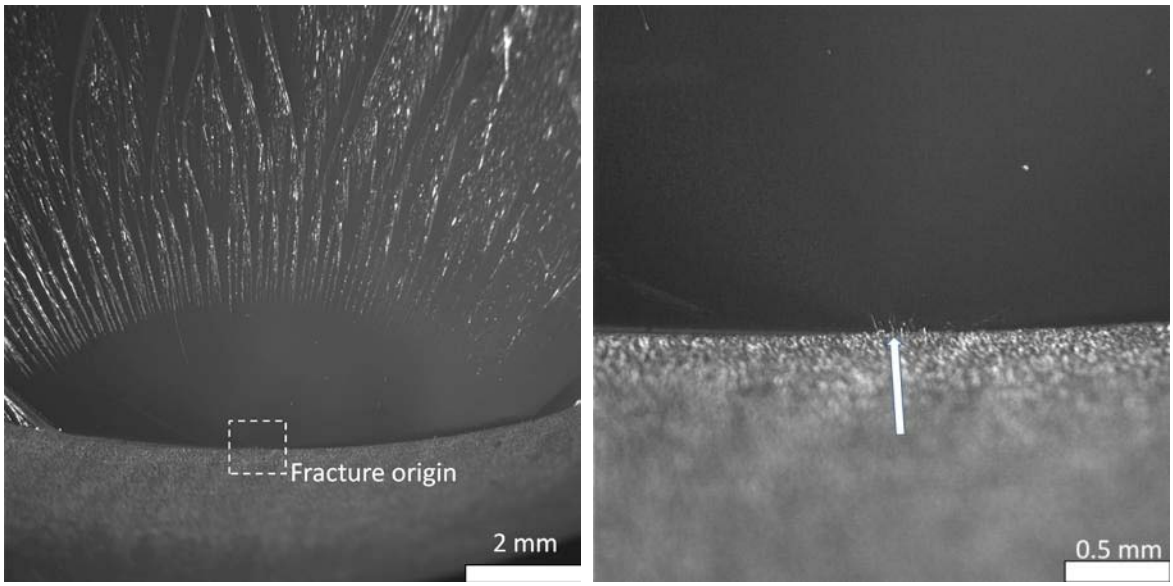

(a) (b)

Figure 21. Images showing (a) the fracture surface and (b) the fracture origin of sample GB3-1.

The fracture surfaces of GB3-6, GB4-1, and GB4-4 showed similar morphology to that of GB3-1 (Figure 22). GB3-1 and GB4-1 had comparable fracture torques (Table 4) due to their similar geometry. GB3-6 and GB4-4 exhibited higher fracture torques due to their smaller notch depth (0.1”) than that of GB3-1 and GB4-1 (0.115”) (Table 3). It is noted that the notch opening angles were different as well (45° versus 90°, see Table 3) and that the effect of the notch opening angle on fractures will be explored in the future.

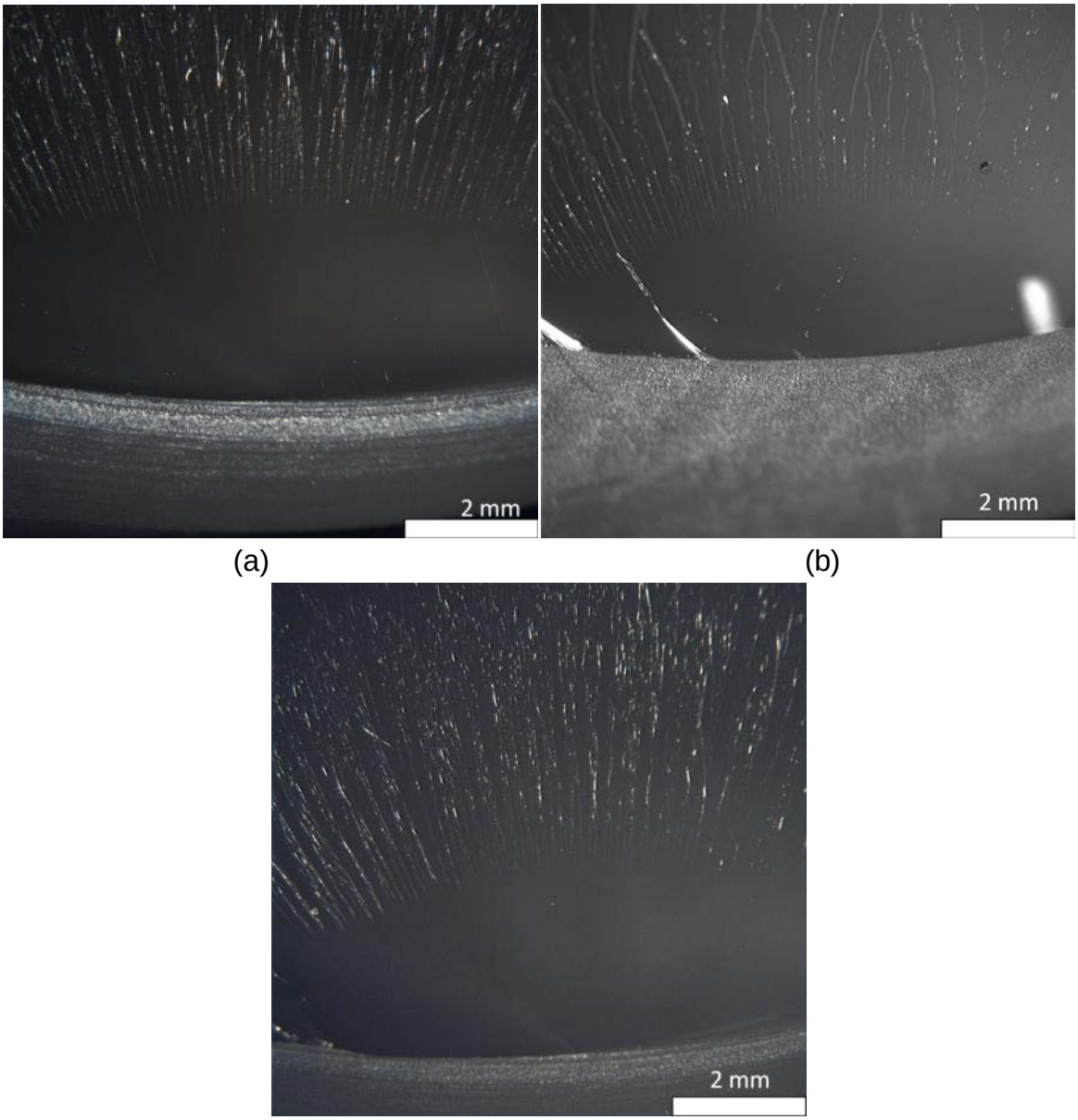

(a) (b)

(c)

Figure 22. Images showing fracture surfaces of (a) GB3-6, (b) GB4-1, and (c) GB4-4.

Samples GB3-8 and GB3-9 had similar geometry to samples GB3-6 and GB4-4, except that the notch depth was 0.2” for GB3-8 and 0.3” for GB3-9, while both GB3-6 and GB4-4 had a notch depth of 0.1” (Table 3). However, GB3-9 showed a higher fracture load (430 lbf-in) than GB3-6 (384 lbf-in) and GB4-4 (404 lbf-in). The fracture surface of sample GB3-9 consisted of a very smooth region away from the notch surrounded by a very rough region (Figure 23b).

Samples GB3-9, GB3-8, and GB3-7 were machined by a different company and it was found that their notch roots were U-shaped (or a dull notch root radius) rather than a sharp V-shaped. Thus, the GB3-9 sample presents a typical dull/blunt crack tip scenario with the observed fracture origin found to be inside the bulk material, rather

than on the surface (Figure 23b). Based on this finding, the notch root of GB3-8 was sharpened using a razor blade prior to testing. The resulting fracture surface of GB3-8 showed a similar appearance to those with V-shaped grooves (Figure 23a)with a fracture torque of 343 lbf-in (Table 4).

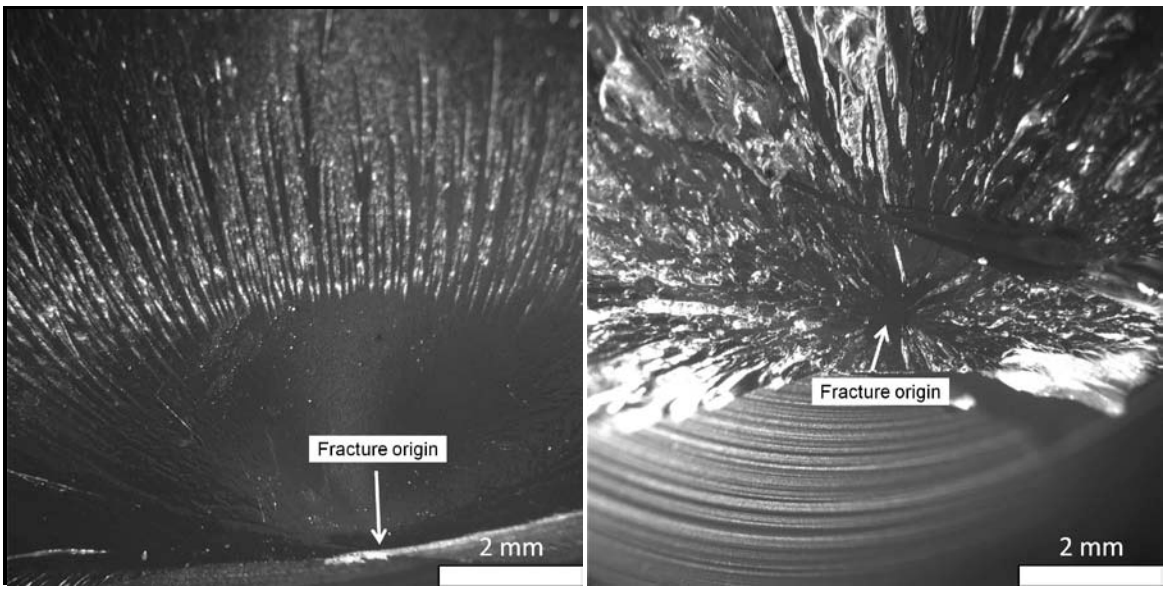

(a) (b)

Figure 23. Images showing the fracture surfaces of (a) GB3-8 and (b) GB3-9.

4.3 Fracture due to fatigue

In addition to the intrinsic material properties, the fatigue behavior of polymeric materials is also influenced by loading conditions, such as stress amplitude ($\Delta\sigma = \sigma_{max} - \sigma_{min}$), stress ratio ($R= \sigma_{min} /\sigma_{max}$) and thus the mean stress, and loading rate ($\sigma'=d\sigma/dt$) (Figure 24). In order to develop an effective protocol to induce a controllable crack growth, pilot testing was carried out where the epoxy samples were tested under different fatigue loading conditions (Table 4).

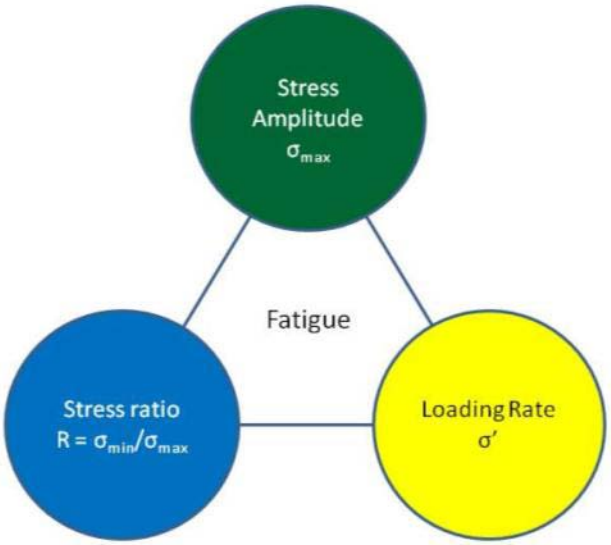

Figure 24. External factors influencing the fatigue behavior of materials.

Sample GB1-2 was fatigued with an angle (or displacement) control approach. The initial test was carried out under a fixed rotation angle range corresponding to a torque range between 300 and 400 lbf-in. The sample did not show fatigue crack growth after 100,000 cycles, based on the observed unchanged specimen stiffness, at a fatigue frequency of 1 Hz. In contrast, when the frequency was increased to 2 Hz with a torque range between 400 and 500 lbf-in, the sample fractured after a few thousand cycles (Figure 25). Thus, it seems that the fatigue life of epoxy materials can be shortened significantly by increasing the loading rate. On the other hand, sample GB1-5 survived 50,000 cycles when fatigued between 20 and 200 lbf-in, but failed after 6316 cycles when the torque range was changed from 30 to 300 lbf-in (Figure 25). Thus, increasing the stress amplitude could also decrease the fatigue life.

Sample GB1-3 survived more than 440,000 cycles under a variety of fatigue conditions (Table 4), where the maximum load reached 650 lbf-in for 50,000 cycles, without obvious stiffness change. However, GB1-3 fractured after 2700 cycles when ΔT ($= T_{max} - T_{min}$) was increased from 50 lbf-in to 400 lbf-in while the maximum torque was reduced from 650 lbf-in to 400 lbf-in and the fatigue frequency was increased from 1 Hz to 2 Hz (Figure 25). This may also imply that the synergistic effect of loading rate and stress amplitude can significantly reduce the fatigue life. It is noted that $R > 0.75$ for the first 440, 000 cycles while $R = 0$ for the last 2700 cycles. The fatigue loading rate effect observed from this pilot study presents a unique characteristic of polymeric material, which is not normally observed in a cycle fatigued metallic material. This may also imply that the polymeric material failure is likely to be loading rate dependent. In general the higher loading rate will decrease the ductility; thus, reducing the fracture toughness. Furthermore, as observed from IR images, the notch region appears to have a lower temperature profile compared to the rest of the sample. Since polymeric material

normally has lower thermal conductivity (compared to that of metallic materials, higher rate loading will further increase the temperature gradient near the crack tip region. The lower localized temperature profile at the crack front will certainly increase the localized constraint leading to lower fracture toughness and thus less fracture resistance.

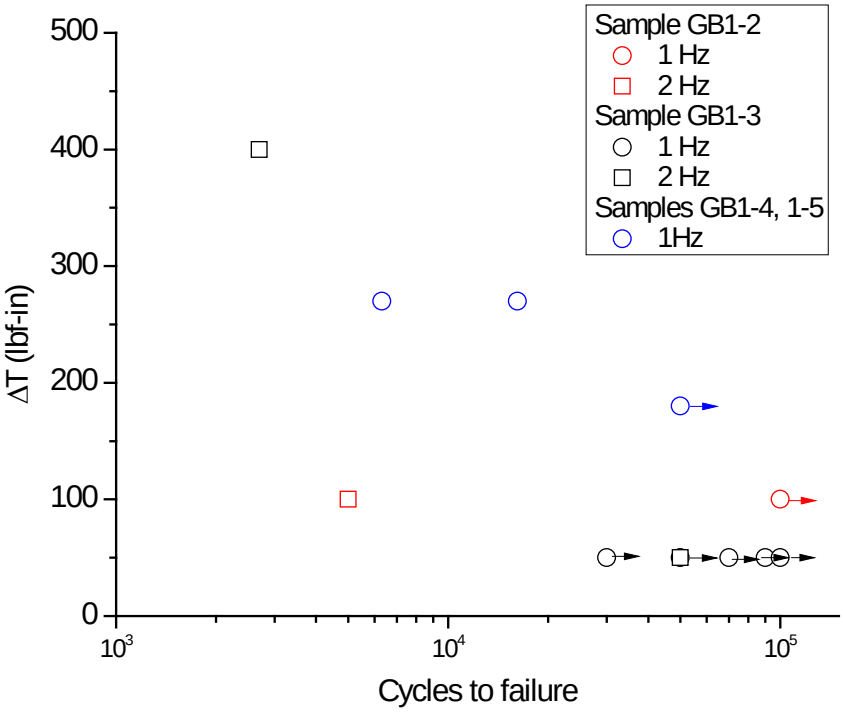

Figure 25. Fatigue S-N plots of samples from GB batch 1.

Based on lessons learned from GB1-2 and GB1-3 fatigue testing, levels of ΔT ≅ 300 lbf-in and a maximum Torque of 300 lbf-in were chosen as fatigue loading conditions for the following fatigue test. Sample GB1-4 was fatigued between 30 and 300 lbf-in with a frequency of 1 Hz and failed after 16,164 cycles (Figure 25). Three distinct regions were observed on the fracture surface: 1) a clam-shell shaped region, 2) a smooth region surrounding the clam-shell region, 3) and a rough region with ridges and furrows (Figure 26). The clam-shell region was probably formed during the fatigue phase, where the crack grew stably. The smooth region probably was created by slow unstable crack growth while the rough region was formed when crack propagation accelerated. Similar features were observed on the fracture surface of sample GB1-5: with the stable fatigue crack growth region, the slow unstable crack growth region, and the fast unstable crack growth region all visible (Figure 27).

In contrast, no fatigue region was observed on samples GB1-2 or GB1-3, where only the unstable crack growth regions were visible (Figure 28). The lack of fatigue region implies that no significant fatigue crack growth took place in these two samples

even though they were fatigued for more than 100,000 and 440,000 cycles, respectively.

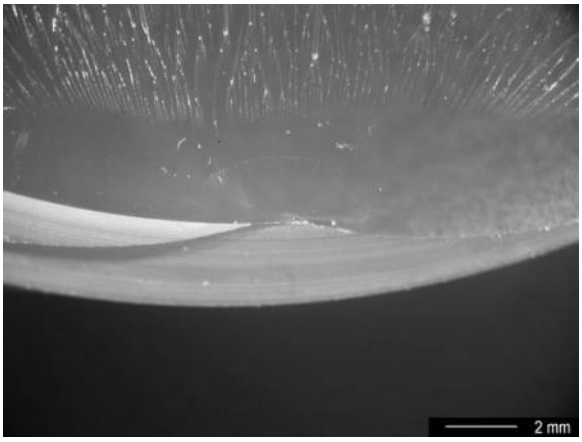

Figure 26. Fracture surface of sample GB1-4.

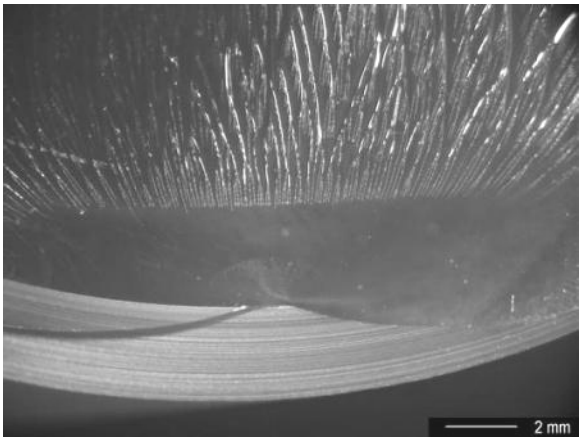

Figure 27. Image showing the fracture surface of GB1-5.

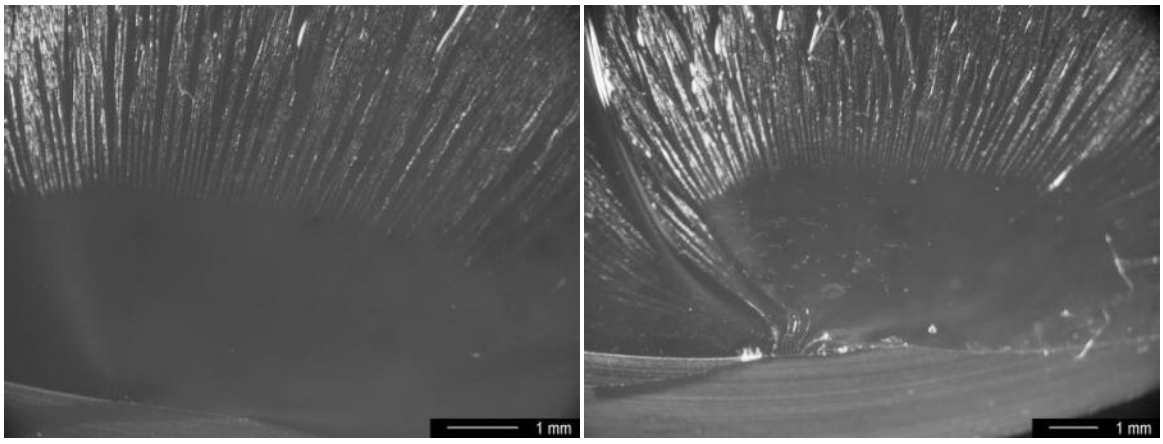

(a) (b)

Figure 28. Images showing the fracture surfaces of (a) GB1-2 and (b) GB1-3.

Samples GB1-2, GB1-3, GB1-4 and GB1-5 were all mixed mode samples with a pitch angle of 36^o (Table 3). However, both the stable crack growth (fatigue) and the unstable crack growth revealed that the fracture surface and crack growth occurred on a plane with a 45^o pitch angle with respect to the SNTT sample axis. Thus, the spiral plane corresponding to Mode I loading with a 45^o pitch angle is the preferred crack growth plane for these epoxy materials. Adams and Odom [Adams 1992] studied the fatigue failure of several brittle polymers including an epoxy resin, and discovered that they all failed in tensile mode even when they were subject to torsional fatigue.

Samples of the second batch from Gougeon Brothers were made from toughened epoxies (Table 1). Prior to fatigue testing, the notch roots of GB2-3, GB2-4, and GB2-5 were sharpened with a razor blade by manually sliding the blade along the spiral notch. GB2-3 fractured after 100 cycles between 30 and 300 lbf-in with a frequency of 2 Hz; while GB2-4 fractured after 1660 cycles between 30 and 300 lbf-in with a frequency of 1 Hz (Table 4). The short fatigue life of these two samples was perhaps a result of increasing constraint due to notch root sharpening. No fatigue region was observed on samples GB2-3 or GB2-4 (Figure 29).

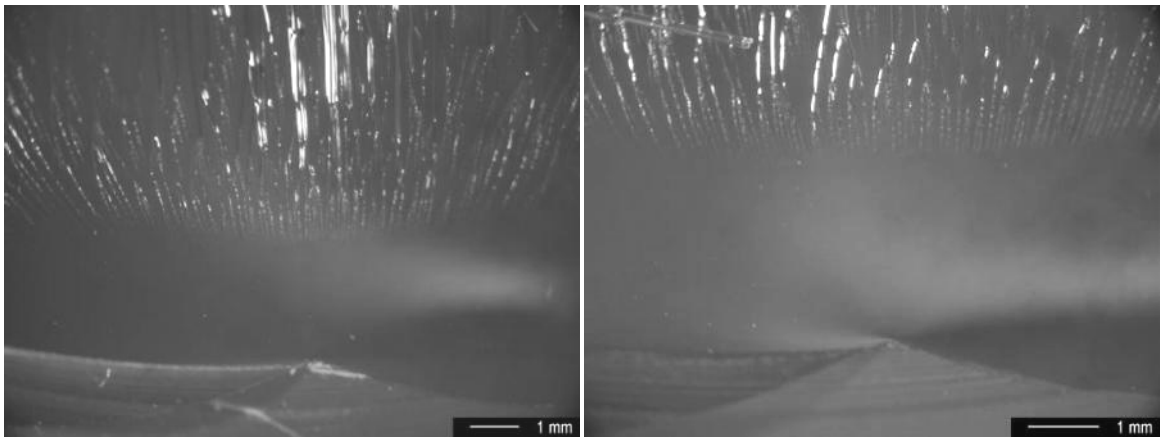

(a) (b)

Figure 29. Images showing the fracture surfaces of (a) GB2-3 and (b) GB2-4.

Sample GB2-5 survived more than three million fatigue cycles, because of the small T_{max} value (< 100 lbf-in, Table 4) and ΔT =90 lbf-in. The sample finally fractured at 41,975 cycle with ΔT =90 lbf-in and T_{max} = 150 lbf-in. On the fracture surface, a clam-shell shaped fatigue region was clearly identified (Figure 30a). In this region, river lines radiated along the direction of the crack propagation, and concentric semi-elliptical lines perpendicular to the river lines were also visible at a higher magnification (Figure 30b). These concentric lines could be striation lines [Yamani 1979, 1980, Cherry 1981] generated during fatigue loading. Using the optical microscope, the spacing between adjacent striation lines measured approximately 0.1 mm (Figure 30b), while the SEM

image showed striation lines on a much finer scale with a spacing around 10 microns (Figure 31a). Thus, the striation lines observed in Figure 30b are believed to represent the unique crack growth cycles of polymeric materials with fatigue aging.

The semi-elliptical region, similar to Figure 30, was also observed by other researchers on fracture surfaces subject to rotary-bending fatigue [Nagasawa 1995] and uniaxial fatigue [Tao 2007] of epoxy materials. In addition, Tao *et al.* observed striation lines with a spacing of a few microns on the stable fatigue crack propagation zone in uniaxially fatigued epoxies [Tao 2007]. The boundary between the fatigue crack growth region and the smooth region (Figure 31b) corresponds to the transition from stable crack growth to unstable crack propagation.

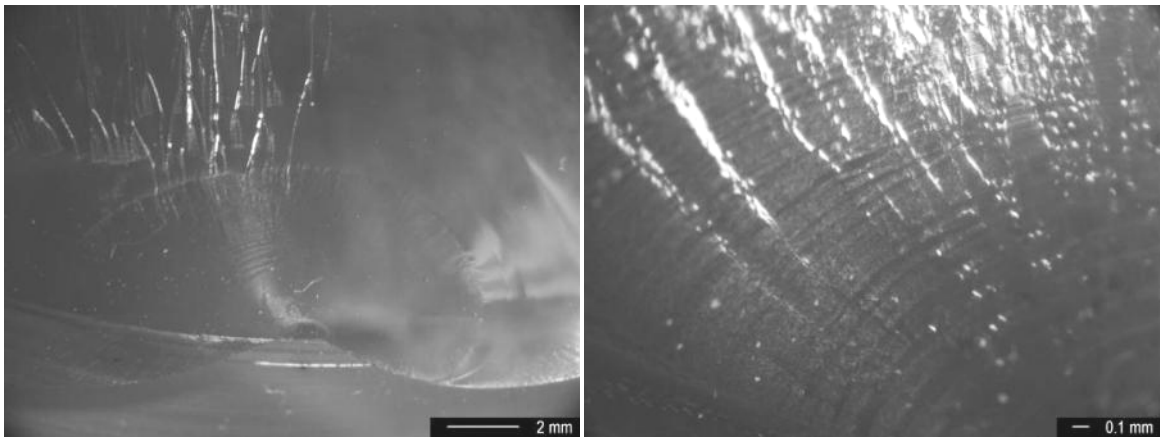

(a) (b)

Figure 30. Images showing (a) the fracture surface of GB2-5 and (b) the crack propogation striation lines.

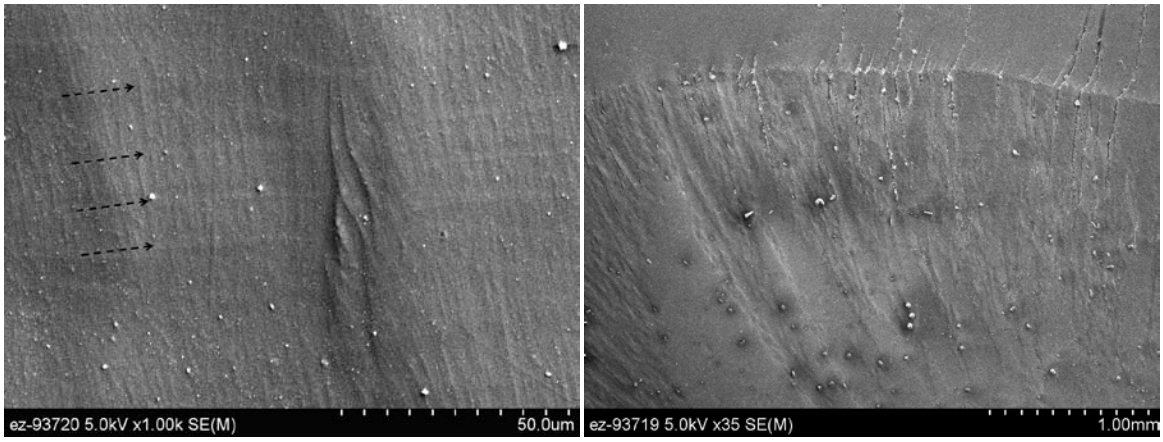

(a) (b)

Figure 31. SEM image of the striation lines observed in GB2-5.

The pitch angles of the notches on samples GB2-3, GB2-4, and GB2-5 were all smaller than 45^{o} (Table 3), however they fractured along the 45^{o} plane rather than the

notch plane. This observation agreed with the conclusion obtained from the first batch of samples: epoxy samples prefer to fracture in tensile opening mode, i.e., Mode I fracture.

Lessons learned from the early samples indicate that small R, small ΔT, and low fatigue frequency do not favor fatigue crack growth or controllable crack advance. In addition, it was difficult to maintain a constant R value using the angle control mode. The Haver function was used in fatigue cycle control with R > 0. Under displacement control, the R ratio will reduce progressively with increasing fatigue cycles, due to increased specimen compliance induced by fatigue crack growth. Thus, all subsequent fatigue tests were performed using torque (or load) control mode with an R value of 0.1 and a frequency of 1 Hz. T_{max} was selected to be approximately 60% of the torque that generated the maximum allowable shear stress on the surface of a SNTT sample.

Samples from batch 3 and batch 4 all had a 45° pitch angle. GB3-4, GB3-5 and GB4-5 had a nominal notch depth of 0.1" and a notch opening angle of 45°. GB3-2 and GB4-2 had a nominal notch depth of 0.115" and a notch opening angle of 90°. All were fatigued at 1 Hz with an R value of 0.1, and T_{max} = 200 or 300 lbf-in (Table 4).

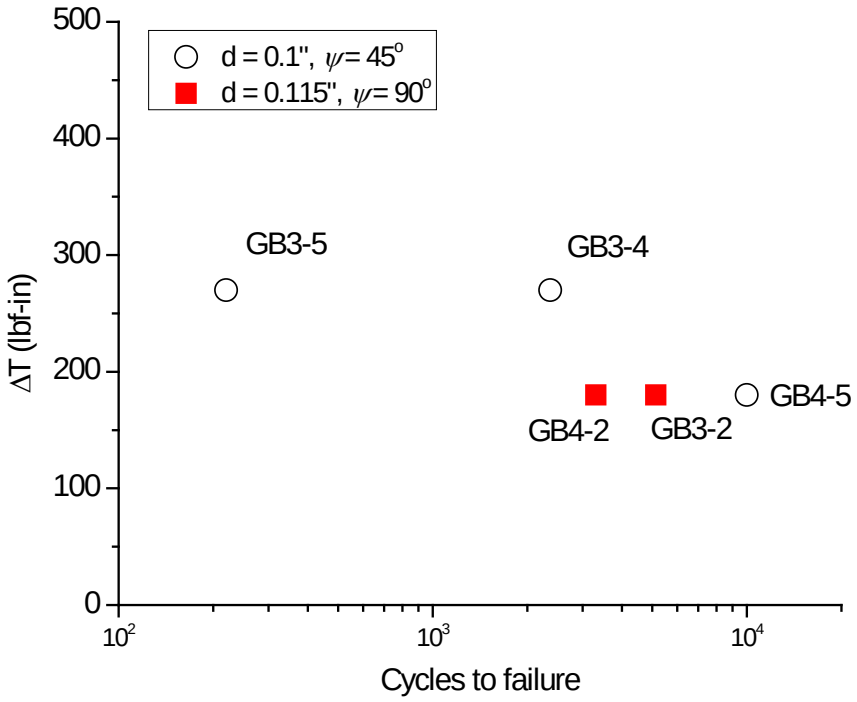

Figure 32. Fatigue S-N plots of samples from GB batch 3 and batch 4.

Compared to GB4-5, which failed after about 10,000 cycles, GB3-4 fractured after 2,369 cycles (Figure 32) because of a higher ΔT (270 lbf-in versus 180 lbf-in). GB4-2 and GB3-2 were both fatigued between 20 and 200 lbf-in with a frequency of 1 Hz. They exhibited comparable fatigue life: 5,139 cycles for GB3-2 and 3,308 for GB 4-2 (Figure

32). When compared to GB4-5, both GB3-2 and GB4-2 had shorter fatigue life (Figure 32), likely due to increased constraint induced by their deeper notches. GB3-5 was fatigued between 30 and 300 lbf-in with a frequency of 1 Hz. However, it is not clear why it fractured after only 220 cycles (Figure 32) while GB3-4 fractured after 2369 cycles when subjected to identical fatigue conditions. One possible explanation is that a surface flaw due to machining existed near the notch line region in the sample prior to fatigue. In fact, no crack growth region could be identified on the fracture surface of GB3-5 (Figure 33). In any event, the fatigue life difference between 220 cycles and 2369 cycles may well due to material inhomogeneity or anisotropy.

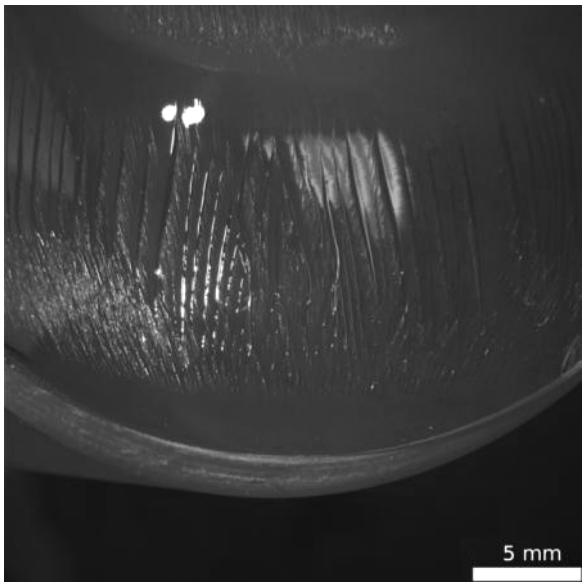

Figure 33. Fracture surface of GB3-5.

The fatigue regions on Mode I samples were expected to be a uniform band along the notch groove. However, the fatigue regions observed on the fracture surfaces of GB3-4 (Figure 34) and GB4-5 (Figure 35) were both long semi-ellipses. This deviation could be attributed to machining errors resulting in a pitch angle which deviated from 45^{o}. It is interesting to point out that a broad striation line was observed on sample GB4-5 (Figure 35b). It is unclear the cause of this striation band, therefore it will require further investigation.

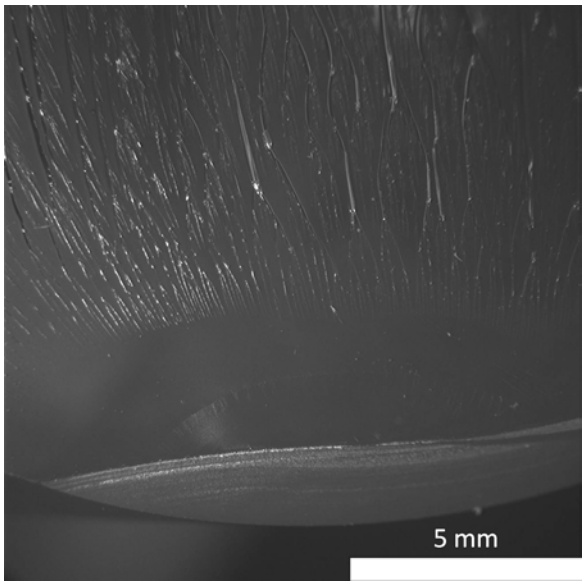

Figure 34. Fracture surface of GB3-4.

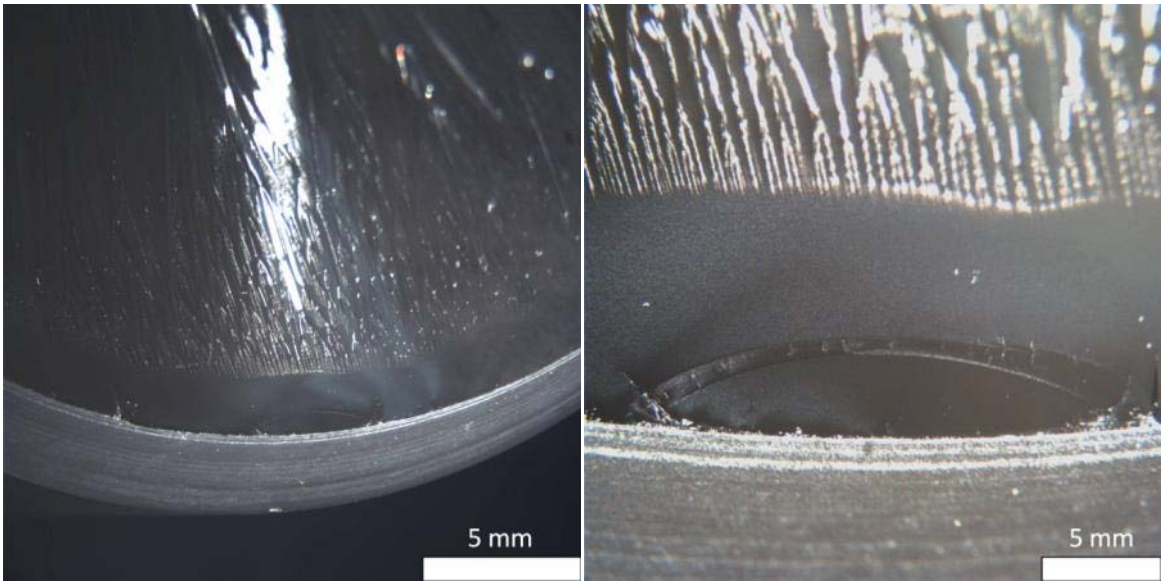

(a) (b)

Figure 35. Images showing the fracture surfaces of GB4-5.

In contrast, uniform smooth bands (the smooth regions) were clearly seen on samples GB 3-2 and GB4-2 (Figure 36 and Figure 37). Higher magnification images of the smooth regions showed parallel markings with comparable lengths formed at a right angle to the notch roots which extended into the smooth regions (Figure 36b). These markings were observed in fatigued polyester resins and were attributed to stable fatigue crack growth [Owen 1975]. The fatigue regions on GB3-2 and GB4-2 agreed well with the expectation that a uniform fatigue growth occurs on a Mode I sample.

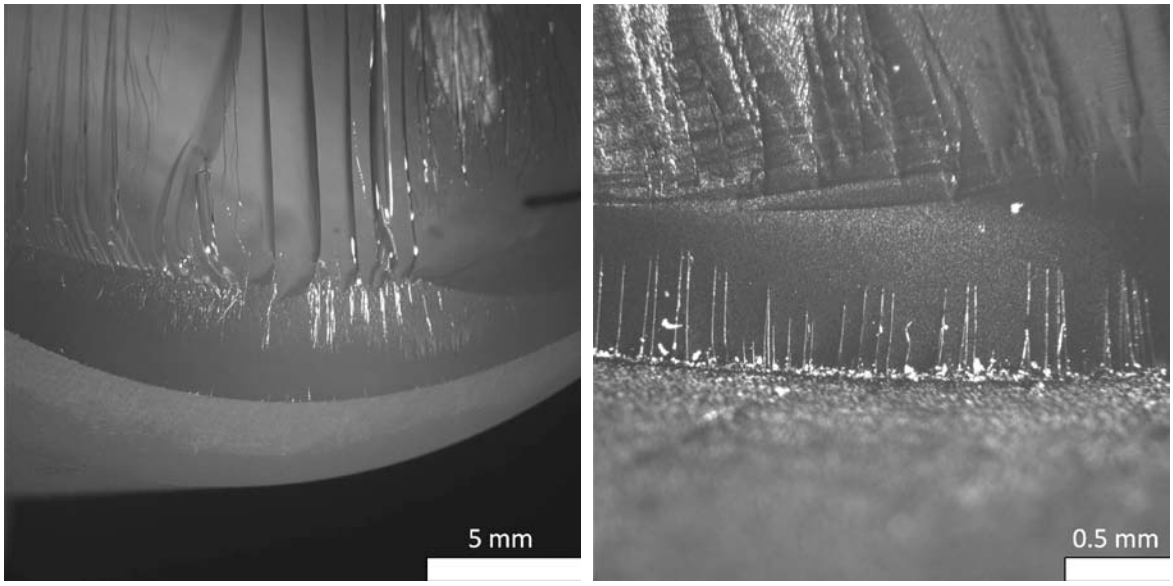

(a) (b)

Figure 36. Images showing the radial markings along the groove line of GB3-2.

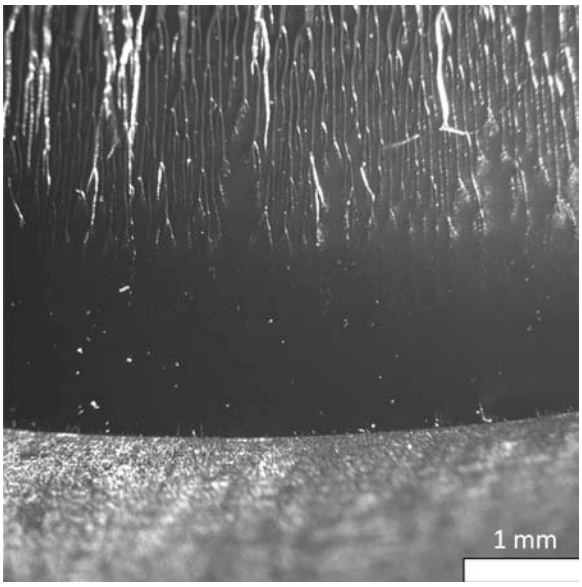

Figure 37. Images showing the uniform crack growth along notch line of GB4-2.

For GB3-2, the compliance change due to fatigue crack growth was monitored using both a rotary variable differential transformer (RVDT) and a biaxial extensometer (see Section 3.1). The extensometer measurements were taken every 1000 cycles. The torque versus rotation angle and shear strain were plotted in Figure 38a and Figure 38b, respectively.

For the rotation angle data measured from RVDT, the slope increased as a function of fatigue cycles, indicating an increase in sample stiffness or a decrease in sample compliance(Figure 38a). Strain accumulation could occur during cyclic loading

[Nagasawa 1995], which might lead to strain hardening. A similar stiffness increase was observed by Tao *et al*. [Tao 2007] in an epoxy material fabricated from Epon 826 Resin and Epi-Cure Curing Agent 9551. Tao and coworkers [Tao 2007] showed that the stress range increased with increasing fatigue cycles when the sample was cycled between a strain range of 0.02% to 3.68%; meanwhile, the stress range decreased with increasing cycles when the strain range involved both positive and negative strain values.

In contrast, a decrease in slope was observed in the extensometer measured data (Figure 38b). This seemed contradictory to the RVDT data. The RVDT measured the overall rotation of the entire sample, including the notched and un-notched regions; while the extensometer recorded the relative gage length displacement between the two probe pins across the notch. Therefore, the data measured by the extensometer is thought to give a more accurate estimate regarding localized deformation due to crack growth. Thus, the slope decrease in Figure 38b was a combined result from both crack growth induced compliance increases and hardening induced compliance decreases.

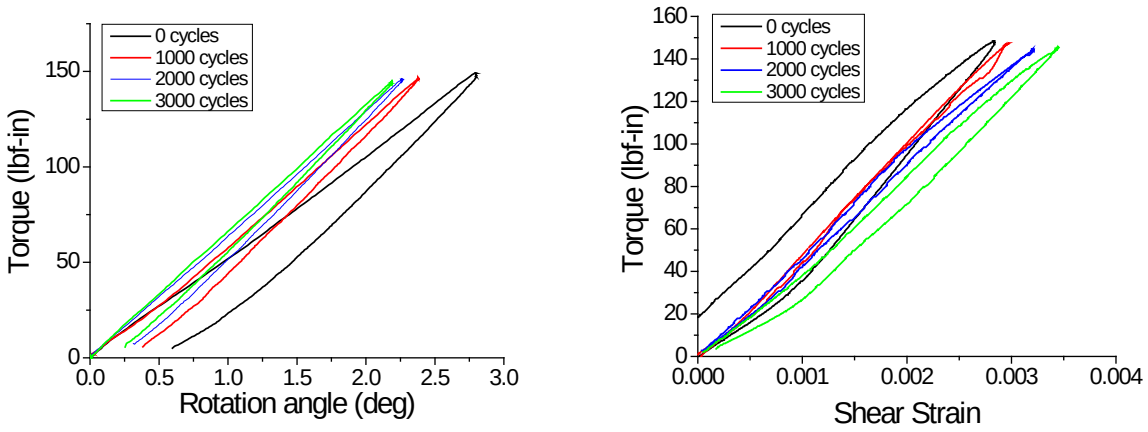

(a) (b)

Figure 38. Effect of fatigue on stiffness of sample GB3-2 as measured from (a) load cell and RVDT, and (b) load cell and biaxial extensometer.

Due to the limited number of samples, only two MFG epoxy samples were tested under fatigue: MFG-2 and MFG-3. MFG-2 was cycle fatigued between 60 and 600 lbf-in with a frequency of 1 Hz. However, the mechanical response of the testing machine was not fast enough to perform such test. The actual torque range was approximately 100 to 560 lbf-in. After about 500 cycles, MFG-2 fractured showing no obvious fatigue region on the fracture surface (Figure 39a). Some river lines were observed at the fracture origin (Figure 39b) indicating some fatigue crack growth.

In contrast to MFG-2, MFG-3 was fatigued between 30 and 300 lbf-in at 1 Hz and failed after 7084 cycles (Table 4). On the fracture surface, a uniform smooth band (Figure 40a), striation line, and unstable initiation line (Figure 40b) were all observed. In

addition, parallel river markings, characteristic of stable crack growth were also seen (Figure 40b). The river markings initially grew perpendicular to the notch root, but then deflected at approximately 0.7 mm into the sample at two different angles (Figure 40b). This interesting behavior perhaps was related to some preferred stress directions and will be further investigated in the future.

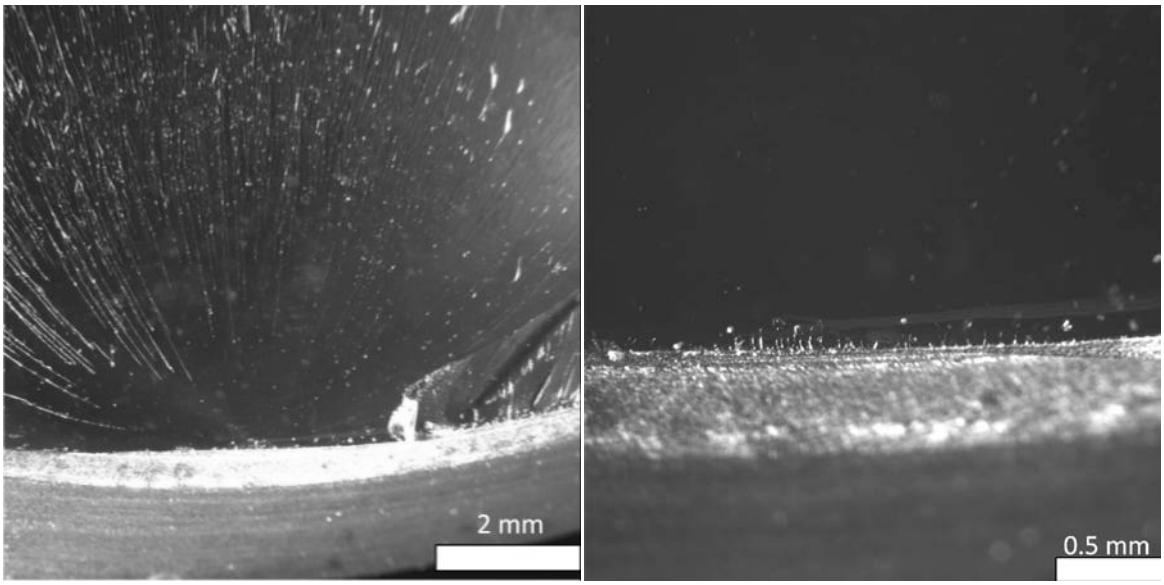

(a) (b)

Figure 39. Images showing the fracture surface of MFG-2.

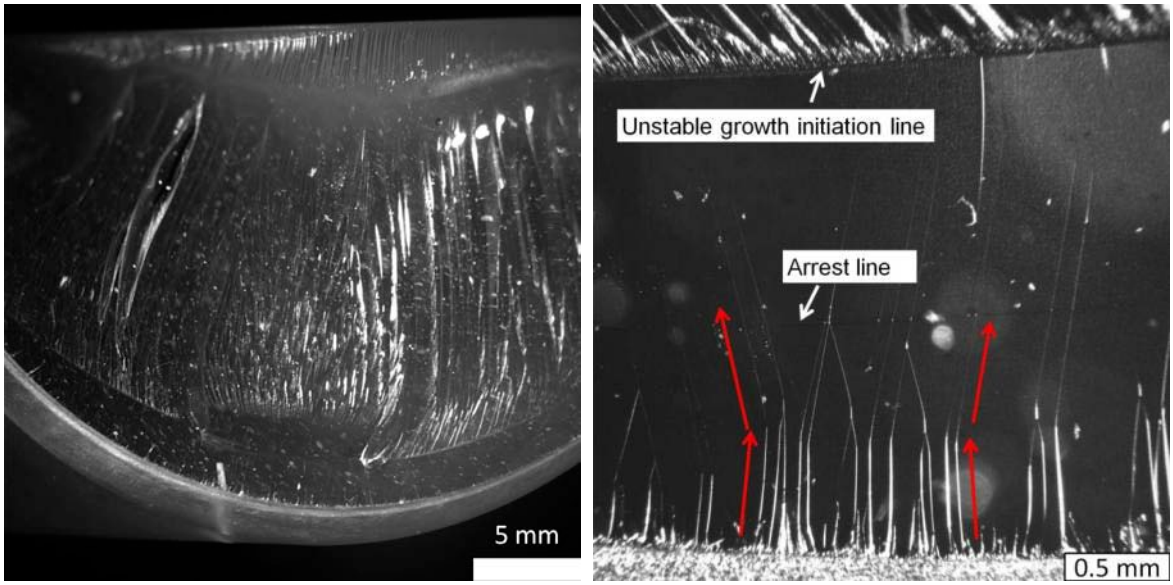

(a) (b)

Figure 40. Images showing the fracture surfaces of MFG-3.

4.4 Fatigue and monotonic loading

Creation of sharp pre-cracks is essential for accurate fracture toughness measurements in order to minimize the energy associated with plastic deformation. In this study, fatigue procedures described in the previous section (Section 4.3) were used to create pre-cracks in epoxy samples. The fatigued samples were then loaded monotonically to failure (Section 4.2).

Samples GB1-6 and GB1-7 were fatigued for 5500 cycles and 260,000 cycles, respectively. Their final monotonic loading curves are compared in Figure 41. Both samples showed linear elastic behavior and almost identical slopes (Figure 41). However, the fracture torque of GB1-6 was 596 lbf-in, approximately 67% higher than that of GB1-7, which fractured at 357 lbf-in (Table 4). It was probable that the lower fracture torque of GB1-7 was due to a deep pre-crack as a result of longer fatigue cycles.

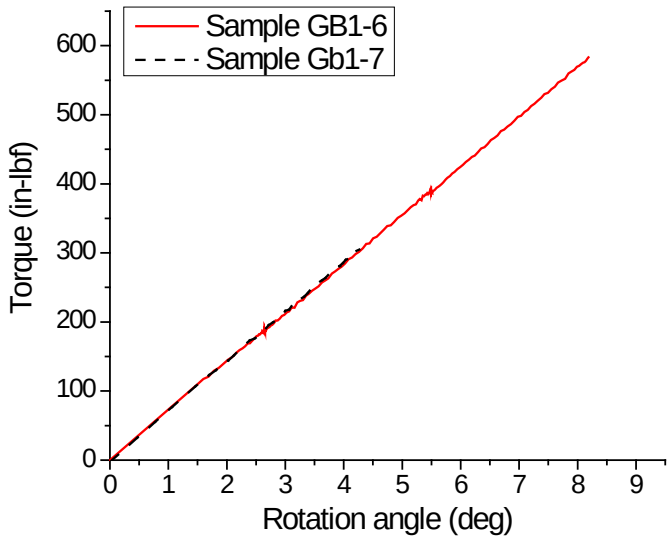

Figure 41. Monotonic loading curves of GB1-6 and GB1-7 after fatigue.

Fractographic analysis showed that no significant fatigue region could be identified on sample GB1-6 (Figure 42a); while in contrast a clam-shell fatigue region was observed on GB1-7, which could explain its lower fracture torque compared to GB1-6.

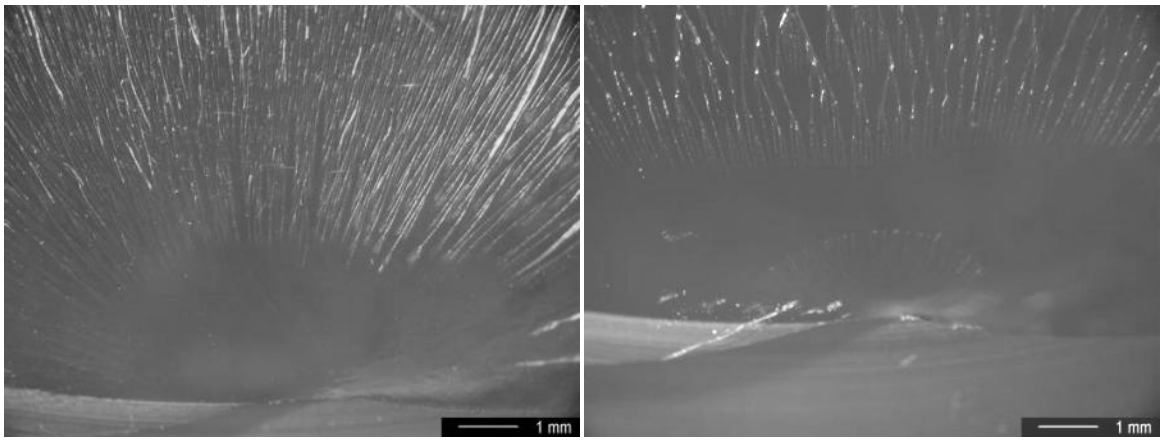

(a) (b)

Figure 42. Fracture surfaces of samples GB1-6 and GB1-7.

Sample GB2-2 was initially fatigued between 20 and 200 lbf-in for 150,000 cycles. Upon monotonic loading, GB2-2 fractured at 865 lbf-in, which was comparable to (in fact slightly higher than) sample GB2-1 without fatigue (Figure 43). This was due to a small peak loading torque being used in fatigue (200 lbf-in) so no pre-crack was generated in the fatigue stage. Microscopic examination also confirms that no significant fatigue crack growth developed in GB2-2 (Figure 44). The fracture surface of GB2-2 looked very similar to GB2-1 and GB2-6 (Figure 18), which were not fatigued prior to monotonic loading.

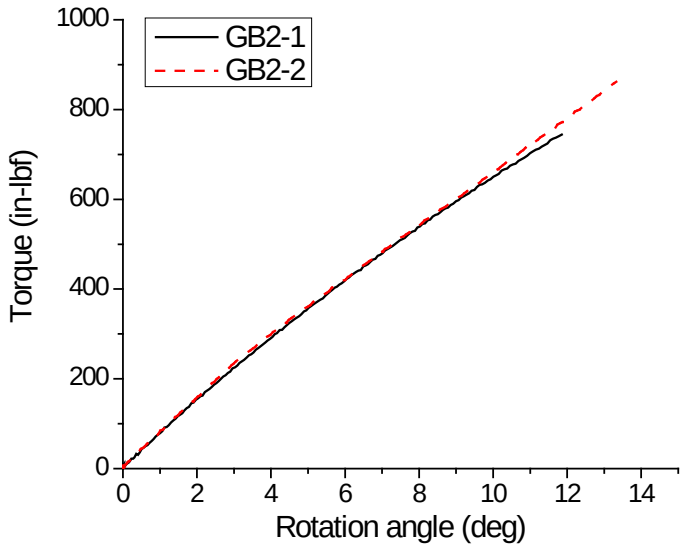

Figure 43. Comparison of the loading curves between GB2-1 and GB2-2.

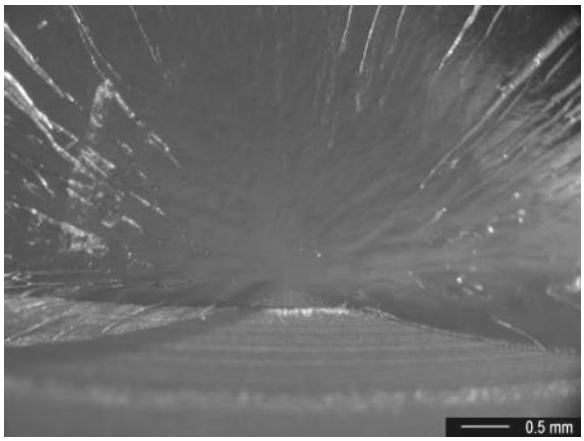

Figure 44. Fracture surface of GB2-2.

Sample GB4-6 was first fatigued between 20 and 200 lbf-in for 9000 cycles and then fractured at 281 lbf-in during monotonic loading. Compared to the fracture load of sample GB4-4 without fatigue (404 lbf-in), GB4-6 exhibited a 30% decrease (Figure 45). This was due to the introduction of fatigue cracks, which were clearly seen on the fracture surface of GB4-6 (Figure 46). However, a slight increase in the slope was observed on the loading curve of GB4-6 as compared to GB4-4 (Figure 45), which might be explained by strain hardening [Tao 2007] as seen in sample GB3-2 (Figure 38a).

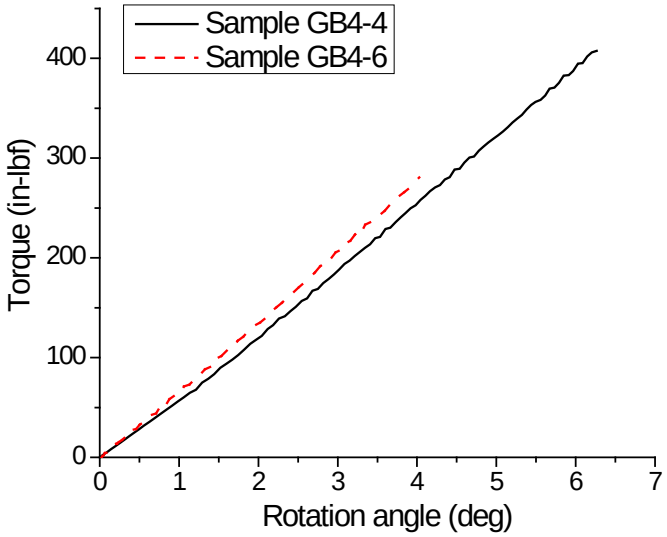

Figure 45. Comparison of the loading curves between GB4-4 and GB4-6.

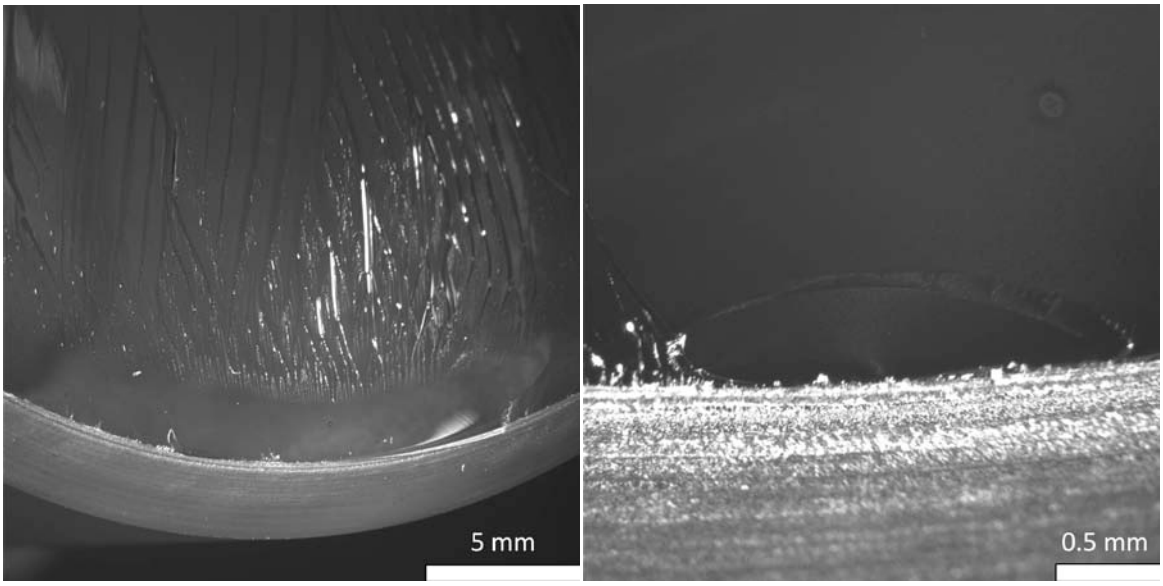

(a) (b)

Figure 46. Images showing the fatigued crack growth on fracture surface of GB4-6.

Samples GB3-1, GB3-3, GB4-1, and GB4-3 were nominally identical (Table 3). GB3-3 and GB4-3 were fatigued between 20 and 200 lbf-in for 3000 and 4000 cycles, respectively. Upon final monotonic loading, GB3-3 and GB4-3 showed comparable fracture torques and similar slopes (Figure 47). This indicates the SNTT testing protocol is reproducible. The two fatigued samples (GB3-3 and GB4-3) had lower fracture torques and higher slopes than the two samples without fatigue (GB3-1 and GB4-1) (Figure 47).

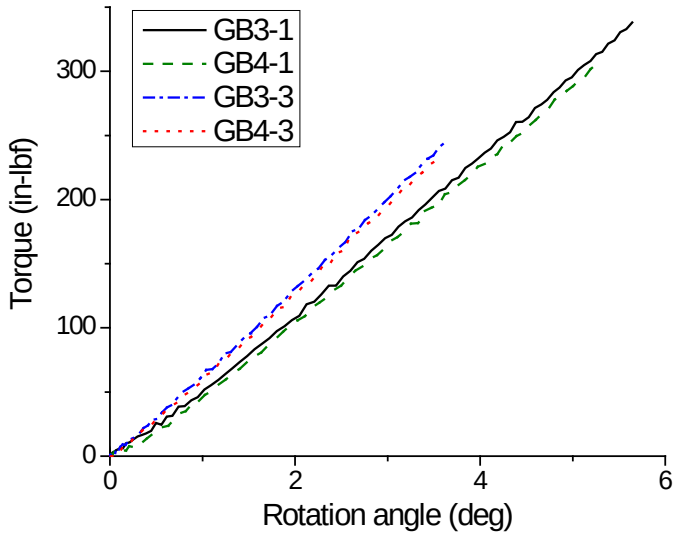

Figure 47. Comparison of the loading curves among GB3-1, GB3-3, GB4-1, and GB4-3.

Microscopy showed that fatigue pre-cracks were developed in both GB3-3 (Figure 48) and GB4-3 (Figure 49). Uniformly smooth regions parallel to the notch groove, characterizing the slow unstable crack growth regions (Figure 48a and Figure 49a), and river markings perpendicular to the grooves, as a result of stable crack growth (Figure 48b and Figure 49b), were observed in both samples. In addition, the striation line in GB4-3 was broad and relatively irregular (Figure 48b) compared to a thin line parallel to notch groove as seen in GB3-3 (Figure 49b).

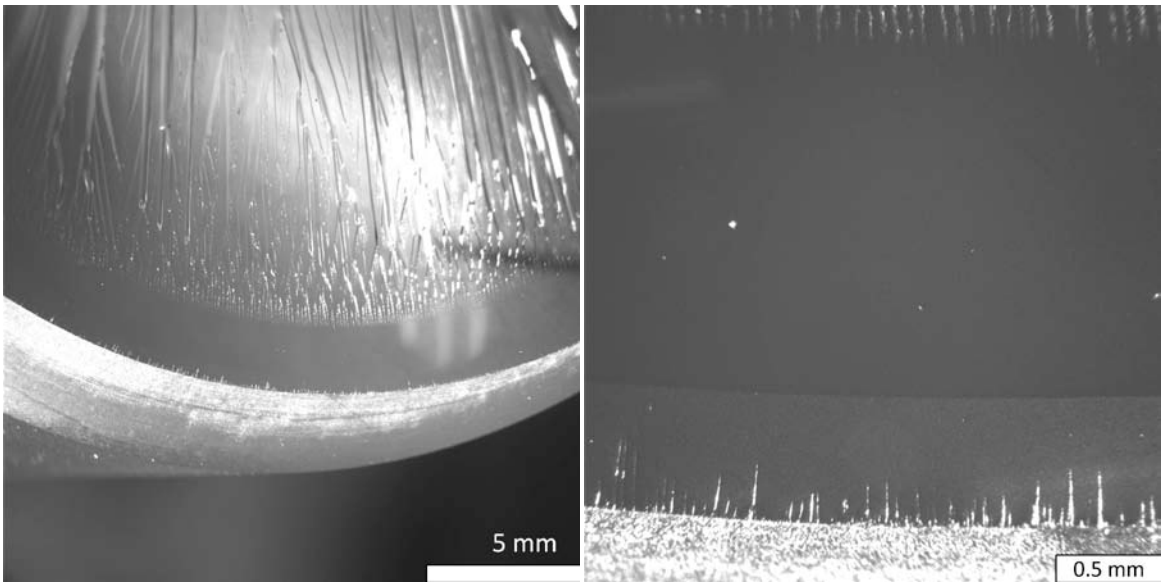

(a) (b)

Figure 48. Images showing the fracture surface of GB3-3.

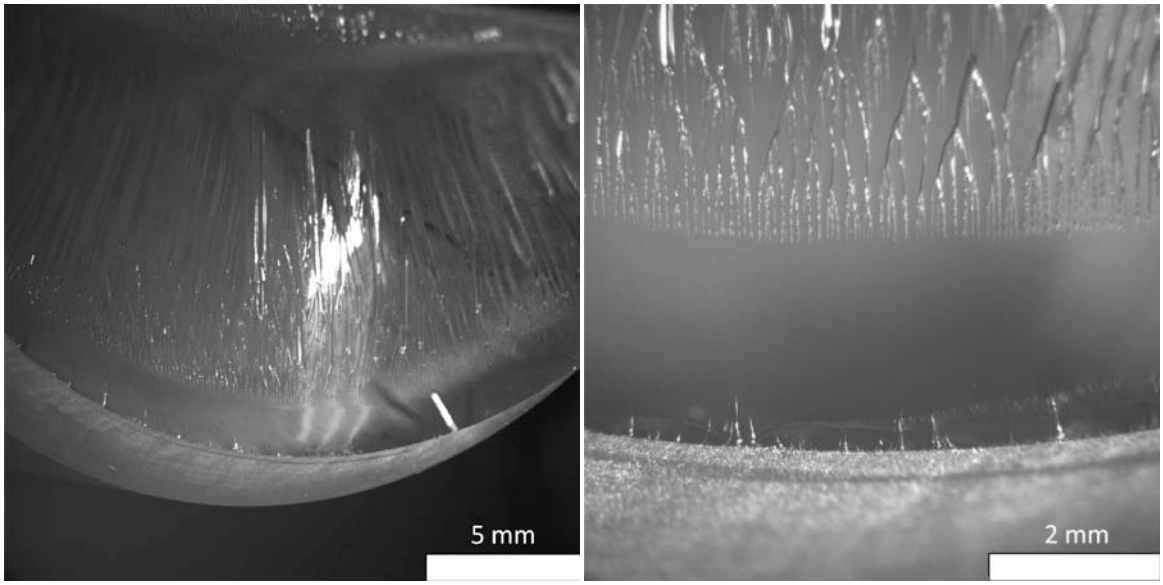

(a) (b)

Figure 49. Images showing the fracture surface of GB4-3.

For GB3-3 and GB4-3, the stiffness was also monitored using both a RVDT and a biaxial extensometer. From the RVDT data (Figure 50a and Figure 51a), fatigue cycle hardening was observed on GB3-3 and GB4-3, similar to that observed on GB3-2 (Figure 38a).

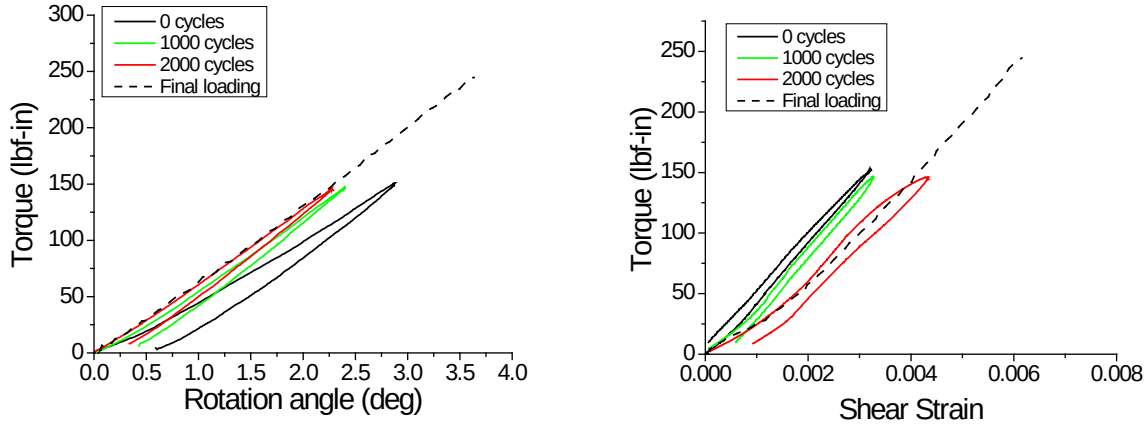

(a) (b)

Figure 50. Effect of fatigue on stiffness of sample GB3-3 as measured from (a) load cell and RVDT, and (b) load cell and biaxial extensometer.

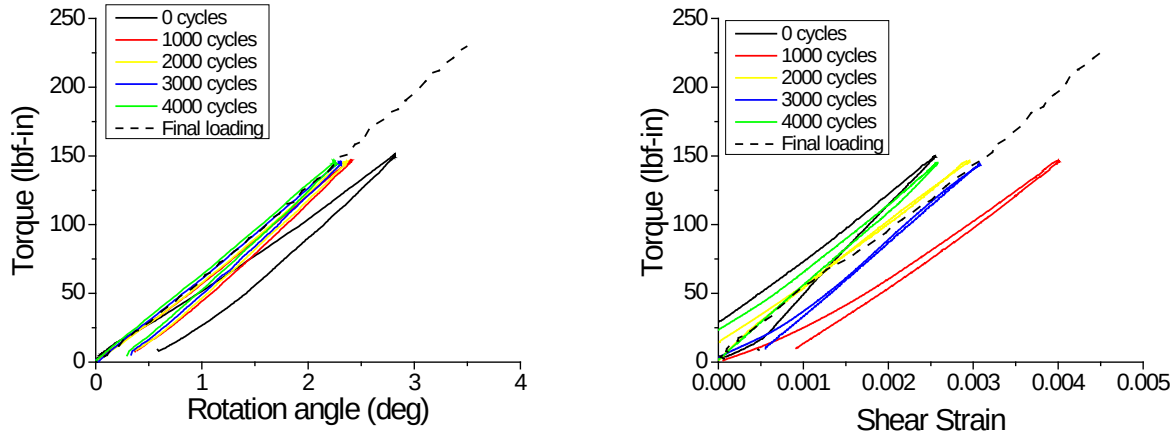

(a) (b)

Figure 51. Effect of fatigue on stiffness of sample GB4-3 as measured from (a) load cell and RVDT, and (b) load cell and biaxial extensometer.

The extensometer data indicated a stiffness drop in GB3-3 (Figure 51b) probably due to crack growth similar to that of GB3-2 (Figure 38b). However, for GB4-3 the stiffness initially decreased for up to 3000 cycles and then increased after an additional 1000 cycles (Figure 50b). The reason for this behavior is not clear, and requires further

investigation. One possible explanation may be related to the competition between the strain hardening and the “crack” softening occurring simultaneously in the grooved region.

Sample GB3-7 was fatigued between 20 and 200 lbf-in for 9000 cycles, which was the same condition used for GB4-6. However, the fracture torque of GB3-7 was much higher than GB4-6, i.e. 618 lbf-in vs. 281 lbf-in. GB3-7 was fabricated by the same machine shop that also processed GB3-8 and GB3-9. The notch roots of these three samples were very blunt. Thus, the fatigue test performed on GB3-7 did not seem to create any pre-crack, which was confirmed by the image of its fracture surface (Figure 52).

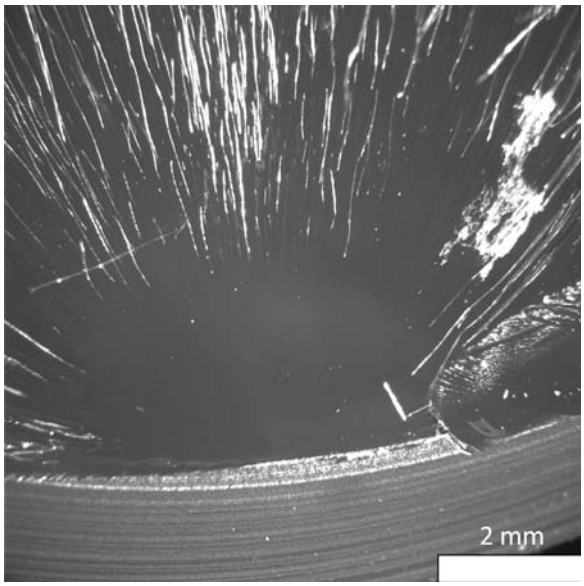

Figure 52. Images showing the fracture surface of GB3-7.

5. Finite Element Model Development for SNTT Epoxy Samples

The detailed SNTT geometry design concept and the associated finite element modeling are illustrated in Figs. 53-57. In order to ensure that the crack propagation direction is perpendicular, the local coordinate of the designed mesh needs to be perpendicular to both the spiral notch and central axis of the SNTT sample as illustrated in Figure 53. Furthermore, a proper partition of the SNTT model is also needed to generate properly organized mesh profiles that are aligned with the spiral crack front as shown by the yellow line in Fig. 54, where the red line indicates the first partition region.

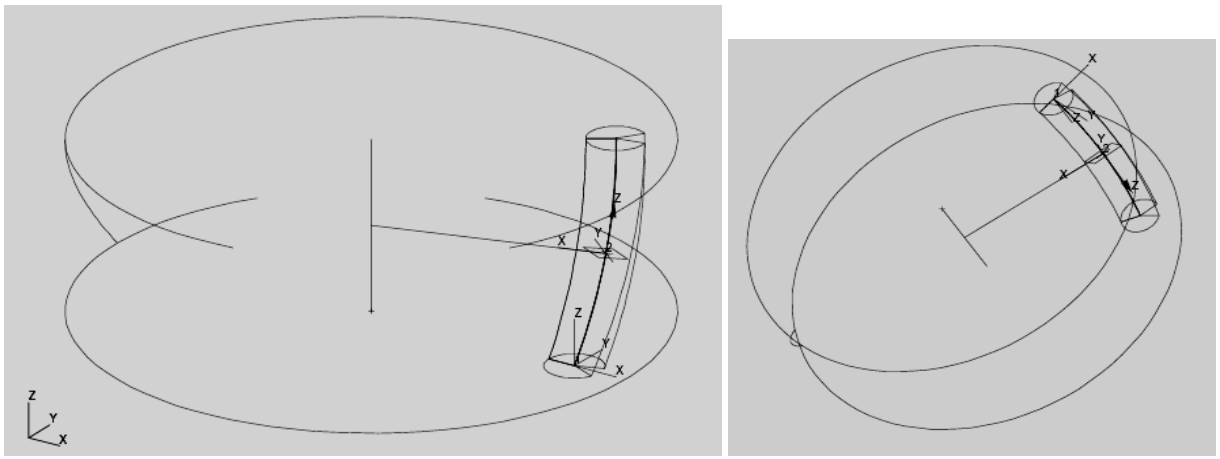

Figure 53. Schematic diagram of SNTT mesh design that allows the crack propagation to be perpendicular to the central axis of the SNTT samples.

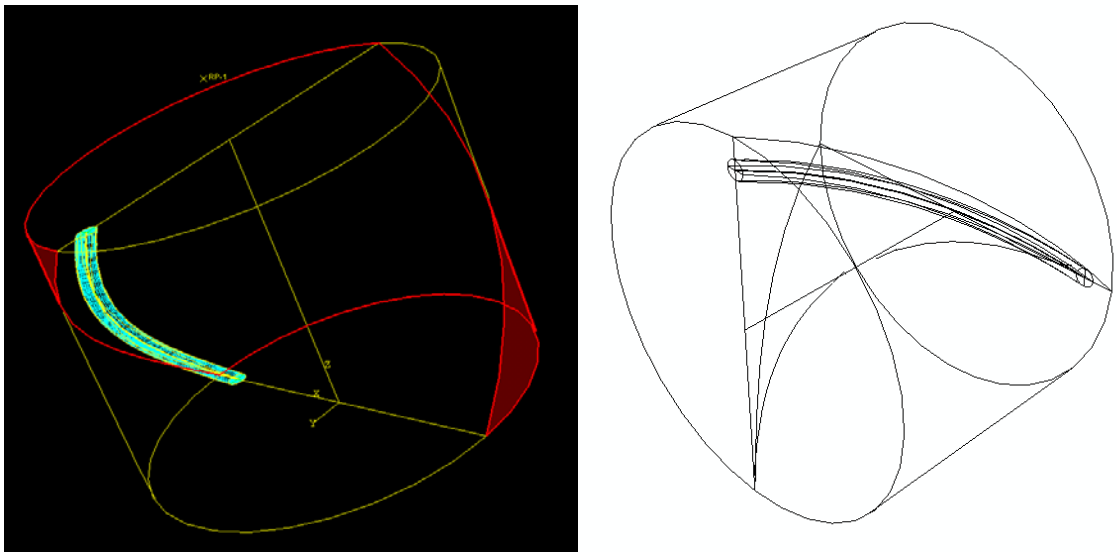

Figure 54. Schematic diagram of SNTT mesh design partition surfaces.

A more detailed mesh design with singular elements along the crack front is illustrated in Figure 55. The completed SNTT FEM model for the epoxy sample is shown in Figure 56 with the embedded partition surfaces. An enlarged view of the FEM model is shown in Figure 57, where the red line indicates the crack seam.

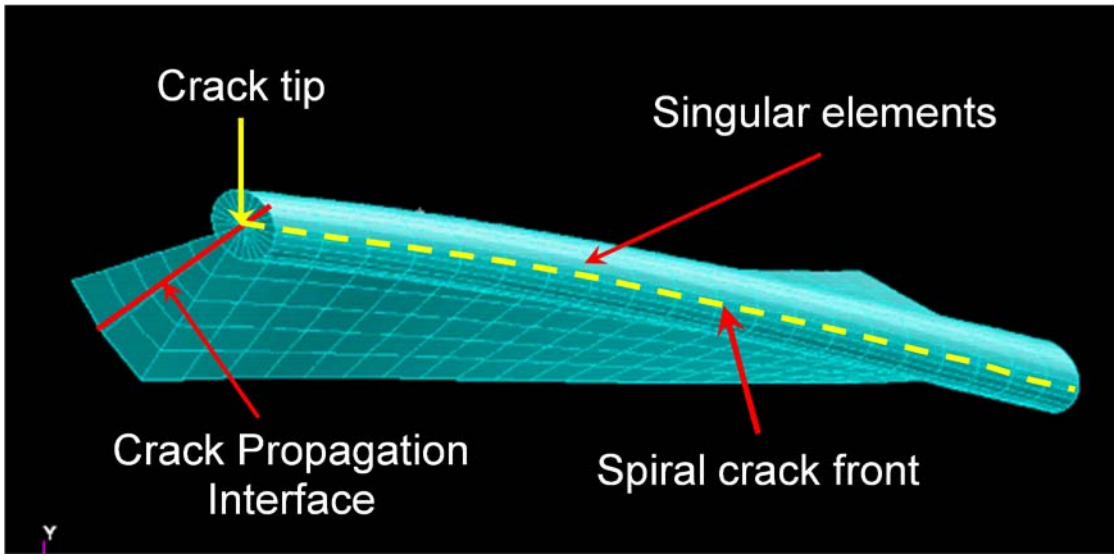

Figure 55. FEM mesh around crack front and crack tip, including the mesh boundary designed along the orientation of crack propagation.

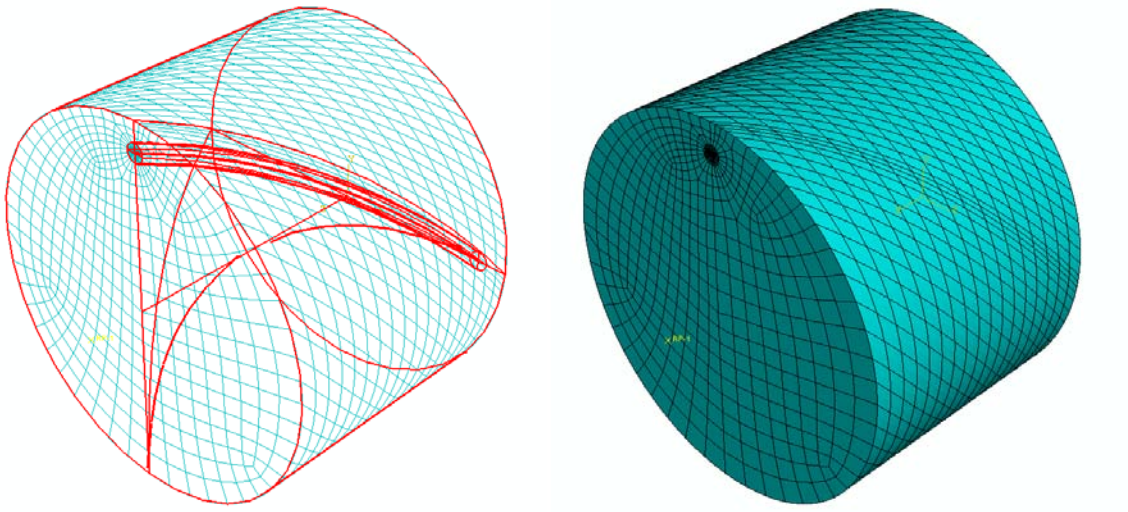

Figure 56. The FEM model designed for SNTT epoxy samples.

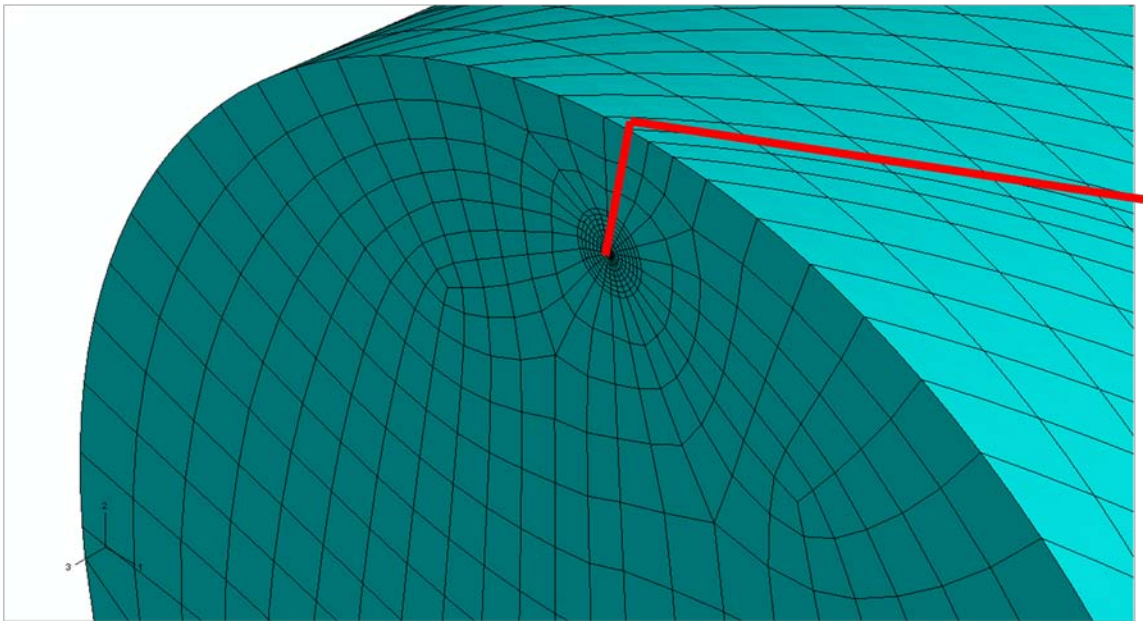

Figure 57. The enlarged view of FEM model for SNTT epoxy sample, where the red lines indicates the crack seam region.

6. Summary and future work

During FY2010, we have 1) configured a SNTT testing apparatus for polymeric/ composite samples; 2) fabricated more than 30 samples from two types of epoxy materials (Gougeon Brothers and MFG); and 3) obtained fundamental knowledge on the fracture behavior of these materials through three types of testing.

To date, a total number of 30 epoxy samples were studied using spiral notch torsion test. Nine samples were fractured without fatigue (Section 4.2), 14 samples were fatigue fractured (Section 4.3), and seven samples were fractured after being fatigued (Section 4.4). For all the tested samples, *brittle fracture* was observed. Thus, the fracture toughness of these materials can be estimated using linear elastic finite element analysis.

However, the sharpness of the notch root seems to affect the fracture behavior, particularly the fracture torque, which in turn would affect the calculated fracture toughness. Thus, fatigue is preferred in order to introduce sharp *pre-cracks* in these epoxy materials. An appropriate *fatigue protocol* has been established to achieve controllable crack growth using the SNTT setup, which is one of the significant accomplishments in this project.

Another important finding was that the epoxy samples involved in this study tended to fail in *tensile failure mode*. The fracture surfaces always follow the 45^{o} spiral plane that corresponded to Mode I loading; even when the starter notch's pitch angle was deviated from 45^{o}. This behavior also indicates the brittle fracture nature of epoxies.

On the other hand, this may not be the case for composite materials. Since fiber reinforced polymers can possess a large degree of anisotropy, their failures are expected to be sensitive to loading conditions. In the following quarter (Q1, FY2011), a significant effort will be focused on the effect of mixed-mode loading to the fracture of fiber glass composite materials. Since the fracture toughness of composites can be much higher than the unreinforced epoxies, proper pre-crack of SNTT composite samples will likely be needed. The experience of fatigue pre-cracking learned from epoxy polymeric materials will be beneficial when investigating polymeric composites.

The success of the fracture toughness evaluation of SNTT samples also depends on advanced finite element analysis. In the past year, geometric models designed for SNTT epoxy samples and appropriate meshing protocols were developed. In FY2011, extensive work will be performed on modeling based on the preliminary results achieved in FY2010. In addition, other factors that may affect fracture behavior of composite materials, such as loading rate and testing environments, will also be investigated. The achievements in FY2010 and the plans for FY2011 are highlighted in Table 5.

Table 5. Project progress in FY2010.

Task	Milestones	Progress, 2010				Notes
		Q1	Q2	Q3	Q4	
1	Sample design		100%			Completed
2	Equipment preparation		100%			Completed
3	Proof of concept: polymeric materials			100%		Completed
4	Mixed mode study of polymeric materials				100%	Completed
5	Proof of concept: composite materials				25%	In progress, will extend to FY11 Q1
		Progress, 2011				
		Q1	Q2	Q3	Q4	
5	Proof of concept: composite materials	25%				Extended from FY10
6	Mixed mode study of composite materials		0%			
7	Loading rate effect			0%		
8	Environmental effect			0%		

References

[Adams 1992] Adams, D. F. and E. M. Odom (1992). "Tensile and Shear Fatigue Testing of Brittle Polymers." *Sampe Quarterly-Society for the Advancement of Material and Process Engineering* **23**(2): 29-37.

[Araki 2002] Araki, W., T. Adachi, A. Yamaji and M. Gamou (2002). "Fracture toughness of bisphenol A-type epoxy resin." *Journal of Applied Polymer Science* **86**(9): 2266-2271.

[Cherry 1981] Cherry, B. W. and K. W. Thomson (1981). "THE FRACTURE OF HIGHLY CROSSLINKED POLYMERS .2. FRACTOGRAPHY." *Journal of Materials Science* **16**(7): 1925-1934.

[Hayman 2008] Hayman, B., J. Wedel-Heinen and P. Brondsted (2008). "Materials challenges in present and future wind energy." *Mrs Bulletin* **33**(4): 343-353.

[Kelly 2000] Kelly, A. and C. Zweben, Eds. (2000). Comprehensive Composite Materials. Amsterdam, Elsevier/Pergamon.

[Kensche 2006] Kensche, C. W. (2006). "Fatigue of composites for wind turbines." *International Journal of Fatigue* **28**(10): 1363-1374.

[Li 1996] Li, H. X., R. H. Jones, J. P. Hirth and D. S. Gelles (1996). "Fracture toughness of the F-82H steel-effect of loading modes, hydrogen, and temperature." *Journal of Nuclear Materials* **237**: 258-263.

[Nagasawa 1995] Nagasawa, M., H. Kinuhata, H. Koizuka, K. Miyamoto, T. Tanaka, H. Kishimoto and T. Koike (1995). "Mechanical Fatigue of Epoxy-Resin." *Journal of Materials Science* **30**(5): 1266-1272.

[Owen 1975] Owen, M. J. and R. G. Rose (1975). "FRACTOGRAPHY OF POLYESTER RESINS." *Journal of Materials Science* **10**(10): 1711-1718.

[Phillips 1978] Phillips, D. C., J. M. Scott and M. Jones (1978). "CRACK-PROPAGATION IN AN AMINE-CURED EPOXIDE-RESIN." *Journal of Materials Science* **13**(2): 311-322.

[Quinn 2007] Quinn, G. D. (2007). *Fractography of Ceramics and Glasses*. Natl. Inst. Stand. Techno, Gaithersburg, MD, USA.

[Sih 1974] Sih, G. C., “Strain Energy Density Factor Applied to Mixed Mode Crack Problem,” *International Journal of Fracture*, 1974, Vol. 10, pp. 305-321.

[Tao 2007] Tao, G. and Z. H. Xia (2007). "An experimental study of uniaxial fatigue behavior of an epoxy resin by a new noncontact real-time strain measurement and control system." *Polymer Engineering and Science* **47**(6): 780-788.

[Wang 2000] Wang, J. A., K. C. Liu, D. E. McCabe and S. A. David (2000). "Using torsional bar testing to determine fracture toughness." *Fatigue & Fracture of Engineering Materials & Structures* **23**(11): 917-927.

[Wang 2002a] Wang, J.-A. and K. C. Liu (2002). ORNL Spiral-Notch Torsion Test (SNTT) System. *2002 R&D 100 Award*, R&D Magazine.

[Wang 2002b] J. A. Wang, K. C. Liu, and D. E. McCabe, "An Innovative Technique for Measuring Fracture Toughness of Metallic and Ceramic Materials," *Fatigue and Fracture Mechanics: 33rd Volume*, ASTM STP 1417, W. G. Reuter and R. S. Piascik, Eds., pp. 757-770, December 2002

[Wang 2003a] Wang, J. A. and K. C. Liu (2003). "Fracture toughness determination using spiral-grooved cylindrical specimen and pure torsional loading." **US Patent 6588283**.

[Wang 2003b] Wang, J. A., K. C. Liu and D. E. McCabe (2003). "An innovative technique for measuring fracture toughness of metallic and ceramic materials." *Fatigue and Fracture Mechanics: 33rd Volume* **1417**: 757-770.

[Wang 2006] Wang, J. A. J., I. G. Wright, M. J. Lance and K. C. Liu (2006). "A new approach for evaluating thin film interface fracture toughness." *Materials Science and Engineering a-Structural Materials Properties Microstructure and Processing* **426**(1-2): 332-345.

[Wang 2008] Wang, J. A. J. and K. C. Liu (2008). "An innovative technique for evaluating fracture toughness of graphite materials." *Journal of Nuclear Materials* **381**(1-2): 177-184.

[Wang, H. 2002] Wang, H., L. Jiang, Y. H. He, L. J. Chen, P. K. Liaw, R. R. Seeley and D. L. Klarstrom (2002). "Infrared imaging during low-cycle fatigue of HR-120 alloy." *Metallurgical and Materials Transactions a-Physical Metallurgy and Materials Science* **33**(4): 1287-1292.

[Yamini 1979] Yamini, S. and R. J. Young (1979). "Crack-Propagation in and Fractography of Epoxy-Resins." *Journal of Materials Science* **14**(7): 1609-1618.

[Yamini 1980] Yamini, S. and R. J. Young (1980). "The Mechanical-Properties of Epoxy-Resins .2. Effect of Plastic-Deformation Upon Crack-Propagation." *Journal of Materials Science* **15**(7): 1823-1831.

Appendix A: SNTT Testing Log

Sample ID: GB1-1			
Material: 117LV/229			
Geometry: 4” gage length, 1” diameter, 36^{o} pitch angle, 0.1” groove depth (nominal)			
Date	Testing	Conditions	Results
03-24-2010	Fatigue	Angle control, 0.15^{o} – 2.71^{o}, 2 Hz, 100000 cycles	No significant cracking observed. Torque range changed from (47, 143) to (36, 133) in-lbf.
03-25-2010	Fatigue	Torque control, 40 – 160 in-lbf, 1 Hz, 11567 cycles	No significant cracking observed. Angle range changed from (0.89, 2.46) to (0.95, 2.50) degree.
03-25-2010	Fatigue	Angle control, 2.46^{o} – 3.20^{o}, 1 Hz, 4000 cycles	No significant cracking observed. Torque range changed from (141, 197) to (134, 194) in-lbf.
03-25-2010	Fatigue	Angle control, 2.46^{o} – 3.20^{o}, 2 Hz, 22482 cycles	No significant cracking observed. Torque range changed from (134, 194) to (130, 190) in-lbf.
03-25-2010 to 03-26-2010	Fatigue	Angle control, 4.49^{o} – 5.10^{o}, 2 Hz, 100000 cycles	No significant cracking observed. Torque range changed from (272, 321) to (238, 288) in-lbf.
03-26-2010	Fatigue	Angle control, 6.70^{o} – 7.20^{o}, 2 Hz, 32800 cycles	No significant cracking observed. Torque range changed from (378, 420) to (360, 402) in-lbf.
03-26-2010 to 03-28-2010	Fatigue	Angle control, 6.428^{o} – 7.202^{o}, 2 Hz, 286072 cycles	No significant cracking observed. Torque range changed from (367, 430) to (287, 353) in-lbf.
03-08-2010	Monotonic	Manually increased angle	Sample fractured at 801 lbf (17.85^{o})

Sample ID: GB1-2			
Material: 117LV/229			
Geometry: 4” gage length, 1” diameter, 36^{o} pitch angle, 0.1” groove depth (nominal)			
Date	Testing	Conditions	Results
03-29-2010	Fatigue	Angle control, 5.17^{o} – 6.43^{o}, 1 Hz, 100000 cycles	No significant cracking observed. Torque range changed from (298, 400) to (220, 323) in-lbf.
03-30-2010	Fatigue	Torque control, 350 – 450 in-lbf, 1 Hz, 3000 cycles	No significant cracking observed. Angle range changed from (6.63, 7.86) to (6.72, 7.98) degree.
03-30-2010 to 03-31-2010	Fatigue	Angle control, 7.50^{o} – 8.75^{o}, 2 Hz	Initial torque range (397, 501). Fractured at 500 in-lbf; final cycle number unrecorded.

Sample ID: GB1-3			
Material: 117LV/229			
Geometry: 4” gage length, 1” diameter, 36^{o} pitch angle, 0.1” groove depth (nominal)			
Date	Testing	Conditions	Results
03-31-2010 to 04-02-2010	Fatigue	Torque control, 150 – 200 in-lbf, 1 Hz, 70000 cycles	No significant cracking observed. Angle range changed from (2.544, 3.118) to (2.700, 3.316) degree.
04-12-2010 to 04-14-2010	Fatigue	Torque control, 200 – 250 in-lbf, 1 Hz, 90000 cycles	No significant cracking observed. Angle range changed from (3.478, 4.078) to (5.858, 6.435) degree.
04-20-2010	Fatigue	Torque control, 250 – 300 in-lbf, 1 Hz, 50000 cycles	No significant cracking observed. Angle range changed from (4.397, 5.020) to (5.012, 5.592) degree.
04-21-2010	Fatigue	Torque control, 350 – 400 in-lbf, 1 Hz, 30000 cycles	No significant cracking observed. Angle range changed from (6.276, 6.862) to (6.845, 7.424) degree.
04-21-2010 to 04-22-2010	Fatigue	Torque control, 400 – 450 in-lbf, 1 Hz, 100000 cycles	No significant cracking observed. Angle range changed from (7.491, 8.070) to (8.103, 8.669) degree.
04-22-2010	Fatigue	Torque control, 500 – 550 in-lbf, 2 Hz, 50000 cycles	No significant cracking observed. Angle range changed from (8.041, 8.633) to (8.934, 9.505) degree.
04-22-2010	Fatigue	Torque control, 600 – 650 in-lbf, 2 Hz, 50000 cycles	No significant cracking observed. Angle range changed from (10.263, 10.859) to (11.186, 11.758) degree.
04-22-2010	Fatigue	Angle control, 0.5^{o} – 6.1^{o}, 0.1 Hz, 1000 cycles; 0.4^{o} – 6.0^{o}, 2 Hz, 2700 cycles.	Initial torque range (2, 403) in-lbf. Fractured after 2700 cycles, fracture torque 435 in-lbf (6^{o}).

Sample ID: GB1-4			
Material: 117LV/229			
Geometry: 4” gage length, 1” diameter, 36^{o} pitch angle, 0.1” groove depth (nominal)			
Date	Testing	Conditions	Results
05-04-2010	Fatigue	Angle control, 1.2^{o} – 4.8^{o}, 1 Hz,	Torque range; Initial: 27 – 301 lbf-in 10k cycles: 15 – 294 lbf-in Sample fractured after 16164 cycles. Max torque: 304.3 lbf-in Max angle: 4.84^{o}

Sample ID: GB1-5			
Material: 117LV/229			
Geometry: 4” gage length, 1” diameter, 36^{o} pitch angle, 0.1” groove depth (nominal)			
Date	Testing	Conditions	Results
05-04-2010	Fatigue	Torque control, 20 – 200 in-lbf, 1 Hz, 50000 cycles	No significant cracking observed. Angle range changed from (0.68, 3.27) to (1.23, 3.82) degree.
05-05-2010	Fatigue	Torque control, 30 – 300 in-lbf, 1 Hz	Initial angle range (1.38, 4.86) degree. Fractured after 6316 cycles, at 302 in-lbf (5.17^{o}).

Sample ID: GB1-6			
Material: 117LV/229			
Geometry: 4” gage length, 1” diameter, 36^{o} pitch angle, 0.1” groove depth (nominal)			
Date	Testing	Conditions	Results
05-05-2010	Fatigue	Torque control, 30 – 300 in-lbf, 1 Hz, 5500 cycles	Angle range changed from (1.2, 4.88) to (1.45, 5.38) degree.
05-05-2010	Monotonic	Torque increase from 10 in-lbf to 1200 in-lbf at 40 in-lbf/sec.	Fractured at 596 in-lbf (9.436^{o}).

Sample ID: GB1-7			
Material: 117LV/229			
Geometry: 4” gage length, 1” diameter, 36^{o} pitch angle, 0.1” groove depth (nominal)			
Date	Testing	Conditions	Results
05-07-2010	Fatigue	Torque control, 20 – 200 in-lbf, 1 Hz, 260000 cycles	Angle range changed from (0.67, 3.24) to (1.70, 3.98) degree.
05-10-2010	Monotonic	Torque increase from zero to 1000 in-lbf at 40 in-lbf/sec.	Fractured at 357 in-lbf (5.868^{o}).

Sample ID: GB2-1			
Material: 117LV/XH10B			
Geometry: 4” gage length, 1” diameter, 36^{o} pitch angle, 0.1” groove depth (nominal)			
Date	Testing	Conditions	Results
05-10-2010	Monotonic	Torque increase from zero to 1000 in-lbf at 40 in-lbf/sec.	Fractured at 774 in-lbf (10.01^{o}).

Sample ID: GB2-2			
Material: 117LV/XH10B			
Geometry: 4” gage length, 1” diameter, 36^{o} pitch angle, 0.1” groove depth (nominal)			
Date	Testing	Conditions	Results
05-10-2010	Fatigue	Torque control, 20 – 200 in-lbf, 1 Hz, 150000 cycles	Angle range changed from (-0.5, 1.74) to (0.32, 2.54) degree.
05-12-2010	Monotonic	Torque increase from zero to 1000 in-lbf at 40 in-lbf/sec.	Fractured at 865 in-lbf (13.83^{o}).

Sample ID: GB2-3			
Material: 117LV/XH10B			
Geometry: 4” gage length, 1” diameter, 28^{o} pitch angle, 0.2” groove depth (nominal), root sharpened with razor blade			
Date	Testing	Conditions	Results
05-12-2010	Fatigue	Torque control, 30 – 300 in-lbf, 2 Hz, ~ 100 cycles	Fractured at 289 in-lbf (4.95^{o}).

Sample ID: GB2-4			
Material: 117LV/XH10B			
Geometry: 4” gage length, 1” diameter, 28^{o} pitch angle, 0.2” groove depth (nominal), root sharpened with razor blade			
Date	Testing	Conditions	Results
05-12-2010	Fatigue	Torque control, 30 – 300 in-lbf, 1 Hz, 1660 cycles	Fractured at 303 in-lbf (5.22^{o}).

Sample ID: GB2-5			
Material: 117LV/XH10B			
Geometry: 4” gage length, 1” diameter, 20^{o} pitch angle, 0.3” groove depth (nominal), root sharpened with razor blade			
Date	Testing	Conditions	Results
05-12-2010	Fatigue	Torque control, 10 – 100 in-lbf, 1 Hz, 60,000 cycles	No detectable crack
05-13-2010 to 05-20-2010	Fatigue	Torque control, 10 – 100 in-lbf, 2 Hz, 1,200,000 cycles	No detectable crack
?	Fatigue	Torque control, 10 – 100 in-lbf, 2 Hz, 694,760 cycles	
05-20-2010 to 05-26-2010	Fatigue	Torque control, 10 – 100 in-lbf, 2 Hz, 1,054,223 cycles	No detectable crack
05-26-2010	Fatigue	Torque control, 15 – 150 in-lbf, 1 Hz, 41795 cycles	Fractured at 153.8 in-lbf (4.634 deg)

Sample ID: GB2-6			
Material: 117LV/XH10B			
Geometry: 4” gage length, 1” diameter, 20^{o} pitch angle, 0.3” groove depth (nominal)			
Date	Testing	Conditions	Results
05-07-2010	Monotonic	Torque increase from 10 in-lbf to 1200 in-lbf at 40 in-lbf/sec.	Fractured at 447 in-lbf (6.37^{o}).

Sample ID: GB3-1			
Material: 117LV/229			
Geometry: 4” gage length, 1” diameter, 0.125” groove depth			
Date	Testing	Conditions	Results
07-21-2010	monotonic	40 lbf-in/sec to 1000 lbf	Fractured at 338 lbf-in

Sample ID: GB3-2			
Material: 117LV/229			
Geometry: 4” gage length, 1” diameter, 0.122” groove depth			
Date	Testing	Conditions	Results
07-27-2010	Fatigue	20 -200 lbf-in, 1Hz	Fractured after 5139 cycles at 198 lbf-in

Sample ID: GB3-3			
Material: 117LV/229			
Geometry: 4” gage length, 1” diameter, 0.122” groove depth			
Date	Testing	Conditions	Results
07-28-2010	Fatigue	20 -200 lbf-in, 1Hz	Fatigued for 3000 cycles
07-28-2010	Mono	40 lbf-in/sec to 1000 lbf	Fractured at 244 lbf-in

Sample ID: Batch3-4			
Material: 117LV/229			
Geometry: 4” gage length, 1” diameter, 0.077” groove depth			
Date	Testing	Conditions	Results
06-30-2010	Fatigue	30 -300 lbf-in, 1Hz	Fractured after 3368 cycles @ 297 lbf-in.

Sample ID: Batch 3-5			
Material: 117LV/229			
Geometry: 4” gage length, 1” diameter, 0.091” groove depth			
Date	Testing	Conditions	Results
07-01-2010	Fatigue	30 -300 lbf-in, 1Hz	Fractured after 220 cycles @ 296.7 lbf-in.

Sample ID: Batch 3-6			
Material: 117LV/229			
Geometry: 4” gage length, 1” diameter, 0.090” groove depth			
Date	Testing	Conditions	Results
07-01-2010	monotonic	40 lbf-in/sec to 1000 lbf	Fractured at 384 lbf-in, 5.57^{o}

Sample ID: GB3-7			
Material: 117LV/229			
Geometry: 4” gage length, 1” diameter, 0.102” groove depth			
Date	Testing	Conditions	Results
07-30-2010	Fatigue	20 -200 lbf-in, 1Hz	Fatigued for 9000 cycles
07-30-2010	Mono	40 lbf-in/sec to 500 lbf	Did not fracture
Groove root sharpened with a razor blade			
07-30-2010	Mono	40 lbf-in/sec to 1000 lbf	Fractured at 618 lbf-in

Sample ID: GB3-8			
Material: 117LV/229			
Geometry: 4” gage length, 1” diameter, 0.206” groove depth			
Date	Testing	Conditions	Results
Groove root sharpened with a razor blade			
07-30-2010	Mono	40 lbf-in/sec to 1000 lbf	Fractured at 343 lbf-in

Sample ID: GB3-9			
Material: 117LV/229			
Geometry: 4” gage length, 1” diameter, 0.298” groove depth			
Date	Testing	Conditions	Results
Groove root NOT sharpened			
07-30-2010	Mono	40 lbf-in/sec to 1000 lbf	Fractured at 430 lbf-in

Sample ID: GB4-1			
Material: 117LV/229			
Geometry: 4” gage length, 1” diameter, 0.128” groove depth			
Date	Testing	Conditions	Results
07-21-2010	monotonic	40 lbf-in/sec to 1000 lbf	Fractured at 305 lbf-in

Sample ID: GB4-2			
Material: 117LV/229			
Geometry: 4” gage length, 1” diameter, 0.127” groove depth			
Date	Testing	Conditions	Results
07-28-2010	Fatigue	20 – 200 lbf-in	Fractured after 3308 cycles at 197 lbf-in

Sample ID: GB4-3			
Material: 117LV/229			
Geometry: 4” gage length, 1” diameter, 0.124” groove depth			
Date	Testing	Conditions	Results
07-27-2010	Fatigue	20 – 200 lbf-in	Fatigued for 4000 cycles
07-27-2010	Mono	40 lbf-in/sec to 1000 lbf	Fractured at 235 lbf-in

Sample ID: GB4-4			
Material: 117LV/229			
Geometry: 4” gage length, 1” diameter, 0.092” groove depth			
Date	Testing	Conditions	Results
07-21-2010	monotonic	40 lbf-in/sec to 1000 lbf	Fractured at 404 lbf-in

Sample ID: GB4-5			
Material: 117LV/229			
Geometry: 4” gage length, 1” diameter, 0.106” groove depth			
Date	Testing	Conditions	Results
07-29-2010	Fatigue	20 – 200 lbf-in	Fatigued for 10000 cycles
07-29-2010	Fatigue	25 – 250 lbf-in	Fractured after 80 cycles at 240 lbf-in

Sample ID: GB4-6			
Material: 117LV/229			
Geometry: 4” gage length, 1” diameter, 0.107” groove depth			
Date	Testing	Conditions	Results
07-29-2010	Fatigue	20 – 200 lbf-in	Fatigued for 9000 cycles
07-29-2010	Mono	40 lbf-in/sec to 1000 lbf	Fractured at 281 lbf-in

Sample ID: MFG-1			
Material: RIM135/RIMH1366			
Geometry: 4” gage length, 1” diameter, 0.084” groove depth			
Date	Testing	Conditions	Results
07-21-2010	monotonic	40 lbf-in/sec to 2000 lbf	Fractured at 1013 lbf-in

Sample ID: MFG-2			
Material: RIM135/RIMH1366			
Geometry: 4” gage length, 1” diameter, 0.078” groove depth			
Date	Testing	Conditions	Results
07-21-2010	Fatigue	60 – 600 lbf-in (testing machine did not response fast enough for this range of torque)	Fractured after ~ 500 cycles at 558 lbf-in

Sample ID: MFG-3			
Material: RIM135/RIMH1366			
Geometry: 4” gage length, 1” diameter, 0.081” groove depth			
Date	Testing	Conditions	Results
08-16-2010	Fatigue	30 – 300 lbf-in, 1Hz	Fractured after 7084 cycles at 294 lbf-in

APPENDIX B: DOE Wind Turbine Blade Integrity Project FY11 Q1 Progress Report

ORNL/TM-2010/333

Materials and Technology Division
Oak Ridge National Laboratory

An Innovative Technique for Evaluating the Integrity and Durability of Wind Turbine Blade Composites

FY11 Q1 Progress Report

Jy-An John Wang and Fei Ren
Materials Science and Technology Division,
Oak Ridge National Laboratory, Oak Ridge, TN, 37831

And

John Mandell and Pancasatya Agastra
Montana State University, Bozeman, MT 59717

Date Published: Dec. 2010

Prepared by
OAK RIDGE NATIONAL LABORATORY
Oak Ridge, Tennessee 37831-6283
Managed by
UT-BATTELLE, LLC
For the
U.S. DEPARTMENT OF ENERGY
under contract DE-AC05-00OR22725

ACKNOWLEDGEMENTS

This research was sponsored by the Wind Energy Program of Department of Energy and was carried out at Oak Ridge National Laboratory under contract DE-AC05-00OR22725 with UT-Battelle, LLC. The authors are grateful to Mr. Stanton Hadley and Dr. Brennan Smith for their support of this project. The authors would like to thank Dr. Paul Majsztrik of ORNL for his comments and suggestions after reviewing this report.

Table of Contents

List of figures

List of tables

Executive summary

The aim of this project is to examine the fracture behavior of polymeric composite materials relative to wind turbine blades using spiral notch torsion test (SNTT). In addition to experimental design and equipment preparation, the Phase I project (FY2010) had focused on SNTT testing of epoxies – an important matrix material for composites. The objective of the Phase II project in FY2011 is to investigate epoxy-based composite materials, including sample design, SNTT testing, and data analysis by fractography and finite element modeling.

This report describes the outcome of discussions between the ORNL team (Drs. John Jy-An Wang and Fei Ren) and Prof. Mandell's group of Montana State University (MSU) on September 6, 2010, and subsequent experimentation intended to establish an SNTT based sample for composite materials testing. Experimental methods and approaches to the problem are described in detail in the Appendix. This phase of the work has focused on the sample geometry in which a composite is fabricated into a groove in a tubular epoxy sample; other geometries have been pursued in less detail. Methodology for casting good quality epoxy tubes has been established. In addition, a new methodology of infusing composites into epoxy samples has been successfully demonstrated by infusing high quality unidirectional composite into grooves machined in a flat cast epoxy plate.

1. Introduction

The aim of this project is to examine the fracture behavior of polymeric composite materials relative to wind turbine blades using spiral notch torsion test (SNTT). In addition to experimental design and equipment preparation, the Phase I project (FY2010) had focused on SNTT testing of epoxies – an important matrix material for composites. The objective of the Phase II project in FY2011 is to investigate epoxy-based composite materials, including sample design, SNTT testing, and data analysis by fractography and finite element modeling.

The Phase II project started with a meeting on September 6, 2010 where the SNTT method was described, and adaptations for fracture testing of composite materials explored. The primary proposed geometry was an epoxy tube containing a band of unidirectional composite embedded at an angled along the surface (Figure 1). The original concept of a band composed of part composite and part neat resin was modified to that of a band of uniform unidirectional composite at a fiber volume fraction typical of wind turbine blades, around 60%. Cracks would then be expected to grow parallel to the fibers under axial/torsional loading. Other options included an exterior pre-cured band bonded to the surface and a crack starter feature, all in the same general geometry. Other possible geometries included a resin-composite-resin sandwich and an all-composite tube. Experimentation which followed explored the fabrication of potential geometries.

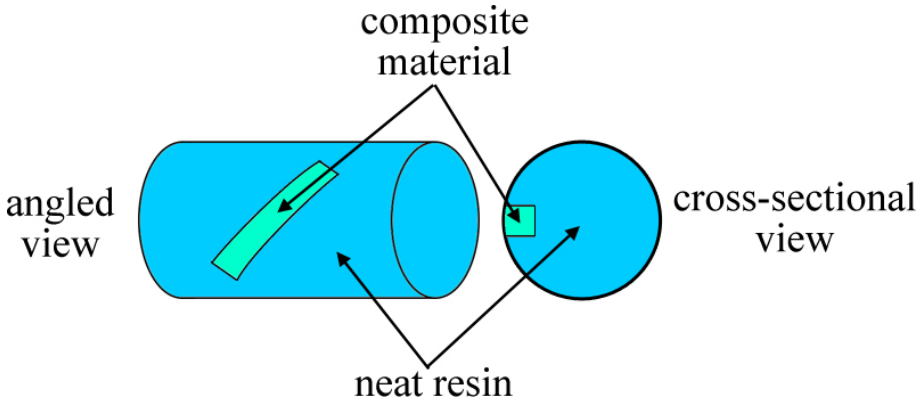

Figure 1. SNTT specimen with angled unidirectional composite band.

2. SNTT sample fabrication

Two approaches for the composite SNTT specimen were discussed:

1. Infusion of embedded strand in a groove in the neat resin specimen (Figure 1). The preliminary approach was using a flat neat resin specimen, in which the strand is placed in a machined groove and infused with resin using a vacuum

bag technique. This preliminary work ensured the feasibility of infusing the strand in a grooved SNTT test specimen.

In conjunction with exploring the feasibility of infusing an SNTT specimen, a neat resin SNTT test specimen manufacturing technique was also explored using a mold supplied by ORNL. Two kinds of neat resin specimen, with and without fabric on the perimeter of the gage section, were also explored.

2. Co-cured resin-composite-resin sandwich as shown in Figure 2. SNTT specimen would be machined out of a co-cured sandwich laminate in several different orientations.

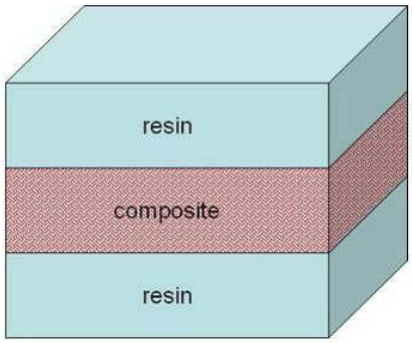

Figure 2. Schematic of the resin-composite-resin sandwich structure

*2.1 **Embedded strand***

2.1.1 Flat neat-resin laminate

The neat resin was fabricated using two parallel 1/2" glass plates with a 1/8"-thick acrylic spacer, tacky tape (Airtech AT-200Y sealant) around the perimeter. Several C-clamps were used to hold the assembly in position. Neat resin mixtures Hexion Epikote RIMR 135 and Hexion Epikure RIMH1366 were mixed for 5 minutes using a mixer with a Jiffy impeller in a polyethylene beaker, degassed at full vacuum for ~10 minutes or until boiling was apparent and then poured carefully into the mold cavity with a funnel and a 3/8"-OD polyethylene tube extension (Figure 3). Pouring was done carefully to prevent bubble entrainment into the neat resin laminate. After pouring, the resin was cured at room temperature overnight and the whole apparatus was post-cured in a convection oven at 100°C for 4 hours. For the second and third trials, the post cure schedules were changed to 50°C and 70°C for 8 hours, respectively. A funnel with a smaller outlet opening was used to reduce the flow rate into the mold. The mold materials are summarized in Table 1. The mold setup is illustrated in Figure 4.

Figure 3. Weighing, mixing and degassing of resin mix.

Table 1. Molding materials.

Mold	Glass, 30 cm × 30 cm × 12.7 mm
Mold Release	Loctite Frekote 44-NC Mold Release Agent
Tacky Tape	Airtech AT-200Y
Resin	Hexion Epikote RIMR 135/Epikure RIMH 1366
Spacer	Acrylic, 1”×1”×0.25”

Figure 4. Parallel glass-plate mold for the flat neat-resin laminate

The de-molded resin laminate was then cut in two and a groove was machined lengthwise using a 1/8” diameter diamond coated end mill. The groove width was also 1/8” and at a depth calculated to obtain the desired fiber volume content. The machining process is shown in Figure 5. The milling feed rate was 8”/10 min with a spindle speed of 1600 rpm. Once machining was done, two and four strands of PPG TEX2400 were placed in the grooves to get approximate fiber volume contents of 36%

and 64%, respectively, and resin infused using a vacuum bag technique as shown in Figure 6 and Figure 7. Nylon 6/6 sheet thickness of 1/16” was initially used and later changed to a thickness of 0.04”. Two attempts were done for each low and high fiber volume contents. For each fiber volume content, two different injection temperatures were used, room temperature and 50°C.

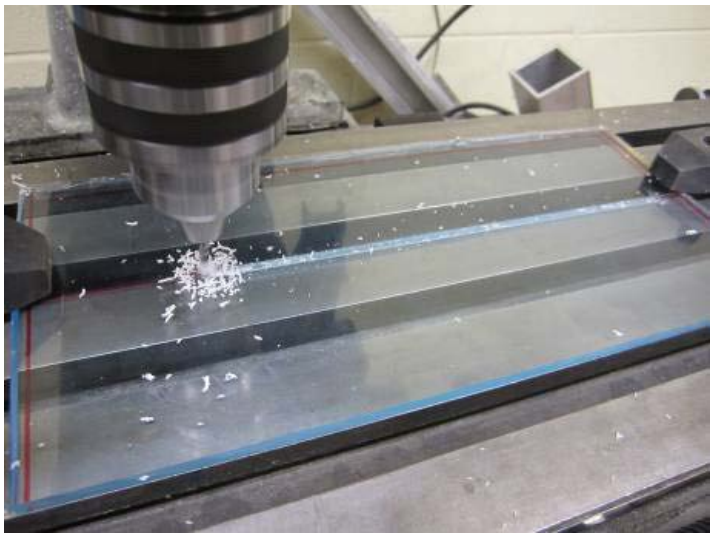

Figure 5. Machining of the groove

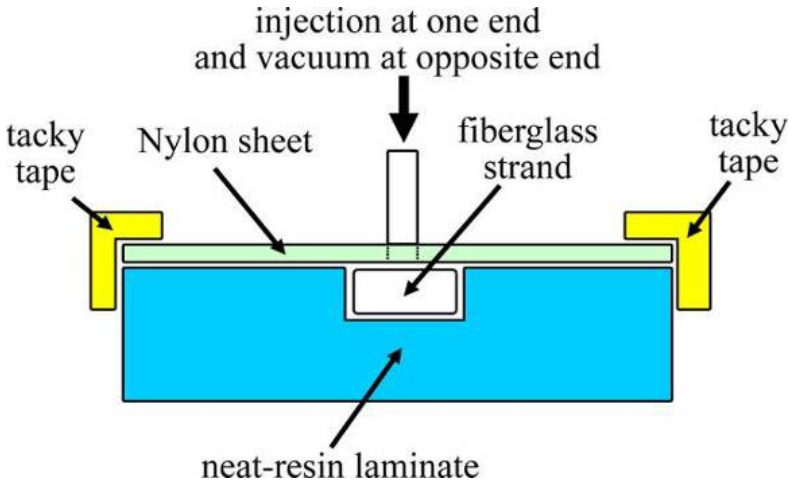

Figure 6. Groove infusion setup

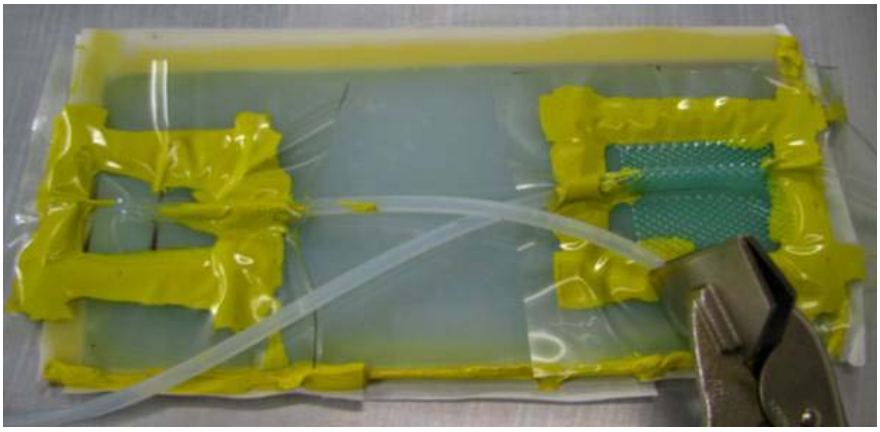

Figure 7. Groove infusion end of process

In the initial attempt, the post-curing temperature of 100°C for the neat resin laminate was too high, resulting in massive chipping of the glass mold and sticking resin on the glass surface that eventually broke apart the neat resin laminate as it was de-molded. For the second attempt, the same procedure was followed, except the post-cure temperature was lowered to 50°C for 8 hours. The result was a clear mold with minimum micro-bubble content, but the T_g of cured resin might have been too low, causing chipping during groove machining. For the third attempt, pouring using a funnel with a smaller hole produced a very clear laminate free of bubbles. Third attempt post-cure temperature at 70°C for 8 hours produced a clean edge during groove machining fiber placement in the groove result are shown in Figure 8.

For the first strand infusion at low fiber volume content, the flow rate was too high, resulting in a very porous composite in the groove. For the second attempt, a smaller tube was used and the flow rate was controlled using a sheet metal clamp. The resulting laminate was much better.

For the first strand infusion attempt at the high fiber volume, the resin flow rate was too slow, which was a consequence of the low permeability at high fiber volume. The infusion temperature was elevated to 50°C to soften the nylon sheet (to reduce flashing) and to decrease the resin viscosity, but the permeability was so low that the resin gelled before the groove was completely filled. For the second attempt, the temperature was kept at room temperature and the groove was completely filled in 2.5 hours. There was a small extent of porosity and flashing. The fiber volume content comparison is shown in Figure 9.

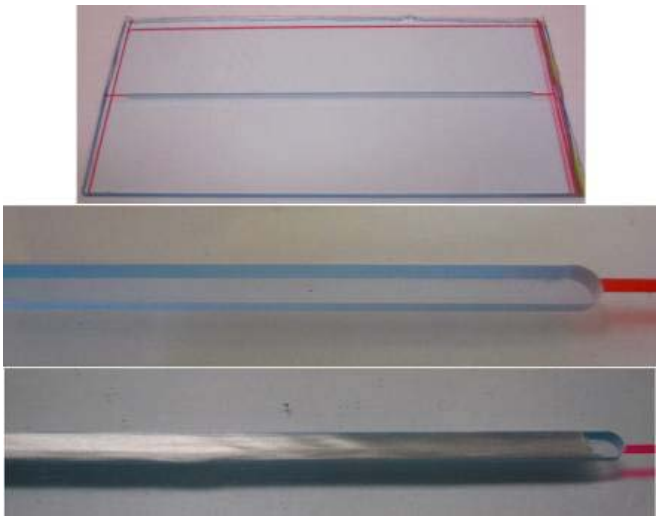

Figure 8. The machining result and fiber placement in the groove.

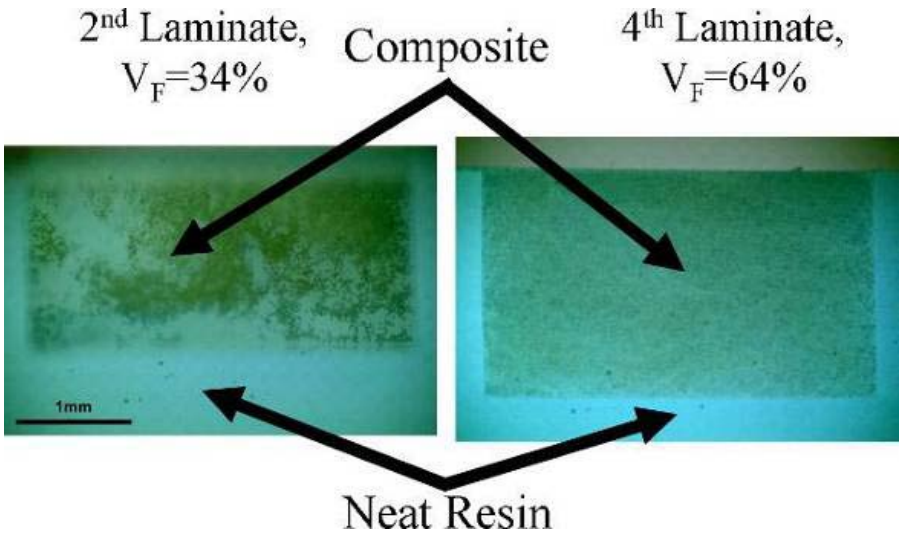

Figure 9. Infusion of the strands at two different fiber volume contents.

2.1.2 Infusion of strand in grooved SNTT specimen

The success of strand infusion in the grooved flat laminate would lead to strand infusion in the grooved SNTT specimen. This project is still ongoing. Similar but thinner nylon sheet would be wrapped around the SNTT specimen and sealed with the tacky tape as shown in Figure 10.

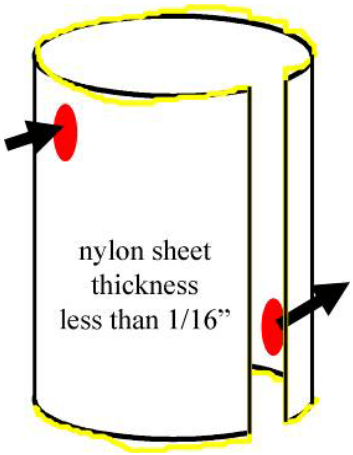

Figure 10. Strand infusion schematic for the grooved SNTT specimen.

2.1.3 Casting of cylindrical SNTT specimen

Casting of the neat resin SNTT test specimen was done with pouring instead of injection, because of the mold design limitation as shown in Figure 11. The mold was coated with mold release (see Table 1) according to the manufacturer's recommendation. The mold was sealed for all the possible sources of leak using tacky tape and vacuum pressure as shown in Figure 12. The mixed and degassed resin was poured into the SNTT mold using a funnel and a tube extending to the bottom of the mold to minimize bubble entrapment as shown in Figure 13. The same care was used when pouring as previously delineated for manufacturing the flat neat-resin test specimen.

Figure 11. Half of the mold with demolded neat resin.

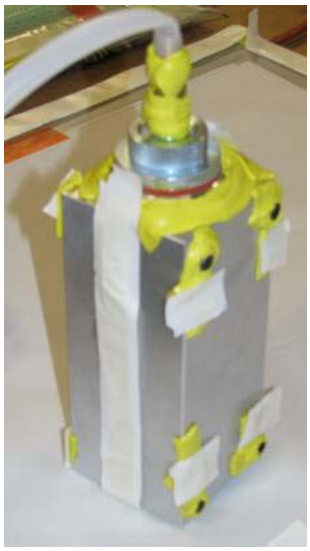

Figure 12. Sealing the mold to prevent leaks prior to pouring.

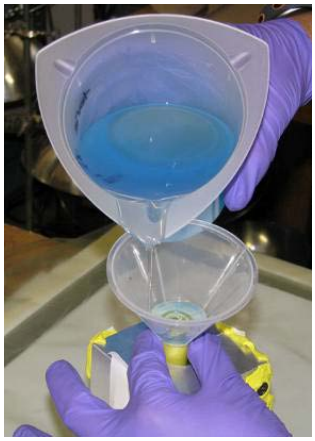

Figure 13. Careful pouring of the resin on the conical wall of the funnel.

Three different test specimens were made, one-third length, full length, and full length with tackified unidirectional fabric. The initial one-third length was to ensure that the neat resin would be easily de-molded, to ensure success of the full length specimen. For the full length with tackified fabric, shown in Figure 14, the fabric was cut to size and placed inside of each half of the mold. Another step of degassing was added prior to post-curing to remove trapped bubbles from the pouring process as shown in Figure 15. Finally the resin was post-cured in the oven at 100°C for 4 hours as shown in Figure 16.

Figure 14. A sample of tackified fabric.

Figure 15. Second degassing after pouring for SNTT with tackified fabric.

Figure 16. The resin-filled mold in a convection oven.

The one-third length SNTT neat resin casting was easily de-molded and the specimen was flawless (Figure 17a). The full SNTT test specimen was difficult to de-mold because of the different coefficient of thermal expansion between the resin and the aluminum mold and the geometry of the mold. The shrunken resin was stuck in the mold and had to be pried out of the mold. Voids were found near the bottom, under the vertical portion of the mold (horizontal surfaces when the mold is upright) (Figure 17b). Minimum flashing was formed at the location at the mold matting surfaces (Figure 17b). As a suggestion, the mold should be designed such that bubbles would not be trapped

in the mold, (e.g. larger radius fillet, termination of horizontal surfaces). For the SNTT with tackified fabric, extensive voids formed within the fabric inter-strand (Figure 17c), because of the second time degassing after pouring. The use of fabric in neat resin SNTT specimen manufacturing suggests that an infusion process is more suitable than pouring.

(a)

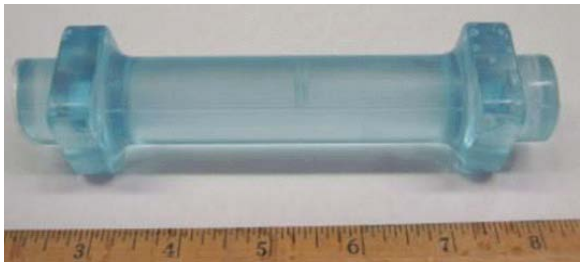

(b)

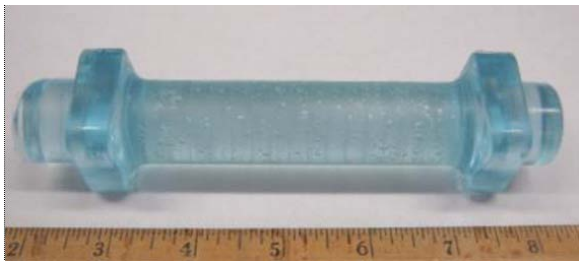

(c)

Figure 17. (a) One-third SNTT specimen; (b) Neat resin SNTT; (c) Neat resin SNTT with tackified fabric on the perimeter of the gage section.

2.2 Co-cured sandwich laminate

Three stacks of a specified number of layers of E-LT5500 fabric was cut into 6”×1.5” pieces and placed equidistance apart under a 0.5” glass plate as shown in Figure 18. The manufacturing technique included a vacuum bag with extra tortuous path entering the vent port. Two unsuccessful attempts were made to produce co-cured sandwich laminates: 1) 30 layers of precut fabric, off-centered in the mold with bottom injection and vent. 2) 15 layers of fabric precut, centered in the mold, bottom injection and top vent. A schematic of the setup and photograph of the actual setup are illustrated in Figure 18 and Figure 19, respectively.

The method to produce this sandwich laminate proved to be very difficult, because of the hollow space and combined with the thickness, the shape integrity could not be ensured with a vacuum bag sheet. The sandwich laminate should be manufactured in a cavity with solid walls and infused with a peristaltic pump, in case the vacuum pressure was not enough to suck the liquid, suggesting VARTM (vacuum assisted resin transfer molding) as an alternative method. The failed infusion processes on both attempts are shown in Figure 21 and Figure 22.

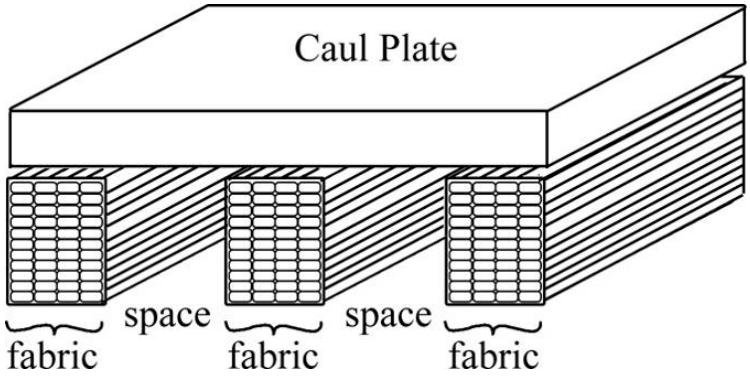

Figure 18. Schematic for sandwich test specimen between the vacuum bag material and the aluminum mold.

Figure 19. First attempt to manufacture sandwich test specimen.

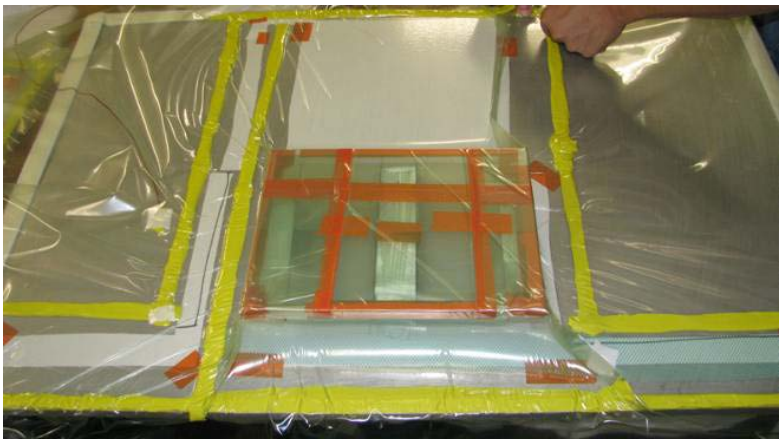

Figure 20. Second attempt to manufacture the sandwich specimen.

Figure 21. Failed first attempt of sandwich specimen.

Figure 22. Failed second attempt of sandwich specimen.

The failure of sandwich laminate manufacturing prompted the idea of machining SNTT test specimens from a thick composite laminate. Twenty layers of 10” × 31” E-LT5500 fabric would yield enough specimens. This thick laminate would be cut into smaller blocks and machined into SNTT test specimen. An example of MSU capability in manufacturing thick composite is shown in Figure 23 and Figure 24.

Figure 23. Infusion setup for 4”-thick composite laminate.

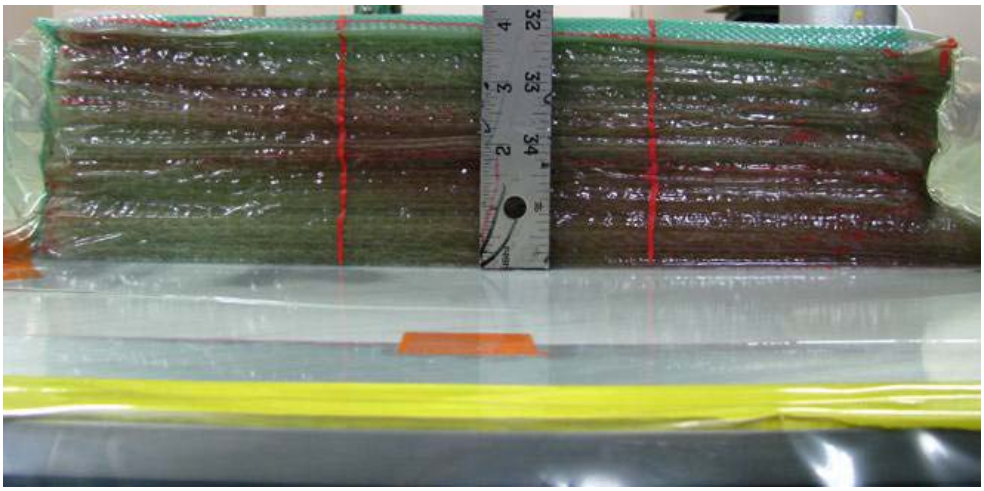

Figure 24. Completed infusion of a 4”-thick composite laminate.

3. Summary and recommendations

The casting of epoxy tubes following prescribed mixing and degassing procedures appears to be successful, although a few small pores remain. These might be eliminated by slight modifications to the mold which are suggested in the previous section. The next step was to demonstrate the successful infusion of the composite band. To simplify the initial attempts, the band was infused in a machined groove in a

flat epoxy plate. After several attempts, a good quality band was infused in the groove, with the desired fiber content range. Tensile specimens loaded normal to the band are scheduled to explore the failure mode.

Other attempts at molding specimens were less successful. Adding a (tackified) fiber band before casting the tubes produced excessive porosity. Efforts to fabricate a sandwich specimen produced unsatisfactory infusion. Finally, production of an all-composite tube appears possible, but of doubtful utility.

The infused composite band approach appears viable. The next steps should be to attempt this with the tube geometry, and to explore failure modes under loading.